UNIVERSIDAD TÉCNICA FEDERICO SANTA MARÍA
DEPARTAMENTO DE INGENIERÍA MECÁNICA
VAPARAÍSO - CHILE

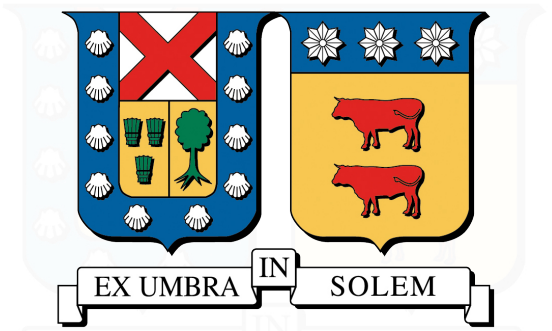

INFLATABLE AERODYNAMIC DECELERATOR FOR CUBESAT REENTRY AND RECOVERY: GEOMETRY EFFECTS UNDER RAREFIED CONDITIONS

NICOLÁS GABRIEL CAQUEO JARA

In partial fulfillment of the requirements for the degree of
MAGÍSTER EN CIENCIAS DE LA INGIERÍA MECÁNICA

and the degree of
INGENIERO CIVIL MECÁNICO

THESIS ADVISOR	:	DR. RODRIGO CASSINELI PALHARINI
INTERNAL EXAMINER	:	DR. HARVEY ZAMBRANO RODRIGREZ.
EXTERNAL EXAMINER	:	DR. CRAIG WHITE (University of Glasgow)

AUGUST 2023

Thesis:

INFLATABLE AERODYNAMIC DECELERATOR FOR CUBESAT REENTRY AND RECOVERY: GEOMETRY EFFECTS UNDER RAREFIED CONDITIONS

Author:

NICOLÁS GABRIEL CAQUEO JARA

This thesis is presented in partial fulfillment of the requirements for the degree of MAGÍSTER EN CIENCIAS DE LA INGIERÍA MECÁNICA and the degree of INGENIERO CIVIL MECÁNICO at Universidad Técnica Federico Santa María, Valparaíso, Chile.

Thesis advisor ,
Dr. Rodrigo Cassineli Palharini _____

Internal examiner ,
Dr. Harvey Zambrano Rodriguez _____

External examiner ,
Dr. Craig White _____

AUGUST 2023

ABSTRACT

In the last decade, a large number of nanosatellites have been placed into Earth's lower orbits, with the most common class of nanosatellite being the CubeSat. The long-lasting nature of these objects is causing a significant number of close encounters between active and decommissioned satellites. An efficient way to address this problem is the use of inflatable aerodynamic decelerators (IAD) for the deorbit and recovery of nanosatellites. Furthermore, the application of this technology to CubeSats reentry and recovery missions could enhance the capabilities of these small satellites in a sustainable and accessible manner.

Inflatable aerodynamic decelerators are devices designed to increase the area of the thermal protection system of a spacecraft regardless of the diameter constraints of the launch vehicle. These devices can be stored in a compact stowed configuration and expanded into a high-drag aeroshell for reentry and recovery applications. In this scenario, the primary objective of this investigation is to evaluate the impact of the IAD geometry on the flow, surface properties, and aerodynamic forces experienced by the spacecraft during reentry. In particular, numerical simulations are carried out on three distinct IAD configurations coupled with a 1U CubeSat during the upper stages of atmospheric reentry. The geometries considered in this study are assumed to be fully inflated, with a forebody radius of 0.3 m and three different cone angles of 68.8°, 45°, and fully rounded. Reentry of the IADs coupled with a 1U CubeSat payload was simulated considering nonreactive flow at 0° angle of attack and 105 km of altitude. Due to the high degree of flow rarefaction at this altitude, the Direct Simulation Monte Carlo method is used for all computations.

The influence of the IAD geometries on the velocity, temperature, density, and pressure profiles and contours was carefully investigated and discussed. From the results, the formation of a strong diffuse shock wave can be observed for all geometries considered in this investigation. However, a lower angle of the inflatable aeroshell is associated with a thinner shock wave and a maximum shock wave temperature closer to the shield's surface. These differences subside in the flow expansion over the IAD shoulder. In the rear of the inflatable shields, a low-temperature and low-velocity region is observed, indicating that the IAD geometries successfully mitigate the harsh conditions of reentry experienced by the payload. Moreover, it was found that aerodynamic elongated shapes exhibit larger wake regions when compared to blunt geometries, albeit at the expense of slightly higher gas temperature closer to the front surface of the shield. No recirculation zone was observed in any of the simulated IAD configurations considered in this investigation.

The effect of the forebody geometry on the surface aerothermal coefficients and aerodynamic forces is discussed thoroughly. According to these results, the thermal load experienced by the shields is particularly severe near the stagnation point, especially for aerodynamically shaped geometries. This kind of geometry exhibited the highest maximum heat transfer coefficient and total heat transfer of all configurations studied. However, it also showed a lower heat transfer coefficient on the middle segment of the shield's surface compared to the other geometries. In addition, the maximum pressure coefficient and the minimum shear stress coefficient were also identified at the nose tip, with the shear stress increasing toward the edge of the shoulder at a rate dependent on the geometry of the aeroshell. Geometries with aerodynamic profiles exhibited a low drag coefficient and a high ballistic coefficient, while more blunt geometries were found to have a better mass-to-drag ratio. The results show that thermal and mechanical loads decrease to negligible values in the rear section of the shield and on the CubeSat surface, further demonstrating the effectiveness of IAD devices in reducing mechanical loads on the payload.

All simulations were carried out using the dsmcFoam+ code, an open-source Direct Simulation Monte Carlo solver. A validation and verification process is performed to assess the physical accuracy and numerical resilience of the dsmcFoam+ code under conditions similar to those employed in the main body of work of this investigation. For the validation process of one of the test cases, additional continuum-based computational fluid dynamic computations were performed by researchers from the University of Naples Federico II at the lowest altitude of analysis. The results of this process demonstrate that the dsmcFoam+ solver is an adequate tool for the numerical investigation of CubeSat-based IADs in rarefied reentry conditions.

ACKNOWLEDGMENTS

Agradecimientos

Quisiera dedicar este apartado para expresar mis más sinceros agradecimientos a todas aquellas personas que me han apoyado y acompañado a lo largo de las distintas etapas de este proyecto de desarrollo personal, profesional y académico, que culmina en la confección de este trabajo de investigación de tesis.

Me gustaría agradecer a mi profesor guía, Dr. Rodrigo Cassineli Palharini, cuya orientación, apoyo y conocimientos han sido fundamentales para mi desarrollo académico y profesional. Gracias por brindarme la oportunidad de perseguir mi curiosidad científica y llevar a cabo este proyecto de investigación en conjunto.

A mi madre, Claudia, y a mi padre, William, les agradezco profundamente por su incondicional apoyo y cariño a lo largo de estos años de formación y crecimiento. Su amor, paciencia y comprensión han constituido la esencia que me ha permitido superar los distintos desafíos que he enfrentado en la vida. Me siento privilegiado de haberlos tenido como padres y honrado de poder ser motivo de sus alegrías. Siempre tendran mi amor incondicional en sus vidas, infinito candado.

A mi hermano Joaquín, le agradezco por ser el mejor compañero que pude haber tenido en esta travesía. Por inspirarme a mejorar como persona, estudiante y hermano. Te agradezco haber compartido conmigo tu naturaleza amable y gentil, de la que aún estoy aprendiendo. He tenido la fortuna de verte crecer y desarrollarte toda mi vida, nada me haría más feliz, que acompañarte otra más.

A Fernanda, por su infinito cariño y confianza a mi lado durante este proceso. En mis sueños, vuelvo a compartir mi vida contigo una y mil veces. Before meeting you I was sleeping in a long 19-year dark night, and now I see daylight. I only see daylight, daylight. And I can still see it all. All of you, all of me.

A mi familia en Iquique, Arica, Santiago y Valparaíso, quiero expresar mi gratitud por ser mi red de apoyo durante las distintas etapas de mi educación. Saber que sin importar donde estuviese podría contar con su ayuda, consejo y compañia me permitió avanzar con seguridad en mis aventuras.

A mis amigos y amigas, por brindarme momentos de distracción, risas y buenísimas historias que enriquecieron mi periodo universitario. Gracias por compartir conmigo una etapa tan significativa de nuestras vidas.

Finalmente, me gustaría expresar mis sinceros agradecimientos a la Universidad Técnica Federico Santa María por brindarme el espacio y las herramientas necesarias para desarrollar mi potencial académico. Su compromiso con la excelencia educativa me proporcionó los recursos y oportunidades que necesitaba para contribuir al progreso científico desde Chile.

En conjunto, cada una de las personas mencionadas en este apartado ha sido una pieza clave en la construcción de este proyecto de investigación, y espero vean reflejadas en este trabajo la influencia de cada una de sus contribuciones.

N.C.J.

Contents

List of Figures

List of Tables

List of Publications

Peer-reviewed scientific publications:

1. Caqueo N., Rioseco D., Palharini R.C., Palharini R.S.A., Gaglio E. and Savinno R., Inflatable Aerodynamic Decelerator for CubeSat Reentry and Recovery: IAD Geometrical Effects on the Flowfield Structure. Aerospace Sciene & Technology, 108571 (2023).
2. Caqueo N., Palharini R.C., Palharini R.S.A., Gaglio E. and Savinno R., Inflatable Aerodynamic Decelerators for CubeSat Reentry and Recovery: Surface Properties. (Under review) Nature Scientific Reports (2023).
3. Rioseco D., Caqueo N., Palharini R.C., Palharini R.S.A., Gaglio E. and Savinno R., Inflatable aerodynamic decelerator for CubeSat reentry and recovery: Altitude effects on the flowfield structure. Aerospace Sciene & Technology, 108358 (2023).

Conferences and congresses:

1. Gaglio E., Cecere A., Guida R., Mungiguerra S., Savino R., Caqueo N. and Palharini R.C., Aerodynamic analysis of a flap-based deployable re-entry system in different flight conditions. In: 25th AIAA International Space Planes and Hypersonic Systems and Technologies Conference, India (2023).
2. Caqueo N. and Palharini R.C, Desaceleradores Aerodinámicos Inflables para la Reentrada y Recuperación de CubeSats: Efectos Geométricos en las Propiedades de la Superficie". In: XII Congreso Argentino de Tecnología Espacial, Mendoza, Argentina (2023).
3. Caqueo N. and Palharini R.C, Análisis aerotermodinámico de vehículos espaciales durante la reentrada atmosférica. In: XX Jornadas de Mecánica Computacional, Valdivia, Chile (2022).
4. Palharini R.C, Rioseco D., and Caqueo N., DSMC Computations of Inflatable Aerodynamic Decelerators for CubeSats. In: 9th European Conference for Aeronautics and Space Sciences (EUCASS), Lille, France (2022).

Nomenclature

Physics constants

$\hat{N}$	Avogadro's constant, 6.022×10^{23} mol^{-1}
k_b	Boltzmann constant, m^{2}kgs^{-2}K^{-1}
R	Universal gas constant, 8.314 JK^{-1}mol^{-1}

Symbols

Δt	Time step, s
Δt_{res}	Residence time, s
δ	Molecular spacing, m
ϵ	Impact deflection angle, °
Λ	Fraction of inelastic collisions
λ	Mean free path, m
Ma	Mach number, U/c_s
ν	Mean collision rate, s^{-1}
ω	Viscosity exponent
$\overline{s_{\text{cell}}}$	Average cell edge, m
ρ	Density, kgm^{-3}
σ_{T}	Total collision cross-section, m^2
τ_c	Mean collision time, s
τ_{rel}	Relaxation time, s
Θ	Characteristic temperature
ε	Average energy per particle
φ	Average probability of inelastic collisions
ζ	Number of internal degrees of freedom
A	Area, m^2
b	Distance of closest approach, m
c	Particle velocity, ms^{-1}
c'	Particle thermal speed, ms^{-1}
c_{r}	Relative velocity between two particles, ms^{-1}

C_D	Drag coefficient, $F_d/(\frac{1}{2}\rho V^2 A_{ref})$
C_f	Skin friction coefficient, $\tau/\frac{1}{2}\rho_\infty U_\infty^2$
C_h	Heat transfer coefficient, $q/\frac{1}{2}\rho_\infty U_\infty^3$
c_m	Velocity of the center of mass, ms^{-1}
C_p	Pressure coefficient, $p - p_\infty/\frac{1}{2}\rho_\infty U_\infty^2$
c_p	Speed of DSMC particles, ms^{-1}
C_m	Momemtum coefficient, $M/\frac{1}{2}\rho_\infty U_\infty^2 AL$
c_s	Speed of sound, ms^{-1}
d	diameter, m
E	Total energy of a system, J
e	Specific energy, Jkg^{-1}
F	Force, N
f	Distribution function
f_0	Maxwellian distribution
F_A	Axial force, N
F_D	Drag force, N
F_N	Ratio of real molecules to simulated molecules
H	Altitude, km
L	Length, m
m	Mass, kg
m_r	Reduced mass, kg
N	Number of particles
n	number density, m^{-3}
N_c	Number of collisions
n_p	Number of simulated particles
N_coll	Number of collisions
N_{equiv}	Number of equivalent particles, dimensionless
p	Pressure, Pa
P_coll	Probability of collision
Q	Total heat flux, W
q	Heat flux per unit area, Wm^{-2}
r	Particle position, m
R_f	Random number between 0 and 1
R_n	Nominal raidus, m
T	Temperature, K
t	Time, s

T_{ov} Overall temperature, K

U Flow speed, ms^{-1}

V Volume, m^3

Z Relaxation collision number

% Diff Percentage difference, $(x_1 - x_2)/(\frac{1}{2}(x_1 + x_2)) \times 100$

AoA Angle of attack, °

BC Ballistic Coefficient, kg/m^2

Kn Knudsen number, λ/L

Superscripts

* Post-collision quantity

VHS Variable Hard Sphere

Subscripts

$\perp$ Perpendicular component

∞ Freestream property

ref Reference value

$\parallel$ Parallel component

coll Collision

wall Wall property

int Internal property

rot rotational mode

tr Translational mode

vib Vibrational mode

Acronyms

ADEPT Adaptive Deployable Entry and Placement Technology

AIAA American Institute of Aeronautics and Astronautics

AMROC American Rocket Company

ASI Italian Space Agency

CDRS CubeSat De-orbit and Recovery System

CELS CubeSat End-of-Life System

CFD Computational Fluid Dynamics

CIRA Italian Aerospace Research Centre

COTS Commercial Off-the-shelf

DESCENT DEployable, Self-regulating, CENTrifugally-stiffened decelerator

DEV Deployable Entry Vehicle

DRS Deorbit and Recovery System

EDL Entry, Descent and Landing

EGG reentry satellite with gossamer aeroshell and GPS/Iridium

ESA European Space Agency

FCC Federal Communications Commission

HEART High-Energy Atmospheric Reentry Test

HIAD Hypersonic Inflatable Aerodynamic Decelerator

HS Hard Sphere

IAD Inflatable Aerodynamic Decelerators

IRDT Inflatable Re-entry and Descent Technology

IRENE Italian Re-Entry NacellE

IRVE Inflatable Re-entry Vehicle Experiment

ISS International Space Station

JAXA Japan Aerospace Exploration Agency

Langley Aerothermodynamic Upwind Relaxation Algorithm LAURA

LEO Low Earth Orbit

MAAC Membrane Aeroshell for Atmospheric-entry Capsule

MCF Majorant Collision Frequency

MISTRAL Air-launcheable Micro-Satellite with Reentry Capability

NASA National Aeronautics and Space Administration

NC Null Collision

NTC No-Time-Counter

PWT Plasma Wind Tunnel

QK Quantum Kinetic

SBF Simplified Bernoulli Trials

SMART Sensible, Modular, Autonomous Return Technology

SPES Small Planetary Entry Simulator

SPLASH Self-DePloyable FLexible AeroSHell for de-Orbiting and Space Re-entry

TC Time Counter

TCE Total Collision Energy

TPS Thermal Protection System

ULA United Launch Alliance

V&V Validation and Verification

VHS Variable Hard Sphere

VLEO Very Low Earth Orbit

1 | Introduction

In the last decade, the interest of the space sector in the small satellite industry has grown substantially [1, 2]. In 2018, more than USD $2.5 Billion were invested into start-up space ventures, with a significant proportion of this funding dedicated to the development of small satellite technology [1]. Even more, as of 2022, the nanosatellite industry alone has an estimated market size value of USD $2.8 billion and is projected to reach over USD $6.7 billion by 2027 [3]. A particular nanosatellite class, the CubeSat, has played a critical role in the small satellite revolution [4, 5]. CubeSats are small satellites built in increments of a standardized 1U unit factor, each unit being a 10 x 10 x 10 cm cube with a maximum mass of 2 kg [6]. Some commonly used CubeSat form factors are shown in Figure 1.1.

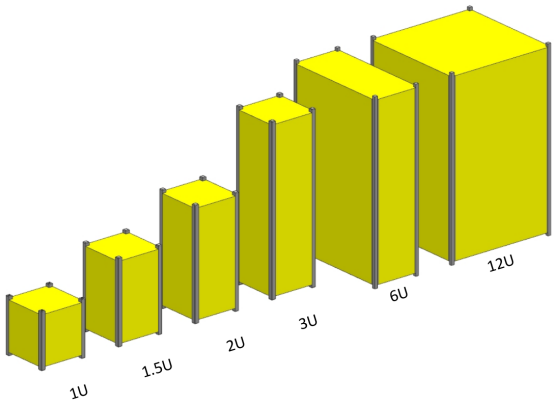

Figure 1.1: Common CubeSat size factors [6].

CubeSats were originally designed for educational purposes, but are now used in a wide range of applications by government agencies, private companies, and academic institutions [7, 8]. Furthermore, CubeSat missions in 2018 were primarily used for remote sensing and technology development; with significant growth rate in CubeSat applications to science and communications missions since 2016 [7]. A driving factor in the shift of the industry towards small form factors is that CubeSats are able to take advantage of the use of Commercial Off-the-shelf (COTS) components to achieve advanced missions at a fraction of the cost [9, 1]. Rapid advances in technology miniaturization and standardization help these small satellites to benefit from a more agile philosophy of operation, enabling these spacecrafts to have a short development

time, be easy to replace, have lower costs and benefit from more up-to-date components [7]. These reasons have led to an explosion in growth in the total number of nanosatellite and CubeSats launches, as can be observed in Figure 1.2, with more than 2100 CubeSats satellite units launched as of May 2023 [10].

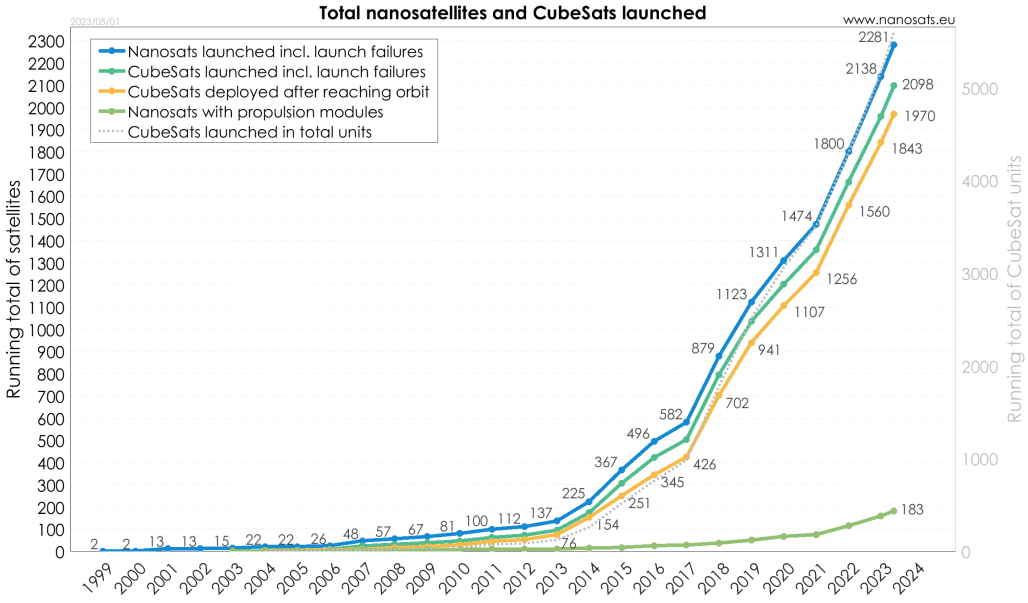

Figure 1.2: Total number of nanosatellites and CubeSats launched as of 2023 [10].

However, the unprecedented low entry barriers and the increasing launch rate of these small satellites have raised concerns about the sustainability of space operations [11, 12, 13]. Many nanosatellite projects are expected to be deployed in the coming years, including multiple CubeSat constellations with thousands of individual units [14, 15, 16]. This poses a greater risk of in-orbit collisions, which, in turn, could cause a significant increase in the amount of space debris in orbit [11]. Moreover, the environmental consequences of the significant increase in mass injected into the atmosphere by reentering artificial objects, estimated to raise 27 times the natural level of aluminum in the atmosphere by 2040, remain largely unquantified [11]. The sudden and rapid increase in the launch rate of small satellites is particularly alarming in Earth's lower orbits, such as Low Earth Orbit (LEO) and Very Low Earth Orbit (VLEO). Lower orbits have lower launch costs and provide several benefits to small satellite missions [17]; which, in turn, have contributed negatively to the partial saturation of the capacity of these orbits to sustain long-term space activities [12, 16]. Furthermore, as shown in Figure 1.3, CubeSats have been found to have a higher failure rate than larger satellites, with CubeSat missions having an overall 61% success rate from 2005 until 2018 [7]. In addition to this, faulty or non-operational CubeSats can remain in orbit for up to 25 years after their operation cycle [18, 19, 20], as the majority of launched nanosatellites lack a dedicated propulsion system for deorbit, as can be observed in Figure 1.2.

In this way, current nanosatellite activities increase the potential threat of a cascade of collisions

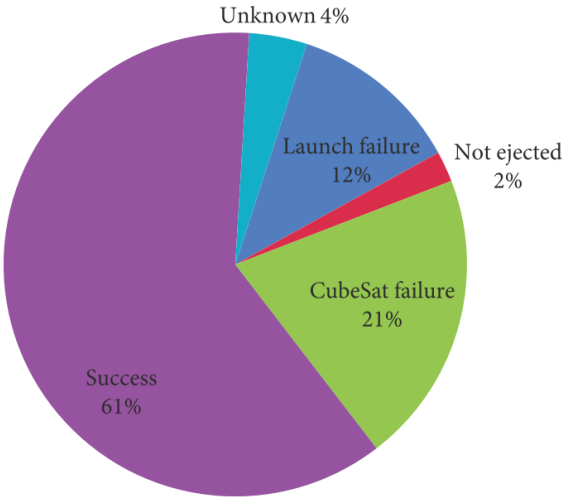

Figure 1.3: CubeSat mission status including CubeSats launched from 2005 until 2018 [7].

creating an orbital debris environment dominated by random collisions and a runaway increase in the amount of orbiting pieces of debris [2]. This phenomenon is referred to as the Kessler syndrome, and it may prevent access to the most important Earth's orbits in the future [21, 22, 23]. In response to these concerns, in September 2022, the Federal Communications Commission (FCC) lowered the orbit-life limit from 25 to 5 years after satellite operation for spacecrafts orbiting at 2000 km or below [24], recognizing the rapid changes underway in the framework of space affairs [12]. To address these challenges and ensure the sustainable and efficient use of space, further developments in nanosatellite deorbit, reentry, and recovery technology are needed. Inflatable Aerodynamic Decelerator (IAD) technology is a promising solution to address the challenges of CubeSat reentry and recovery, while expanding CubeSat capabilities in a cost-effective and sustainable way [25, 26].

1.1 Inflatable Aerodynamic Decelerators

IADs are inflatable devices designed to be stored in a compact stowed configuration when not in use and expanded into a high-drag Thermal Protection System (TPS) when needed [26], protecting the payload and slowing down the spacecraft as it enters the planet's atmosphere. IADs can be customized to specific missions and payloads, as they allow the Ballistic Coefficient (BC) to be an independent design parameter from the diameter constraints of the launch vehicle [27, 28]. The BC is a parameter that relates the mass and the drag of the reentry body such that

$$\mathrm{BC} = \frac{m}{C_D\, A_{\mathrm{ref}}}, \tag{1.1}$$

where m is the mass, A_{ref} is the vehicle's reference surface, and C_D is the drag coefficient. When

expanded, the increased aeroshell area of the IAD reduces the associated ballistic coefficient of the spacecraft, which in turn allows for greater deceleration and decreased thermal and mechanical loads during reentry [26]. Compared to traditional rigid aeroshells, inflatable and deployable aerodynamic decelerator technology enhances the capabilities of reentry missions by allowing safe delivery of greater payload mass [29] and higher elevation descent in thinner atmospheres [30]. Furthermore, the use of IAD technology has the potential to also greatly benefit the reentry and recovery missions of small satellites or secondary payloads [25, 31, 32, 33], making new scientific and commercial missions feasible [32] and further reducing costs through complete or partial reuse of small satellites. Moreover, when expanded in low-altitude orbits, the increased area of the aeroshell can induce the deorbit process based solely on the drag produced by the IAD in contact with the atmosphere, eliminating the need for a dedicated deorbit propulsion subsystem while helping to keep the lifespan limit of spacecrafts in lower orbits [25, 34].

IAD technology was first explored in the 1960s, peaking in the mid-seventies during the mission planning phases for the Viking, Pioneer, and Galileo programs; for the atmospheres of Mars, Venus and Jupiter, respectively. As shown in Figure 1.4, different types of IAD technology were evaluated through wind tunnel and flight tests during this time. However, no significant progress occurred after this period until the 1990s [35], where the increasingly ambitious space exploration missions exposed the limitations of trailing parachutes and rigid aeroshells, renewing interest in IAD technology for Entry, Descent and Landing (EDL) [36]. Thus, since the 1990s, many Deployable Entry Vehicle (DEV) concepts, including inflatable and mechanically deployable aerodynamic decelerators, have been proposed and developed.

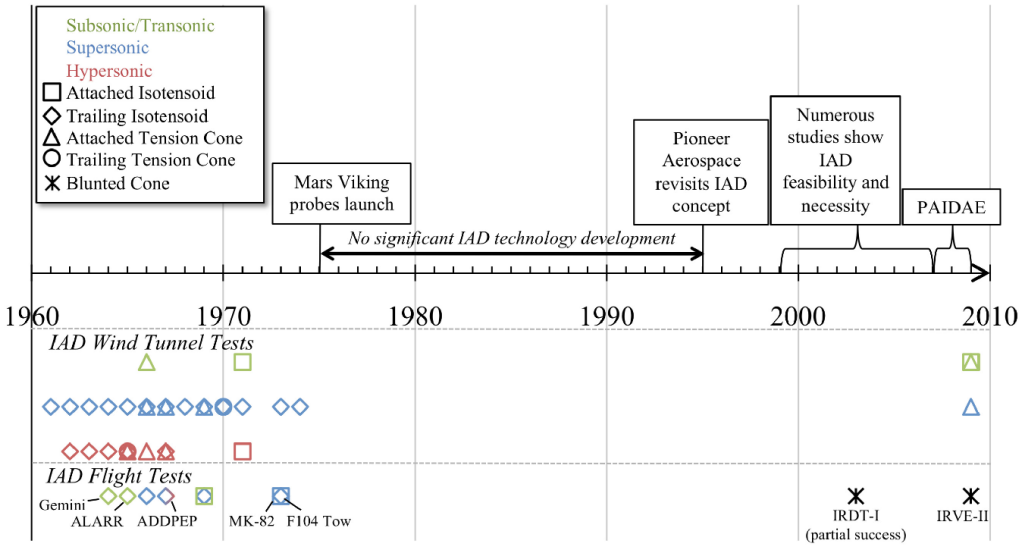

Figure 1.4: History of IAD technology development from 1960 to 2010 [35].

The history of modern DEV technology can be traced back to the inception of the ParaShield concept, developed by Akin D. in the early 1990s [37, 38]. This concept acted as both the heat shield and the landing

parachute; hence the name ParaShield. Initial development of the ParaShield concept was performed by students of Akin D. in 1988. In 1989, a suborbital demonstration vehicle based on the ParaShield concept, called Skidbladnir, was scheduled to be launched by the American Rocket Company (AMROC) SET-1 launch vehicle. The Skidbladnir design concept featured a conical pressure vessel that housed all vehicle systems, with the ParaShield system folded around it. The stowed and deployed configurations of Skidbladnir are shown in Figure 1.5a and Figure 1.5b, respectively. Unfortunately, a launch vehicle problem resulted in the failure of the suborbital flight test and the ParaShield concept was never tested in flight. Nevertheless, subsonic and supersonic wind tunnel tests, as well as hypersonic Computational Fluid Dynamics (CFD) simulations, were carried out on the ParaShield concept. These tests validated the aerodynamic modeling of the ParaShield in both subsonic and supersonic regimes, whereas hypersonic simulations showed that the system could survive entry from LEO [38].

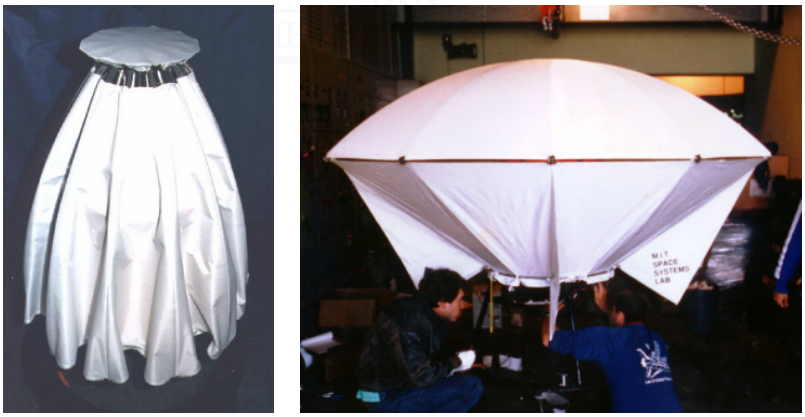

(a) Stowed configuration. **(b)** Deployed configuration.

Figure 1.5: Skidbladnir ParaShield [38].

Later, in 1996, the University of Bremen carried out some preliminary design studies of the BREM-SAT 2 mission, which aimed to return a small satellite back to Earth through the use of a deployable heat shield [39]. During launch, the aerodynamic decelerator device could be stored in a 0.65 m diameter stowed configuration, as shown in Figure 1.6a. When expanded, the deployable aeroshell used for BREM-SAT 2 resembles an umbrella-like structure, as can be observed in Figure 1.6b, and increases the satellite front area by a factor of 12, to a diameter of 2.24 m, which yield to a heat flux maximum of 200 kW/m^2 for this configuration. The design also considered the use of COTS materials for the heat-resistant silicon fabric of the umbrella and the twelve titanium arms. Although a tentative launch for 1999 was considered [39], the deployable aerodynamic decelerator design BREM-SAT 2 has never been tested to date.

The first partially successful test of a modern IAD DEV was the orbital flight test of Inflatable Re-entry and Descent Technology (IRDT) in February 2000 [40, 41]. The IRDT concept, shown in Figure 1.7a, was developed by Russia and the European Space Agency (ESA) for Mars and LEO reentry missions [42]. The main reentry configuration of the IRDT vehicle consisted of a pressurized core covered by different

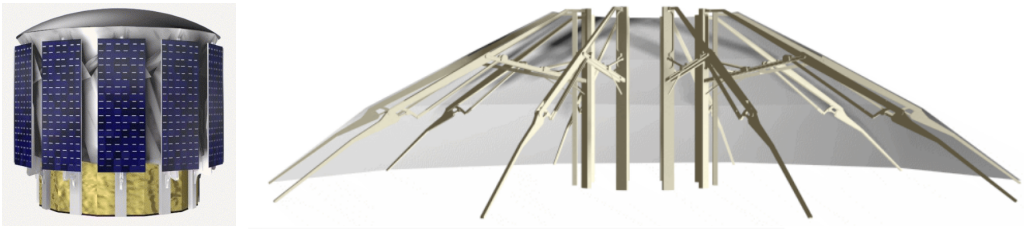

(a) Stowed configuration. **(b)** Deployed configuration.

Figure 1.6: BREM-SAT 2 [39].

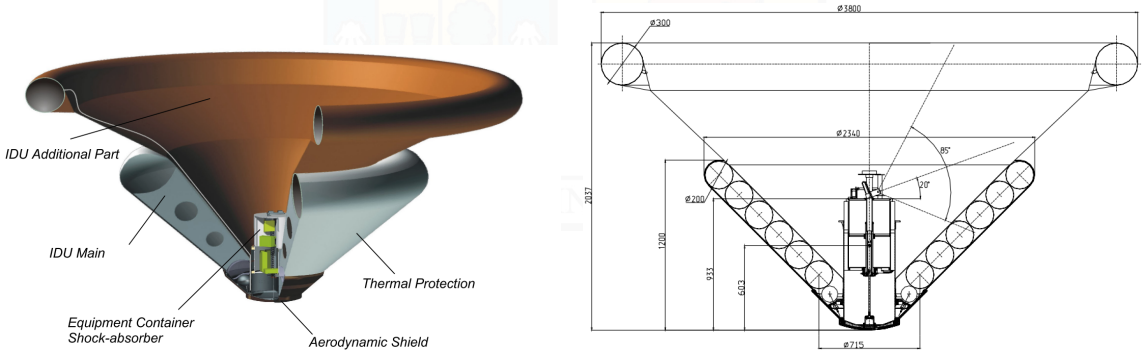

(a) Vehicle design [40]. **(b)** Fully deployed geometry description [42].

Figure 1.7: IRDT vehicle description and dimensions in fully deployed configuration.

layers of thermal insulation and flexible ablative material that was deployed prior to reentry. A secondary deceleration cascade was deployed to serve as a landing system after reaching subsonic speed [43]. As shown in Figure 1.7b, the aerodynamic shape of the IRDT vehicle during reentry was that of a blunted cone, with a nose radius of 0.61 m, a cross section diameter of 2.34 m, and a 45° half-cone angle [42]. Despite some minor deficiencies, the first mission confirmed the basic feasibility of the IRDT technology, and a second demonstration mission, IRDT-2, was planned for 2001 [40]. However, two launch attempts in 2001 and 2002 resulted in failures due to launch vehicle problems and issues with launcher interface, respectively. In 2005, another flight test of the IRDT vehicle, the IRDT-2R project, was carried out. The test provided useful flight data, but the demonstrator could not be recovered as it experienced a failure near peak deceleration that caused a significant deviation from its nominal trajectory and landing target [42].

Similarly, during the latter half of the 2000s, advances by the National Aeronautics and Space Administration (NASA) on the Hypersonic Inflatable Aerodynamic Decelerator (HIAD) program led to several flight tests of the Inflatable Reentry Vehicle Experiment (IRVE) [44, 45]. A first orbital flight test attempt, launched in 2007 on a Terrier Orion sounding rocket, was unsuccessful because the IRVE launcher failed to release the reentry vehicle from the launch shroud [46]. Despite this setback, in 2009, the IRVE-II orbital flight test successfully separated from the launcher, inflated as planned, and demonstrated stable flight through reentry and descent while providing valuable flight performance data to the ground. As shown in Figure 1.8a, the IRVE-II reentry vehicle consisted of a conical inflatable aeroshell attached at the leading edge

of a rigid cylindrical centerbody. In launch configuration, the vehicle had an outer diameter of 0.419 m with the deflated aeroshell packed around the centerbody. After separation from the launch vehicle, the aeroshell was inflated to its reentry configuration of a 60 degree half-angle sphere cone, with an outer diameter of 3 m [46, 45]. The first flight test of the IRVE-II concept is a milestone in the development history of IAD technology, as it successfully demonstrated inflation and reentry survivability, assessed the thermal and drag performance of the reentry vehicle, and collected flight data for comparison with analysis and design techniques used in vehicle development [47, 29].

Following the success of the IRVE-II mission, IRVE-3 launched in 2012 and successfully achieved its two main objectives; to further demonstrate the reentry survivability of the HIAD concept, reaching Mach 10 during atmospheric reentry; and to demonstrate the effectiveness of generating lift with a HIAD from a radial center of gravity offset [48, 49]. The IRVE-3 design shared the same general configuration as the earlier IRVE-II mission, that is, a 3 m outer diameter and a 60° half-angle sphere cone. However, the inflatable structure was redesigned to handle increased thermal and mechanical loads, keeping the stacked-toroid approach but adding individual structural straps connecting the toroids to each other and to the centerbody [49, 50], as shown in Figure 1.8b. Furthermore, the thermal protection system was upgraded from the layered Nextel fabric used on IRVE-II to a multilayer system more capable of handling the heating levels experienced during flight [51, 49].

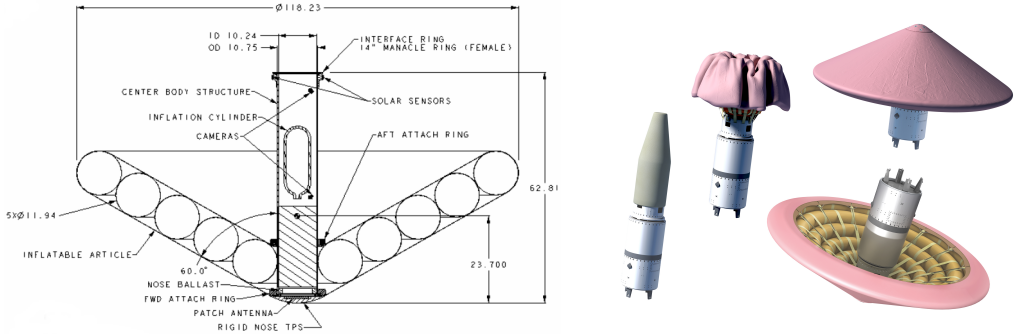

(a) IRVE-II geometry description [44]. **(b)** IRVE-3 deployment stages [52].

Figure 1.8: IRVE-II geometry description and IRVE-3 deployment stages.

Beyond IRVE-3, NASA proposed four additional HIAD missions. The High-Energy Atmospheric Reentry Test (HEART) was planned for late 2016 and aimed to demonstrate the effects of scale on development and performance in an environment relevant for robotic Earth and planetary entry [53, 54, 55]. The HEART HIAD design, shown in Figure 1.9a, could be stored within a 2.5 m diameter launch vehicle and deployed into a 55 degree 8.3 m diameter aeroshell prior to atmospheric entry. A second mission of similar nature, HEART-2, was considered to test the ability to control larger HIAD vehicles and land at a targeted location [53]. In order to successfully complete this potential mission and bridge the gap between HEART and HEART-2, the IRVE-4 mission was proposed to investigate the HIAD control response and targeting on an inexpensive subscale vehicle [47, 53]. Lastly, the United Launch Alliance (ULA) in collaboration with NASA

proposed that a HIAD be utilized as part of the Sensible, Modular, Autonomous Return Technology (SMART) initiative to enable recovery of the Vulcan launch vehicle booster main engines [56]. A first experiment, referred to as HIAD on ULA (HULA), proposed a scale increase from the 3 m diameter of IRVE to a 6 m diameter aeroshell. Figure 1.9b shows a scale comparison between the proposed HULA design concept and the IRVE-III reentry vehicle. The goal of the HULA flight test was to use a half scale vehicle to provide flight data relevant to the ULA SMART initiative and the Mars EDL Pathfinder mission [56]. To date, none of these missions (HEART, HEART-2, IRVE-4, and HULA) have been launched.

(a) HEART [54]. **(b)** HULA [56].

Figure 1.9: HEART and HULA reentry vehicle concepts.

However, as recently as November 2022, the Low-Earth Orbit Flight Test of an Inflatable Decelerator (LOFTID) successfully entered the Earth's atmosphere using NASA's second-generation HIAD technology [57, 58]. The LOFTID reentry vehicle shared the same design objectives as the proposed HULA experiment; that is, a large mass of 1700 kg and 6 m diameter deployed inflatable aeroshell. Instead of the 60 degree half-angle sphere cone used in previous IRVE experiments, the LOFTID reentry vehicle is characterized by a 70° forebody geometry [26], as shown in Figure 1.10. The LOFTID orbital flight technology demonstration mission is the largest blunt body aeroshell ever flown, demonstrating the viability of large-scale HIAD technology in an Earth orbital entry environment [26]. The LOFTID experiment also relates to applications in Mars, Venus, and Titan missions; as well as the safe return of Vulcan rocket engines as part of ULA's re-use program [58].

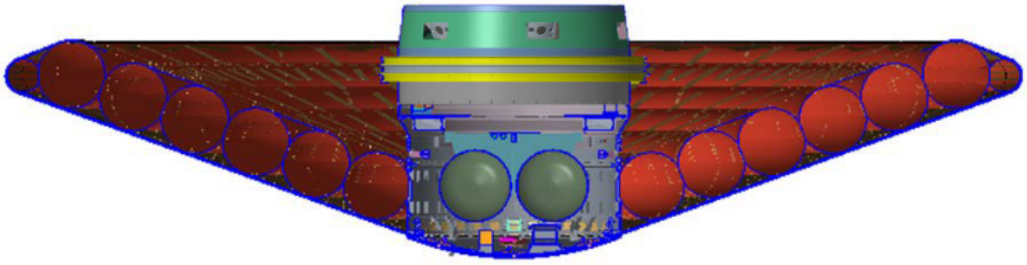

Figure 1.10: LOFTID profile section view [57].

In addition to the HIAD program, NASA started the development and testing of a mechanically deployed system called Adaptable Deployable Entry and Placement Technology (ADEPT). The ADEPT

project has a wide range of applications, including science missions to Venus, Mars, and the Outer Planets [59, 60, 61, 62]. As shown in Figure 1.11a, the mechanically deployable concept is akin to an umbrella, employing a 70° sphere-cone thermal protection system made of flexible 3D-woven carbon fabric material over high-strength ribs that make up the aeroshell structure [63, 64]. A particular characteristic of the initial ADEPT design is the conceptual capability to invert the aerosurface like an umbrella to form a landing system, as shown in Figure 1.11b, hence the name ADEPT. This landing configuration uses the structural spokes of the umbrella to provide attenuation of landing impact, helping to provide soft and safe landing on uneven terrain [63]. Although ADEPT is an ongoing project, it is worth noting that no further studies have been carried out on the viability of the ADEPT landing configuration, with recent publications on the project making no mention of this feature [26, 65, 66]. Nevertheless, ground testing campaigns have demonstrated the ability of the carbon fabric material to withstand combined mechanical and aerothermal loads [67], and system-level aerothermal tests have shown the concept to be a good candidate for multiple mission destinations; including Venus, Mars, Titan, Uranus, Neptune, and Earth return [26, 68].

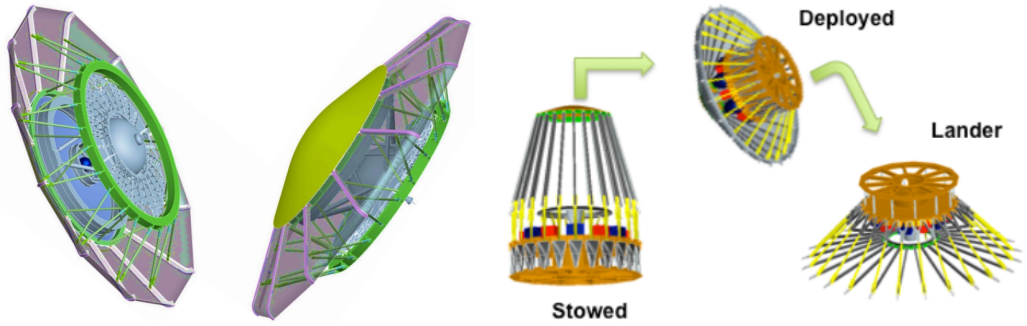

(a) Deployed configuration [62]. **(b)** ADEPT configurations [63].

Figure 1.11: ADEPT concept design.

In 2012, a demonstration flight of the Membrane Aeroshell for Atmospheric-entry Capsule (MAAC) developed by the Japan Aerospace Exploration Agency (JAXA) was launched using the Japanese S-310 sounding rocket. Figure 1.12a shows a schematic of the experimental reentry vehicle demonstrator, which consists of a capsule-type main body, a thin membrane flare, and an inflatable torus [69]. The Sounding Rocket Experiment of MAAC (SMAAC) successfully completed its mission and demonstrated the performance of the flare-type thin membrane aeroshell sustained by the inflatable torus as a decelerator under atmospheric entry conditions [69, 70]. As can be observed in Figure 1.12b, the capsule had an initial diameter of 0.19 m, whereas the inflated aeroshell had an overall projected diameter of 1.2 m and a flare angle of 70 degrees, connected to the inflatable torus at its edge [71]. Figure 1.12b also shows the positions of the embedded thermocouples placed on the back of the SMAAC aeroshell. The aerodynamic heating behavior of the vehicle was investigated using the measured temperature history, and the data was found to be in reasonable agreement with predictive numerical simulations [71]. Since then, additional ground tests and numerical simulations on the MAAC concept have been carried out [72, 73, 74].

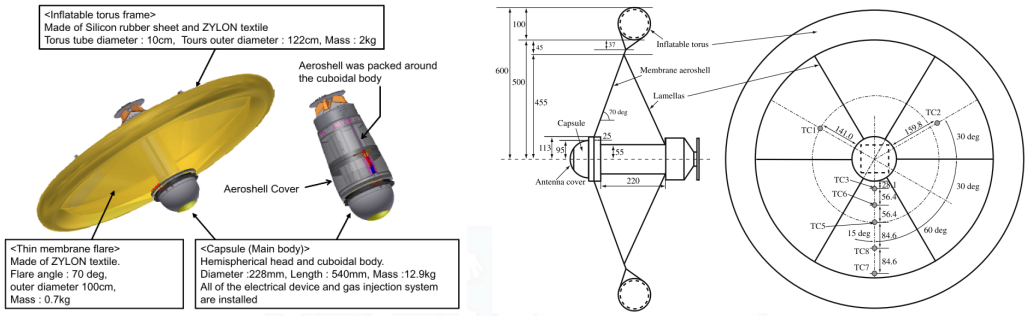

(a) Schematic of the experimental vehicle [69]. **(b)** SMAAC geometry description. [71].

Figure 1.12: Sounding Rocket Experiment of MAAC (SMAAC) vehicle design.

In 2011, the Italian Space Agency (ASI) started a feasibility study on the Italian Re-Entry NacellE (IRENE) project, a low-cost deployable reentry system to enable future space missions requiring planet atmosphere entry or Earth reentry [75, 76]. When deployed, the preliminary dimensions of the IRENE reentry capsule include a 45 degree half-vertex angle and a maximum diameter of 0.3 m for the deployed heat shield [75]. Proposed applications of the IRENE vehicle include: payload return to Earth from the International Space Station (ISS), recoverable scientific experiments in LEO, robotic exploration missions, and/or future manned space systems [76]. The flexible TPS material and complementary ceramic foam for the nose have undergone preliminary testing in the Small Planetary Entry Simulator (SPES) hypersonic wind tunnel at the University of Naples Federico II. Furthermore, a subsystem test including both the nose and flexible TPS material was carried out at the Italian Aerospace Research Centre (CIRA) in the SCIROCCO Plasma Wind Tunnel (PWT) [77]. Figure 1.13 shows some relevant images of the IRENE subsystem tests. The test was considered successful and demonstrated that the materials selection and design choices were suitable, feasible, and exploitable [75]. Consecutive studies have focused on the development of a scaled down prototype half the size of IRENE, named MINI-IRENE [78, 79, 80]. The current phase of the program, led by CIRA and ESA, aims to perform suborbital flight tests of the MINI-IRENE concept on the MAXUS sounding rocket and the VSB-30 rocket [81, 77].

Figure 1.13: IRENE subsystem test in the SCIROCCO plasma wind tunnel at CIRA [75].

The IRENE mechanical deployable heat shield is also being considered for two other Italian projects, the Air-launcheable Micro-Satellite with Reentry Capability (MISTRAL) and the IPERDRONE project [82]. The primary objective of the MISTRAL project is to develop a 20-30 kg class spacecraft provided with a

deployable flexible aerobrake that can return it to Earth in a recovery area [83]. The spacecraft is equipped with a payload compartment capable of accommodating a variety of instruments to allow the project to satisfy a large number of missions ranging from Radiation measurement to Exobiology to Atmospheric mapping to Earth observation [83]. Once the mission is completed, the aerobraking system can perform an aerodynamic deorbit maneuver, a controlled reentry into the atmosphere, and a soft landing (or splash down) to allow users to retrieve and post-process the data recorded on board [34]. The MISTRAL mechanical heat shield concept, shown in Figure 1.14, can modulate the deployable surface for aerodynamic control of the deorbiting trajectory to guide the capsule towards the selected landing and recovery point [84, 85, 82].

On the other hand, the objective of the IPERDRONE program is to design and develop a small spacecraft reentry system capable of performing in-orbit operations on the International Space Station (ISS) and/or other Space Systems, reenter the atmosphere, and safely land on Earth bringing back unaltered scientific payloads/experiments [86]. The IPERDRONE program will consist of a series of missions characterized by incremental objectives, aiming at qualifying new type of missions and related technologies [87]. There are two missions in preparation as part of the first stage of the program. The first mission, named IPERDRONE.0, aims to validate the system performance and subsystems; concluding in a deorbiting maneuver demonstration, which will lower its orbit into a pre-defined re-entry corridor to guarantee the complete disintegration of the spacecraft during the re-entry phase. The second mission, named IPERDRONE.1, will aim to demonstrate the ability to return payload back to Earth without the use of active propulsion, instead employing the mechanically deployed shield IRENE [87, 82].

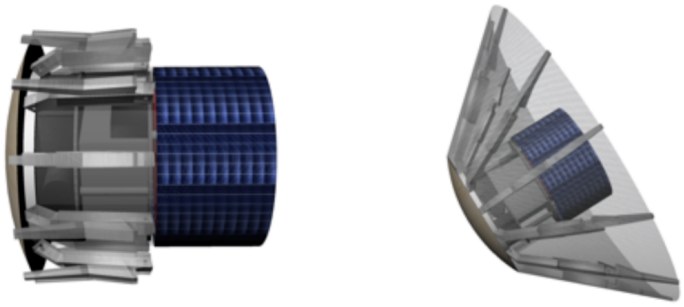

Figure 1.14: MISTRAL design concept in stowed in deployed configuration [83].

Currently, the European Union H2020 program is funding the development of the EFESTO project to increase the European technology readiness level of inflatable heat shields for reentry vehicles [88, 89]. The EFESTO project is focused on the development of IAD technology for two key applications, Reusable Small Launchers Upper Stages and Mars Robotic Exploration [88]. For the Earth application, the recovery of the AVUM VEGA upper stage has been chosen as the baseline case study. The current mission layout consists of a deorbit from the Polar Orbit followed by a controlled entry phase. Atmospheric deceleration is achieved using a 60° angle 4.5m diameter class HIAD, followed by a parachute descent phase [90]. For the Mars Application, the robotic exploration mission class resulted in a 10 m diameter IAD class, with approximately

6600 kg of entry mass, a BC of approximately 50 kg/m^2, and a sphere-cone heat shield with a 70 degree angle [89, 88]. To overcome some identified weaknesses of the stacked toroid configuration of the IRVE series, the Annular Tori configuration has been adopted for both the Earth and Mars scenarios, with slightly different configuration optimized for each scenario [88]. Figure 1.15 shows the component description of the deployed configuration of both conceptual reentry vehicles, for Earth and Mars applications, respectively.

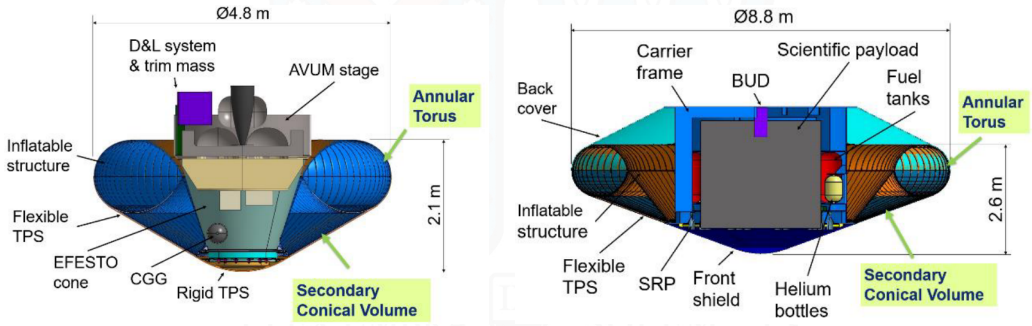

(a) AVUM **(b)** MARS

Figure 1.15: EFESTO reentry vehicles for Earth (AVUM) and Mars applications (MARS) [90].

1.2 Reentry flow regimes

As described in section 1.1, the benefits of IAD technology make it a good candidate for a wide range of space applications, from small spacecraft low-orbit reentry missions to the delivery of large mass payloads in planetary exploration missions. In all of these scenarios, IAD reentry vehicles are bound to experience rarefied flow phenomena, particularly during the first stages of atmospheric reentry. The low atmospheric density at high altitudes characterizes the physical interaction between the spacecraft and the surrounding flow; where the latter usually exhibits a significant deviation from the thermodynamic equilibrium. The extent of these effects are described to as the degree of rarefaction of the flow, which further differentiates the flow regimes experienced by a spacecraft during the reentry process and fundamentally shifts the approach to model and investigate flows under these conditions.

Since the atmospheric density and the mean free path of freestream particles vary with altitude, the reentry vehicle experiences different degrees of flow rarefaction during descent. The mean free path (λ) is the average distance traveled by molecules between collisions and at high altitudes, where there is low atmospheric density, molecules exhibit a large mean free path. High altitudes are associated with a significant degree of flow rarefaction, as the lack of molecular collisions leads to a significant degree of non-equilibrium in the flow. Thus, in a rarefied flowfield, the equilibrium assumption underlying all continuum models is invalid. This means that traditional Computational Fluid Dynamic (CFD) methods based on the Navier-Stokes equations become inadequate after a certain threshold of flow rarefaction, as these models no longer form a determinate set of equations under these conditions [91, 92].

As mentioned above, during the initial stages of the reentry process, the spacecraft first encounters a flow regime with a very large mean free path. This flow regime is denominated as free molecular flow, where the effects of intermolecular collisions are negligible. At lower altitudes, the spacecraft goes through a flow regime denominated as transitional regime, where the effect of intermolecular collisions can no longer be ignored [93, 94]; yet, it is not sufficient to allow for the use continuum models. Eventually, the spacecraft reaches a medium of sufficiently high atmospheric density and a short mean free path, which allows for the validity of the equilibrium assumption. These flow regimes can be identified through the Knudsen number (Kn), defined as

$$\mathrm{Kn} = \frac{\lambda}{L}, \tag{1.2}$$

where L is the characteristic length of the reentry vehicle or spacecraft. Thus, for the same set of reentry conditions, the degree of flow rarefaction can vary for vehicles of different sizes. Figure 1.16 shows the relation between the degree of flow rarefaction and its respective flow regime as a function of the Knudsen number.

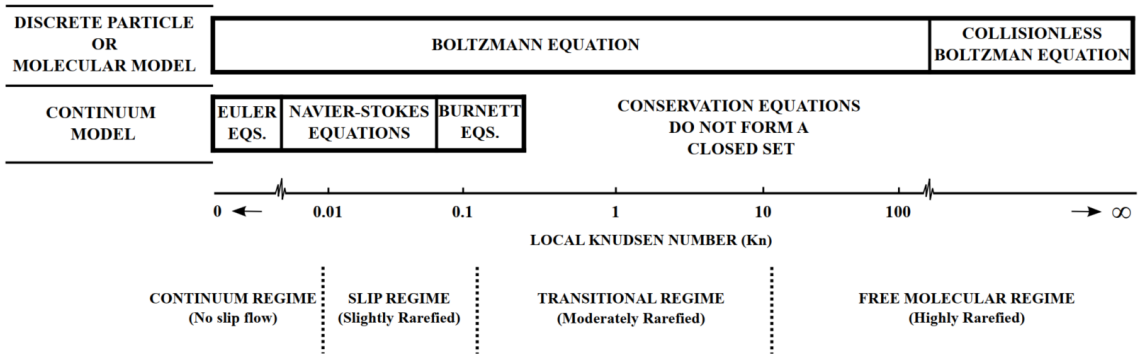

Figure 1.16: Mathematical models for different degrees of rarefaction as delimited by the Knudsen number [91].

As can be observed in Figure 1.16, the continuum regime in which the Navier-Stokes equations are valid is defined for a Knudsen number below 0.1. The Burnett equations can help to extend the upper limit of validity of the continuum models to a Knudsen number of 0.2. However, as rarefaction increases and the Knudsen number becomes significant, regions of non-equilibrium begin to appear near surfaces as molecule–surface interactions become less frequent [95]; thus, requiring the replacement of continuum models by molecular models. The region where $0.01 < \mathrm{Kn} < 10$ defines the transitional regime, where the continuum fluid equations are inaccurate and collisions cannot be neglected. For $\mathrm{Kn} > 10$, very few collisions occur within the gas and the flow is approximately free molecular. The only mathematical model capable of modeling the complete spectrum of flow rarefaction regimes is the Boltzmann equation. From a continuum perspective, at the limit of zero Knudsen number the transport terms vanish and the Navier-Stokes equations reduce to the inviscid Euler equations. The opposite limit of infinite Knudsen number is the free-molecule

flow regime, where the collisionless form of the Boltzmann equation applies. These mathematical models can be related through the Chapman-Enskog theory, where they can be derived by different order approximations of a common series expansion about these local Knudsen numbers.

Moreover, high gradients and small length scales, such as those within the strong shock layers associated with hypersonic flight, can further deviate the molecular velocity distribution function from equilibrium [96, 97]. To varying degrees depending on the mission, IAD vehicles are exposed to characteristic hypersonic flow phenomena during operation. This is because during the reentry process, where the kinetic energy of the spacecraft is dissipated into the atmosphere, these vehicles reach very high speeds. For Earth applications, depending on their altitude and/or orbit before descent, reentry vehicles can reach speeds on the order of 10^4 m/s. The hypersonic flow regime is characteristic of an object with a velocity considerably higher than the speed of propagation of the perturbations in the flow caused by the object, that is, when the speed of a gas flow (U_∞) around an object is significantly higher than the speed of sound (c_s) in the same medium. The ratio between both quantities can be described by the Mach number (Ma) as

$$\mathrm{Ma}_\infty = \frac{U_\infty}{c_s}. \tag{1.3}$$

Thus, a sufficiently large Mach number, Ma >> 1, would be indicative of a hypersonic flow regime. Reentry vehicles experience a range between 28 and 0 Mach during atmospheric reentry. Figure 1.17 shows the development of a flow around an airfoil for different Mach numbers, ranging from the subsonic to the hypersonic flow regime. A commonly used criterion to classify a flow as hypersonic is Ma > 5.

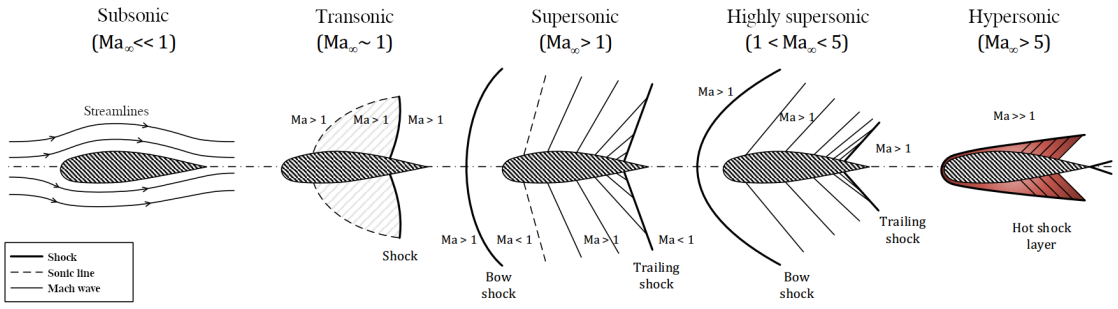

Figure 1.17: Schematic of the flow development around an airfoil for different Mach numbers.

However, hypersonic flow is best defined as the regime in which certain physical flow phenomena become progressively more important as the Mach number is increased to higher values. Some of these defining flow phenomena include: thin shock layers, strong entropy gradients, a large boundary layer, and high temperatures at and behind the shock wave. Figure 1.18 summarizes some of the important physical phenomena associated with hypersonic flight.

The effects of flow rarefaction also influence the nature of characteristic hypersonic flow phenomena.

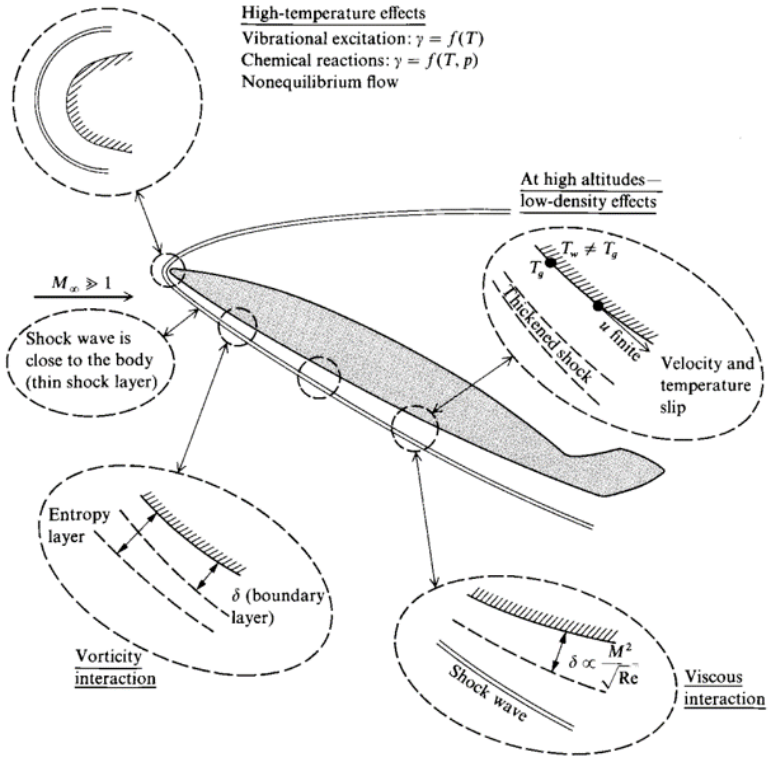

Figure 1.18: Schematic of important physical phenomena associated with hypersonic flight. [98]

For instance, it is worth noting that the mean free path is inversely proportional to the gas density, and, for a given shock strength, the width of the wave is also inversely proportional to the density. Moreover, the portion of the flow that is viscous increases as the flow becomes rarefied [91]. At extremely low densities, the shock waves and boundary layers merge and then lose their identities as the free molecular regime is approached. Outside boundary layers and shock waves, equilibrium continuum flow can be assumed and the Euler equations may be applied, yielding the correct results at all Knudsen numbers. Reentry vehicles, such as IADs, travel through rarefied flow fields dominated by compressibility effects. However, because of the speed of the vehicle, most of the flow in contact with the spacecraft is laminar in nature. This allows the thermal viscous effects on the surface of the spacecraft to be neglected [99], which simplifies the analysis. Nevertheless, flow rarefaction leads to velocity-slip and temperature-jump phenomena, in which the velocity and temperature in the gas adjacent to the surface are not equal to their corresponding values at the surface of the vehicle.

The limitations of traditional CFD techniques based on the continuum hypothesis and the difficulties associated with analytical solutions make these approaches inadequate to investigate the reentry of IADs under rarefied conditions. The importance of non-equilibrium effects and intermolecular collisions under this regime has made the stochastic particle-based Direct Simulation Monte Carlo (DSMC) method [91, 100] the standard method for aerospace investigations at high altitudes [95, 101, 102]. This method will be discussed in detail in section 2.2.

1.3 Previous work: CubeSat-based IAD technology

The first application of IAD technology for CubeSats reentry and recovery was proposed by Spaceflight Industries, then Andrews Space [103, 104]. The proposed CubeSat Deorbit and Recovery System (DRS) was a standalone device that used inflatable technology to shorten a spacecraft's lifetime by a factor of ten and potentially enabled controlled reentry and safe recovery of NanoSat and CubeSat class spacecraft. Attached to a standard 2U CubeSat module, the CubeSat DRS was a 1U module with an inflatable 1.2 m diameter tension-cone decelerator. The DRS design objectives included a standard CubeSat interface, the use of COTS, and a self-contained modular design. The Andrews Space team evaluated different types of DRS configurations and selected a DRS design with a 60° tension cone deployed using an inflatable torus, as shown in Figure 1.19. The team conducted component, subsystem, and system level testing to verify the performance and feasibility of a DRS prototype. Material testing assessed both the strength and thermal properties of the materials to withstand the reentry environment, while tests to the inflation system helped calibrate this system and derive inflation times. Based on these tests, several design improvements were identified, including the use of a finer weave in the material and a potential redesign of the inflation system. A demonstration mission to reenter and recover a 3U spacecraft from the ISS was formulated, but has not taken place to date.

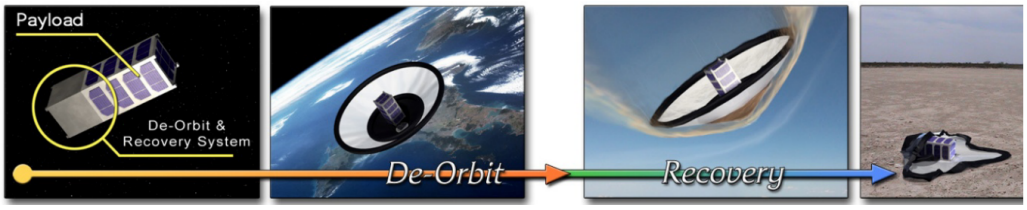

Figure 1.19: Andrews Space's CubeSat DRS system conceptual mission stages [103].

Important work on CubeSat-based IAD technology has been carried out by researchers from the University of Naples Federico II, who conducted preliminary feasibility analyzes on two concepts of mechanically deployable aerodynamic decelerators for CubeSats [25]. The first concept proposed, shown in Figure 1.20a, is the CubeSat End-of-Life System (CELS), which is intended to provide nanosatellites with the possibility of performing an aerodynamic deorbit maneuver. The objective of this concept is to deorbit without recovery, with the payload and deployable aerobrake disintegrating during atmospheric reentry. The second concept analyzed, shown in Figure 1.20b, is the CubeSat De-orbit and Recovery System (CDRS). In addition to the deorbit maneuver, the CDRS enables the safe reentry and recovery of CubeSat modules. This is achieved through the use of a flexible high-temperature heat shield that protects the CubeSat payload from the harsh reentry conditions. Similarly to other mechanically deployed reentry vehicles, the reference surface of the CDRS concept could be modulated by changing the half-cone angle to control the trajectory during descent. For CDRS, preliminary calculations of aerothermal and mechanical loads during reentry were performed, using numerical methods based on the Navier-Stokes equations to focus on the continuum regime

part of the reentry trajectory. Both reentry vehicles had a 45° forebody geometry configuration. As stated by the authors [25], this geometry configuration provided a good compromise between aerodynamic stability and the maximum available cross-section area in the deployed configuration for a given rod dimension.

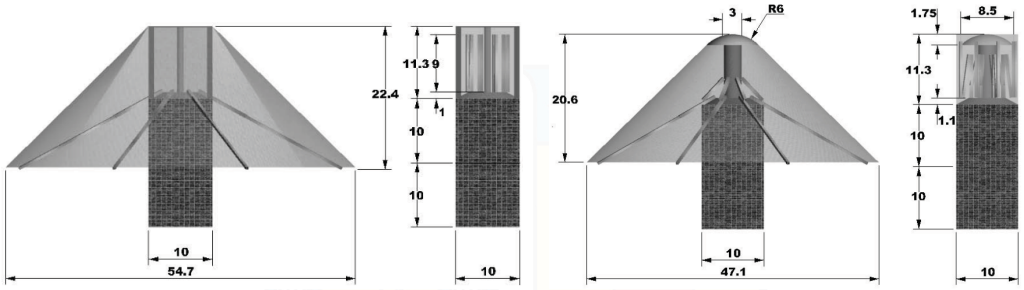

(a) CELS **(b)** CDRS

Figure 1.20: Mechanically deployable aerodynamic decelerators concepts for CubeSat applications [25].

Although not specifically applied to CubeSats, in a related study [105], two possible sphere–cone configurations for the TPS were investigated. As shown in Figure 1.21, the analyzed configurations had the same reentry mass and maximum diameter, but were characterized by different half-cone angles of 45° and 60°, referred to as TPS-45 and TPS-60, respectively. The analyzes involved both the evaluation of thermal and aerodynamic loads and the assessment of the capsule longitudinal stability. The aerothermodynamic analysis performed for both half-conce angles in deployed configuration considered transitional and continuum reentry regimes. From these analyzes, TPS-45 was shown to be more favorable than TPS-60 from a stability point of view [105, 106]. From the thermal and aerodynamic loads point of view, preliminary results showed TPS-60 to be more favorable than TPS-45 due to the steeper reentry trajectory and smaller radius of curvature of this latter geometry [105, 76].

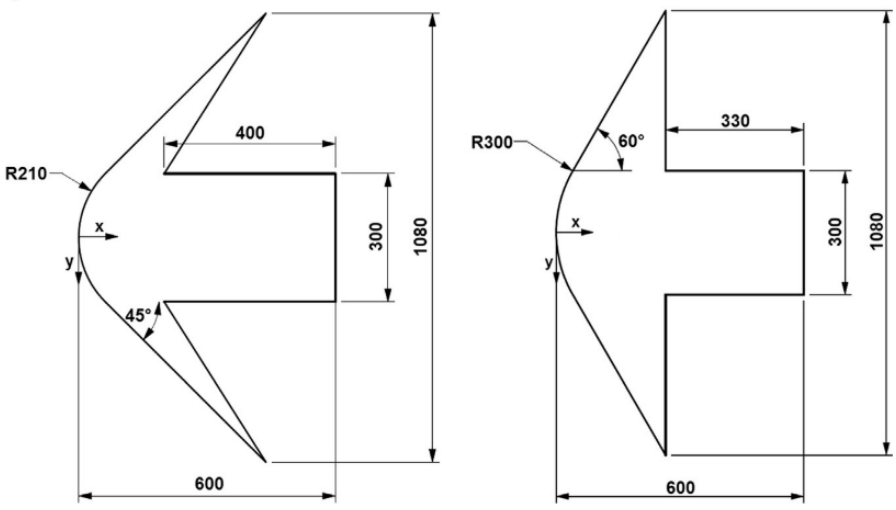

(a) TPS-60 **(b)** TPS-45

Figure 1.21: Geometrical characteristics of TPS-60 and TPS-45 [105].

Other numerical aerothermodynamic studies and aerodynamic control capability investigations carried out by researchers from the University of Naples Federico II [34, 107, 108, 109] have been mainly related to non-CubeSat applications. Namely, as described in section 1.1, the development of the IRENE and MINI-IRENE heat shields and the MISTRAL project. However, it should be noted that the proposed IPERDRONE.1 mission aims to safely return and recover a 3U CubeSat payload using the mechanically deployed IRENE heat shield [86, 87, 82].

In line with the basis established by the MAAC project [110], in 2017, JAXA successfully conducted a nanosatellite orbital deployment mission, the reentry satellite with gossamer aeroshell and GPS/Iridium (EGG) experiment [111, 112]. Before deployment, EGG could be compactly packed into a 3U CubeSat form factor. The inflatable thin-membrane aeroshell was approximately 0.8 m in diameter and had a flare angle of 60 degrees. The main components and general dimensions of the EGG spacecraft in deployed configuration are presented in Figure 1.22. EGG was deployed from the ISS and orbited in LEO for 120 days at an altitude of approximately 400 km before reentering the Earth's atmosphere and burning out according to mission schedule. Several investigations have been carried out on the EGG experiment and the data obtained during its reentry [112, 111, 113, 114]. In particular, the history of heat fluxes on the membrane aeroshell and the inflatable torus during descent was reconstructed based on the data measured by the thermocouples placed in the membrane of the aeroshell. The heat flux distribution was reproduced using the discrete particle-based Direct Simulation Monte Carlo method. The results indicated that, at an altitude of 110 km, the heat fluxes on the membrane aeroshell and the inflatable torus were approximately 2.8 and 4.0 kW/m^2, respectively. This latter value being the maximum heat flux experienced by the reentry vehicle at an altitude of 120 km. However, after the mission, post-flight analysis indicated that membrane aeroshell of EGG was deformed, highlighting the need for further investigation on the aerodynamic forces and aerodynamic heating environments causing this deformation [112].

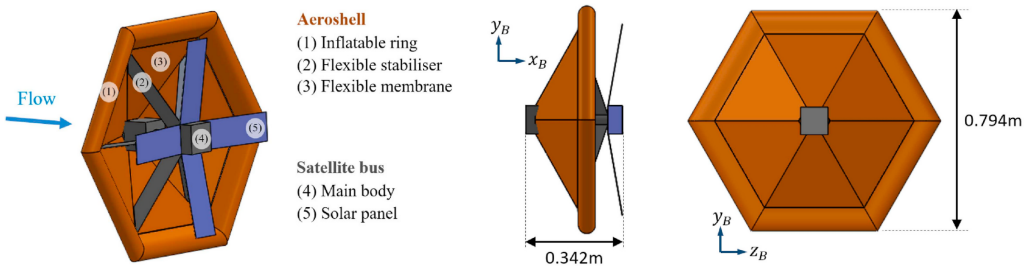

Figure 1.22: Main components and general dimensions of the EGG spacecraft in deployed configuration [111].

Similarly, NASA conducted the ADEPT SR-1 flight test in 2018 to evaluate the application of the ADEPT system for nanosatellites and secondary payloads (Nano-ADEPT) [32, 115]. The mission targeted a minimum separation altitude of 100 km for ADEPT SR-1 and a peak Mach number during entry of 3.0. When deployed, the SR-1 configuration was an octagonal pyramid with a spherical nose-cap aeroshell attached to a 3U CubeSat payload. In stowed configuration, the ADEPT umbrella structure could wrap around the

payload at an overall diameter of 0.24 m. The deployed configuration was 0.7 m in diameter and had a 70° half-cone angle, increasing the projected area by a factor of eight from the stowed configuration to the deployed configuration [115]. Figure 1.23a and Figure 1.23b show an overview of the mechanical system of nano-ADEPT and the SR-1 reentry vehicle itself, respectively. The suborbital mission was successful, meeting 5 of the 6 mission success criteria, and demonstrated the capability of the ADEPT system to achieve a fully deployed configuration before reaching an altitude of 80 km during descent [33]. However, the ADEPT SR-1 flight had an unexpected roll rate increase observed during the supersonic flight regime and also tumbled at speeds lower than Mach 0.2 [116]. In addition to this, reconstructed flight performance identified multiple limitations of the pre-flight aerodynamics database. Computational simulations were used to develop the ADEPT SR-1 static aerodynamics database, with non-continuum aerodynamics predicted using particle-based simulation methods [117]. In particular, the transitional regime data was generated for the ADEPT SR-1 geometry at altitudes from 115 to 75 km, that is, from Kn = 2.23 to Kn = 0.0023. Based on preliminary simulations, the ADEPT SR-1 model was assumed to behave as a rigid heatshield, without any mid-gore or rib deformation. The Direct Simulation Monte Carlo solvers MAP and DAC were used for the lower and higher density conditions in the aforementioned altitude range [117]. Large axial and normal coefficient values, $C_A \approx 2.4$ for 0° angle of attack at 105 km altitude, were observed at non-continuum conditions, but no details on the flow structure or surface properties were presented for this flow regime.

A higher altitude sounding rocket test, SR-2, is being considered to reach altitudes of 500 km, which would result in ADEPT SR-2 experiencing hypersonic flight conditions for a short duration [115]. Additionally, the Pterodactyl Project is analyzing various ADEPT configurations to study the efficacy of guidance and control architectures for DEVs, including axisymmetric configurations and flap-based control systems [118, 119].

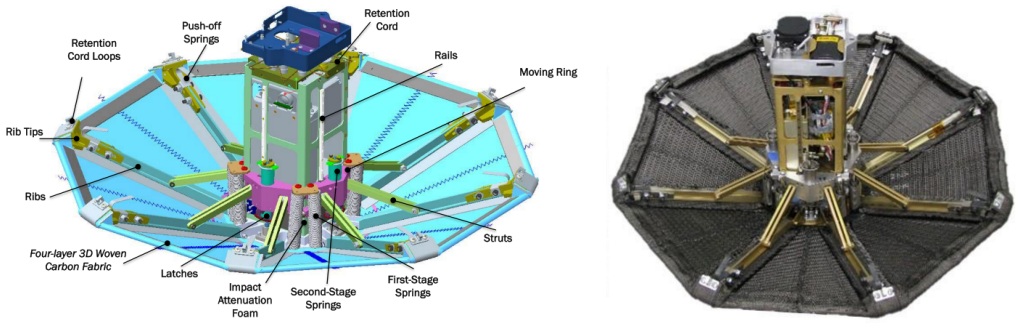

(a) SR-1 Mechanical systems [115]. **(b)** SR-1 reentry vehicle [33].

Figure 1.23: Overview of the nano-ADEPT SR-1 reentry vehicle.

Other relevant work includes the development of the DEployable, Self-regulating, CENTrifugally-stiffened decelerator (DESCENT) concept and its possible applications to CubeSat-sized vehicles [31, 120, 121]. The core design concept of DESCENT lies in the application of inertia forces for the deployment of a thin flexible heat shield. The shape of the shell generates an axial aerodynamic roll-torque that causes

autorotation during descent and produces a centrifugal force that stiffens and flattens the shell [31]. In Figure 1.24, two conceptual designs of DESCENT entry vehicles are presented. Initial studies focused on CubeSat-sized applications of DESCENT, demonstrating the capability of the system to reach near full deployment in hypersonic and supersonic flight regimes during LEO reentry [31]. A low-speed free-fall drop test from a height of 100 m was performed to verify key aspects of the simulation. According to the authors, Design 2 of DESCENT is found to enable a miniaturized vehicle to survive entry even when flipped over, thus eliminating the requirement for attitude control and providing a potential entry vehicle solution for miniaturized swarm-probes [121].

(a) Design 1 **(b)** Design 2

Figure 1.24: Conceptual designs of DESCENT entry vehicles [121]. (a) Design 1 uses a deployable first stage to minimise the stowed diameter. (b) Design 2 lacks the first stage and replaces it with a larger nose cone.

Lastly, the Self-DePloyable FLexible AeroSHell for de-Orbiting and Space Re-entry (SPLASH), a mechanically deployed aeroshell for the controlled reentry and safe recovery of CubeSats, is being developed by Italian and Brazilian researchers [122]. Unlike other mechanically deployed heat shields, such as the ADEPT 3U or ADEPT 12U aeroshell concepts, one of the key objectives of SPLASH is to integrate the entire morphing concept within a standard 12U CubeSat deployer, as shown in Figure 1.25a. The proposed concept is an umbrella-like system consisting of structural ribs and struts that are covered by a flexible thermal protection system (TPS). The preliminary geometry in deployed configuration consists of a sphere-cone angle of approximately 60 degrees and a base diameter of 0.8 m, as shown in Figure 1.25b. The project is still in its early stages, with future work involving the evaluation of thermal and aerodynamic loads and the assessment of aeroelastic stability. Once a full aerostructural analysis and numerical validation of the small-scale model is achieved, a demonstrator of a SPLASH morphing aeroshell will be fabricated at CIRA for functional testing.

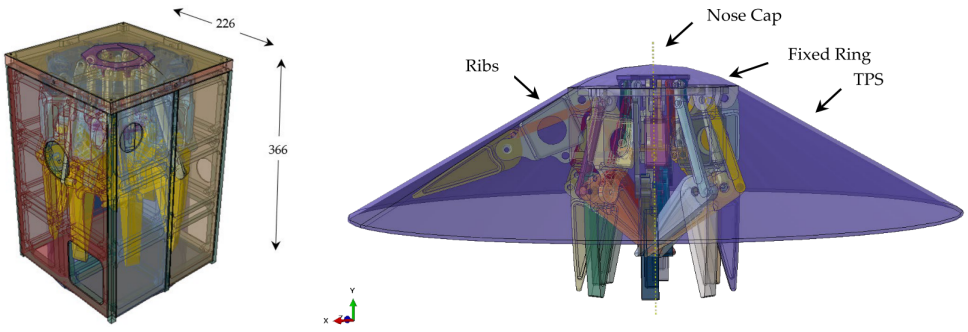

(a) Stowed configuration. **(b)** Aeroshell components.

Figure 1.25: SPLASH CubeSat IAD vehicle schematics in stowed and deployed configurations.

1.4 Project objectives

As explored in section 1.1, IAD technology has the potential to have a profound impact on the future framework of space activities, as it has the capability to expand and improve multiple aspects of spacecraft reentry. Furthermore, as demonstrated in section 1.3, there are several instances of IAD project applications to nanosatellite missions, with a substantial body of recent research that reflects growing interest in this field. There is a wide variety of IAD concepts being explored and many shield geometry configurations have been proposed. However, few aerothermodynamic analyzes on IAD technology for CubeSat reentry and recovery have been carried out, especially in regards to the rarefied flow regime.

The main objective of this project is to assess the impact of various forebody IAD geometries on the flowfield structure and surface properties during the initial stages of reentry, where spacecrafts are exposed to a significant degree of flow rarefaction. By doing so, this work aims to further extend the understanding of the flowfield around CubeSat-based IADs and help elucidate their optimum design requirements. In particular, numerical simulations are carried out on three distinct IAD configurations coupled with a 1U CubeSat during the upper stages of atmospheric reentry. The geometries considered in this study are assumed to be fully inflated, with a forebody radius of 0.3 m and three different cone angles of 68.8°, 45°, and fully rounded. Reentry of the IAD vehicles coupled with a 1U CubeSat payload was simulated considering nonreactive flow at 0° angle of attack and 105 km of altitude. Due to the high degree of flow rarefaction at this altitude, the Direct Simulation Monte Carlo method, implemented in the dsmcFoam+ solver, is used for all computations.

The specific objectives of this thesis are described as follows:

- Validation and verification of dsmcFoam+ for the study of CubeSat-based IADs in rarefied reentry conditions. For this purpose, two test cases of conditions similar to those employed in the main body of work of this investigation are used.
- Describe the flowfield structure around CubeSat-sized IADs confronted with hypersonic rarefied reentry conditions.
- Assess the influence of the IAD geometry on the macroscopic flow properties during reentry. In particular, the velocity, temperature, density, and pressure fields are carefully investigated and discussed.
- Investigate the effects of the forebody geometry on the surface properties of CubeSat-based IAD vehicles. To achieve this, the aerothermal coefficients and aerodynamic forces experienced by the three IAD geometries are thoroughly analyzed.
- Provide a useful resource for engineers and researchers developing IAD technology for CubeSat Reentry and Recovery.

1.5 Thesis outline

This chapter has delved into the importance of addressing the nanosatellite revolution to ensure the long-term sustainability of space affairs. It has provided a comprehensive overview of the major advancements in modern IAD technology, along with a description of the challenging reentry conditions that IADs may encounter. A review of previous research on CubeSat-based IADs was presented, from which the project objectives were laid out.

Chapter 2 focuses on the computational method employed for the simulations conducted in this thesis, the Direct Simulation Monte Carlo Method. Fundamental concepts of the kinetic theory of gases are provided to establish a theoretical basis for the explanation of the DSMC method. Then, a detailed description of the DSMC method is provided, encompassing the algorithms and physical models utilized.

The validation and verification of dsmcFoam+ is presented in **Chapter 3**. For the validation process, the results obtained from the dsmcFoam+ solver are directly compared to previous numerical studies. For the verification process, the main computational parameters for the accuracy of the DSMC method were tested.

In **Chapter 4**, the computational results regarding the investigation of inflatable aerodynamic decelerators for CubeSat reentry and recovery are thoroughly discussed. An analysis of the influence of the IAD geometry on the macroscopic flow properties during reentry is carried out. Then, the effects of the forebody geometry on the surface properties and aerodynamic forces are investigated.

Lastly, **Chapter 5** summarizes the main conclusions derived from this research and highlights potential future projects.

2 | Computational method

In the upper stages, atmospheric reentry is characterized by the presence of highly rarefied hypersonic flows. The flow physics at this region are quite complex with significant thermodynamic non-equilibrium and high macroscopic gradients in the shock wave and around the spacecraft. Under these conditions, the Direct Simulation Monte Carlo (DSMC) method has proven essential for the design and analysis of aerodynamic systems, studying spacecraft reentry systems, and comprehending hypersonic flow phenomena in the transitional flow regime. This chapter provides a comprehensive introduction to the fundamental principles of the kinetic theory of gases, which constitute an essential foundation of the DSMC method. The description of the DSMC method is the primary focus of this chapter and is detailed in section 2.2.

2.1 Fundamentals of kinetic theory

The kinetic theory of gases constitutes a fundamental framework in the study of gas dynamics, as its primary aim is to relate the microscopic behavior at the molecular level and the corresponding macroscopic properties observed in gases. Kinetic theory achieves this objective by delving into the dynamics of individual gas particles and subsequently aggregating their collective attributes to elucidate the macroscopic processes taking place in the gas flow. At the molecular scale, gas particles engage in two essential processes: translational motion within the spatial domain and intermolecular collisions with other particles in the gas. Through a comprehensive investigation of these processes, kinetic theory provides a model that incorporates the fundamental principles governing the behavior and properties of gases.

2.1.1 The molecular model

The molecular model recognizes the particulate nature of the gas, modeling its structure as a multitude of discrete molecules. This model aims to describe the behavior of a gas flow by providing detailed information on the position, velocity, and state of each individual molecule at all times. At this molecular or microscopic level, the appropriate mathematical model is the Boltzmann equation, which governs the evolution of the molecular distribution function of the gas particles in the flow. However, the direct application of the Boltzmann equation presents considerable challenges, as it generally lacks analytical solutions for nontrivial

problems and poses significant difficulties for conventional numerical methods. Nevertheless, the discrete structure of the gas at the molecular level enables these difficulties to be circumvented through direct physical modeling. That is, instead of solving a mathematical governing equation, the discrete nature of the gas is leveraged to explicitly account for the interactions and dynamics of individual molecules.

In the molecular model, a set of basic quantities is associated with each molecule. These include the number of molecules per unit volume, as well as the mass, size, velocity, and internal state of each individual molecule. These quantities play a crucial role in characterizing the molecular behavior in the gas. When related to the mean free path and collision frequency, these quantities help to establish the distance and time scales of the effects due to collisional interactions among the molecules.

The mass of a molecule is the sum of the masses of its constituent atoms. The structure of each atom within a real molecule is composed of a nucleus surrounded by orbiting electrons. The position of a molecule refers to the location of the center of mass of its constituent atoms, while the velocity of the molecule is the center-of-mass velocity of those atoms, as shown in Figure 2.1a. This consideration allows for a simplified representation of the molecule's motion and enables the analysis of its overall behavior at a macroscopic level. For diatomic and polyatomic molecules, the atomic motion relative to the center of mass, such as rotation and vibration, contributes to the internal energy of the particle. These additional degrees of freedom, depicted in Figure 2.1b and Figure 2.1c, respectively, influence the thermodynamic properties and energy distribution of these types of molecules.

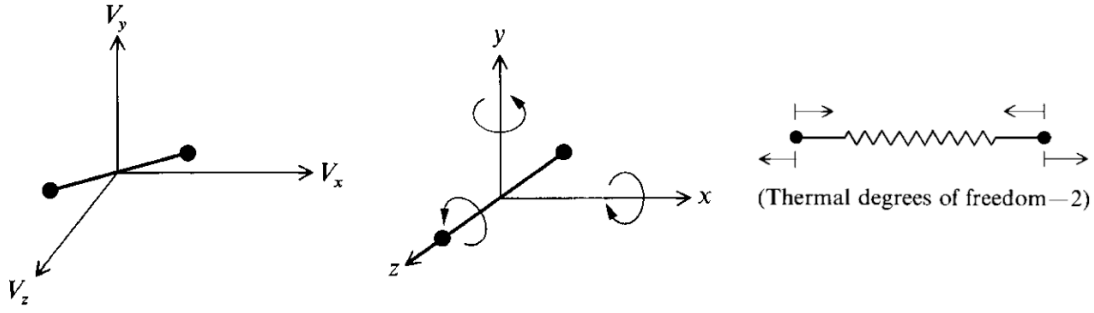

(a) Transalational energy **(b)** Rotational energy **(c)** Vibrational energy

Figure 2.1: Energy modes of a diatomic linear molecule [98].

Molecular size is a quantity that cannot be precisely and uniquely defined. However, its definition is fundamental for the qualification of the results derived from elementary kinetic theory, as it determines the nature of intermolecular collisions. In real collisions, particles interact through fields formed by the electrostatic Coulomb forces acting between the elementary charges of the interacting bodies. In this fashion, the force fields resulting from these interactions, which statistically can be assumed to be spherically symmetric, define the collision process between molecules. The general form of the force between two molecules as a function of the distance between their nuclei is illustrated in Figure 2.2. This figure illustrates that, at large distances of separation, there is a weak attractive force that brings individual molecules closer

together; whereas, at small distances of separation, strong repulsive forces push the molecules apart. For simple gas species, the weak attraction forces are typically negligible, except at very low gas temperatures. Therefore, in most cases, the modeling of the repulsive part of the potential field becomes the primary focus of interest.

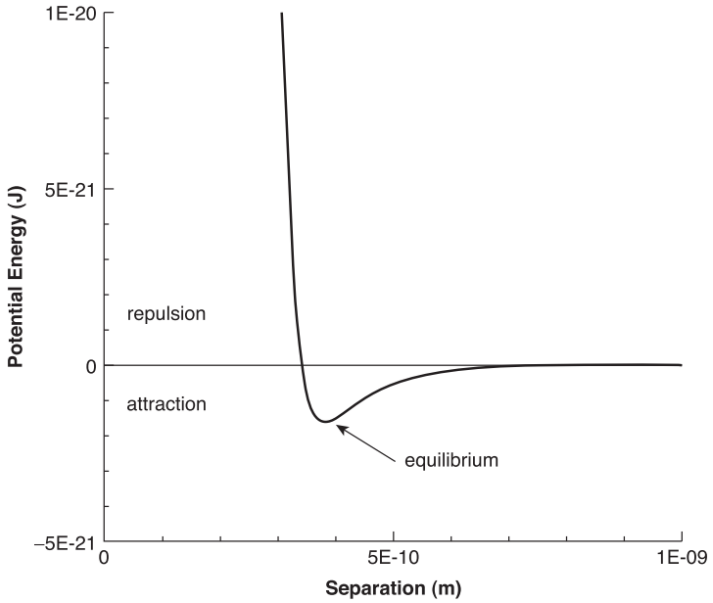

Figure 2.2: Representative interaction force field for two argon particles [100].

A hard elastic sphere provides a simplified but useful model of a molecule. The **hard sphere** (HS) model assumes that each particle can be represented as a rigid sphere with a specific diameter d. According to this model, two molecules collide if their trajectories are such that the distance between their centers decreases to their hard sphere diameter, as shown in Figure 2.3. Mathematically, this implies that the force field between two particles is zero everywhere except when the distance of separation is equal to the diameter of the molecules. The total collision cross-section (σ_T) for these molecules is

$$\sigma_T = \pi d^2. \tag{2.1}$$

It is important to note that the collision cross-section of realistic models is a function of the relative speed between the molecules and experience has shown that it is important to reproduce this behavior. The specific form of the force field and the resulting distribution of scattering angles in collisions are comparatively less important.

For simplicity and clarity, in this chapter, the terms particle and molecule will be used interchangeably to refer to monatomic, diatomic, or polyatomic molecules. Similarly, the discussion of the kinetic gas theory will be restricted to a **simple gas**, that is, a gas consisting of a single chemical species in which all molecules are assumed to have the same structure.

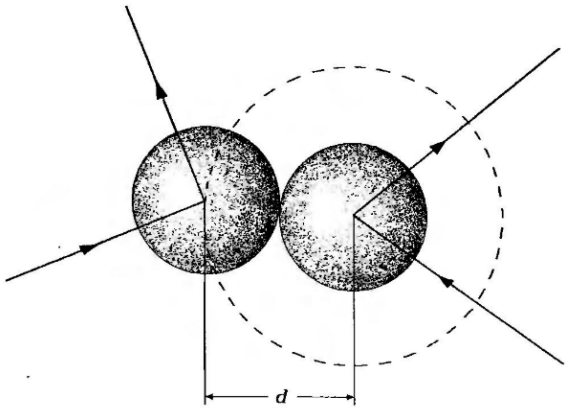

Figure 2.3: Collision between two hard sphere particles of diameter d [91].

2.1.2 The dilute gas

The number density (n) of a gas refers to the number of molecules per unit volume. This quantity depends on temperature and pressure; however, it remains unaffected by gas composition. Avogadro's law states that, at a given temperature and pressure, the volume occupied by one mole of any gas is the same for all gases. Since the average volume available to a molecule is given by $1/n$, the mean molecular spacing (δ) can be defined as

$$\delta = n^{-1/3}. \tag{2.2}$$

Thus, the proportion of space occupied by a gas molecule can be calculated as approximately $(d/\delta)^3$. Furthermore, from Equation 2.2, it can be deduced that, at sufficiently low densities, the molecular spacing δ is significantly larger than the effective molecular diameter d. This condition characterizes a dilute gas, which can be explicitly defined by the condition

$$\delta \gg d. \tag{2.3}$$

One of the key implications of the dilute gas assumption is that collisions are overwhelmingly likely to be binary collisions involving only one other molecule. In doing so, under the dilute gas assumption, the effect of three-body collisions can be statistically disregarded, only requiring two-body binary collisions to be considered. In non-dilute gases, three-body collisions must be accounted for, which significantly complicates the mathematical analysis.

Moreover, when dealing with dilute gases, the influence of intermolecular interactions on a particle's movement is largely negligible, as they are outside the range of influence of each other. This assumption allows for the decoupling of a molecule's movement from the effects of intermolecular collisions within

time scales smaller than the mean collision time. The mean collision time (τ_c) is the mean time between the successive collisions suffered by any particular molecule. The reciprocal of this quantity is the mean collision rate or collision frequency (ν) per molecule. For a dilute simple gas, the collision frequency can be defined as

$$\nu = n\,\overline{\sigma_{\mathrm{T}} c_{\mathrm{r}}}, \tag{2.4}$$

where $\overline{c_{\mathrm{r}}}$ is the relative velocity between the colliding particles. Thus, the total number of collisions (N_{c}) per unit time per unit volume can be calculated as

$$N_{\mathrm{c}} = \frac{1}{2} n\,\nu = \frac{1}{2} n^2 \overline{\sigma_{\mathrm{T}} c_{\mathrm{r}}}. \tag{2.5}$$

Under these conditions, the mean free path (λ) can be defined as the mean thermal speed ($\overline{c'}$) of the molecule divided by the collision frequency, that is,

$$\lambda = \frac{c'}{\nu} = \frac{\overline{c'}}{n\overline{\sigma_T c_{\mathrm{r}}}} \tag{2.6}$$

2.1.3 Macroscopic properties

To develop relationships between particle behavior and macroscopic gas flow quantities, some simple results based on a collection of particles are derived. As mentioned previously, each particle i can be assumed to have: a mass (m_i), a hard-sphere diameter (d_i), a position $\boldsymbol{r}_i = (r_1, r_2, r_3)_i$ and a velocity $\boldsymbol{c}_i = (c_1, c_2, c_3)_i$. The following paragraphs present simple relations for some of the most fundamental macroscopic gas flow properties, namely density, pressure, temperature, and velocity.

The first of the macroscopic properties to be discussed is the **density** (ρ). Consider a small volume (V) containing a total of N particles. The number density per unit volume can be calculated as

$$n = \frac{\sum_{i=1}^{N} 1}{V}, \tag{2.7}$$

Thus, the corresponding mass density can be determined by

$$\rho = \frac{\sum_{i=1}^{N} m_i}{V}. \tag{2.8}$$

This is defined as the mass per unit volume of the gas and is therefore equal to the product of the number of molecules per unit volume and the mass of an individual molecule, i.e.

$$\rho = nm. \tag{2.9}$$

The mass of an individual molecule can be calculated by diving the molecular weight (M_w) of the gas by Avogadro's constant ($\hat{N}$), 6.022×10^{23}. This result can also be derived by considering the flux vector of a quantity Q across a small gas element, that is,

$$n\overline{Q\boldsymbol{c}}. \tag{2.10}$$

When the quantity Q in Equation 2.10 is set equal to the mass of an individual molecule, the transport of mass across the element is obtained.

$$nm\overline{\boldsymbol{c}} = \rho\overline{\boldsymbol{c}}. \tag{2.11}$$

The thermal speed ($\boldsymbol{c}'$) describes the velocity of a molecule relative to the stream velocity of the flow. When describing a gas element from a frame of reference moving with the local stream velocity, Equation 2.10 can be expressed as

$$n\overline{Q\boldsymbol{c}'}. \tag{2.12}$$

When setting the quantity Q equal to the momentum vector $m\boldsymbol{c}$, a nine-component Cartesian tensor is obtained describing the **pressure** due to thermal motion,

$$\boldsymbol{p} = nm\overline{\boldsymbol{c}'\boldsymbol{c}'} = \rho\overline{\boldsymbol{c}'\boldsymbol{c}'}. \tag{2.13}$$

The individual terms of Equation 2.13 can be compactly described using Einstein's notation,

$$p_{i,j} = \rho\overline{c_i' c_j'}, \tag{2.14}$$

where the subscripts i and j range from one to three, describing each of the velocity components in three dimensional space. The scalar pressure p is usually defined as the average of the three normal components of the pressure tensor, that is,

$$p = \frac{1}{3}\rho\left(\overline{c_1'^2} + \overline{c_2'^2} + \overline{c_3'^2}\right) = \frac{1}{3}\overline{c_i'^2}. \tag{2.15}$$

The specific average kinetic energy associated with the thermal translational motion of a molecule can be defined as

$$e_{\text{tr}} = \frac{1}{2}\overline{c'^2}, \tag{2.16}$$

Thus, by relating Equation 2.15 and Equation 2.16, the translational energy can be expressed as

$$e_{\text{tr}} = \frac{3}{2}\frac{p}{\rho}. \tag{2.17}$$

Furthermore, from the ideal gas equation of state,

$$p = \rho RT = nk_bT, \tag{2.18}$$

the **translational temperature** (T_{tr}) can be related to the translational energy such that

$$RT_{\text{tr}} = \frac{2}{3}e_{\text{tr}}. \tag{2.19}$$

The universal gas constant (R) and the Boltzmann constant (k_b) are directly related through the molecular mass, so that $k_b = mR$. Therefore, by incorporating Equation 2.16, the translational temperature can be expressed as

$$T_{\text{tr}} = \frac{1}{3}\frac{m}{k_b}\overline{c'^2}. \tag{2.20}$$

In gases composed of monatomic molecules, particles have no internal structure and the translational energy constitutes the only mode of energy of the gas. On the other hand, diatomic and polyatomic molecules also possess internal energy associated with the rotational and vibrational energy modes. The corresponding **internal temperature** (T_{int}) can be defined based on the specific internal energy (e_{int}), so that

$$\frac{1}{2}\zeta RT_{\text{int}} = e_{\text{int}}, \tag{2.21}$$

where ζ is the number of internal degrees of freedom. For nonequilibrium gases, an overall kinetic temperature (T_{ov}) may be defined as the weighted average of the translational and internal energies, that is,

$$T_{\text{ov}} = \frac{3T_{\text{tr}} + \zeta T_{\text{int}}}{3 + \zeta}, \tag{2.22}$$

which is equivalent to the thermodynamic temperature for gases in equilibrium, where the translational and internal temperatures are the same.

2.1.4 Molecular collisions

Collisions provide the physical mechanism that pushes a gas toward equilibrium, while an insufficient number of collisions leads to nonequilibrium. As mentioned previously, in dilute gases, intermolecular collisions are mainly binary collisions involving two molecules. In this subsection, the binary elastic collision of two molecules of class $\boldsymbol{c}$ is analyzed. An elastic collision is defined as one in which there is no energy exchange between the translational and internal energy modes. Thus, in an elastic collision, the total linear momentum and kinetic energy of the colliding particles must be conserved. The pre-collision and post-collision velocities of particles in a binary collision may be denoted by $\boldsymbol{c}$ and $\boldsymbol{c}^*$, respectively. Thus, the conservation of momentum and energy in a binary elastic collision can be expressed as

$$m_1\boldsymbol{c}_1 + m_2\boldsymbol{c}_2 = m_1\boldsymbol{c}_1^* + m_2\boldsymbol{c}_2^* = (m_1 + m_2)\,\boldsymbol{c}_m, \tag{2.23}$$

and

$$m_1 c_1^2 + m_2 c_2^2 = m_1 c_1^{*2} + m_2 c_2^{*2}, \tag{2.24}$$

where the subscripts 1 and 2 identify the properties of each individual molecule, m is the mass of the corresponding molecule and $\boldsymbol{c}_m$ is the velocity of the center of mass of the pair of colliding molecules. The relative velocity between the colliding molecules before the collision, $\boldsymbol{c}_\mathrm{r} = \boldsymbol{c}_1 - \boldsymbol{c}_2$, can be used in combination with Equation 2.23 to give

$$\begin{aligned} \boldsymbol{c}_1 &= \boldsymbol{c}_m + \frac{m_2}{m_1 + m_2}\boldsymbol{c}_\mathrm{r}, \\ \boldsymbol{c}_2 &= \boldsymbol{c}_m - \frac{m_1}{m_1 + m_2}\boldsymbol{c}_\mathrm{r}. \end{aligned} \tag{2.25}$$

Similarly, using the relative velocity between the colliding molecules after the collision, $\boldsymbol{c}_\mathrm{r}^* = \boldsymbol{c}_1^* - \boldsymbol{c}_2^*$, from Equation 2.23 it can be derived that

$$\begin{aligned} \boldsymbol{c}_1^* &= \boldsymbol{c}_m + \frac{m_2}{m_1 + m_2}\boldsymbol{c}_\mathrm{r}^*, \\ \boldsymbol{c}_2^* &= \boldsymbol{c}_m - \frac{m_1}{m_1 + m_2}\boldsymbol{c}_\mathrm{r}^*. \end{aligned} \tag{2.26}$$

Equation 2.23 shows that the velocity of the center of mass is not affected by the collision. Similarly, Equation 2.25 and Equation 2.26 show that the pre- and post-collision velocities are antiparallel in the center of mass frame of reference. Furthermore, from these two equations, it can be shown that

$$\begin{aligned} m_1 c_1^2 + m_2 c_2^2 &= (m_1 + m_2)\, c_{\mathrm{m}}^2 + m_{\mathrm{r}} c_{\mathrm{r}}^2 \\ m_1 c_1^{*2} + m_2 c_2^{*2} &= (m_1 + m_2)\, c_{\mathrm{m}}^2 + m_{\mathrm{r}} c_{\mathrm{r}}^{*2}, \end{aligned} \tag{2.27}$$

where m_{r} is the reduced mass of the system, defined as

$$m_{\mathrm{r}} = \frac{m_1 m_2}{m_1 + m_2}. \tag{2.28}$$

From Equation 2.27 and Equation 2.24 it is easy to deduce that the magnitude of the relative velocity remains unchanged after the collision, that is, $c_{\mathrm{r}}^* = c_{\mathrm{r}}$.

If $\boldsymbol{F}$ is the force between two spherically symmetric point center of force molecules and $\boldsymbol{r}_1$ and $\boldsymbol{r}_2$ are their position vectors, the equations of motion of the molecules are

$$\begin{aligned} m_1 \ddot{\boldsymbol{r}}_1 &= \boldsymbol{F}, \\ m_2 \ddot{\boldsymbol{r}}_2 &= \boldsymbol{F}. \end{aligned} \tag{2.29}$$

From this description, it can be shown that the motion of the molecule of mass m_1 relative to the molecule of mass m_2 is equivalent to the motion of a molecule of mass m_{r} relative to a fixed center of force, that is,

$$\begin{aligned} m_1 m_2 \left(\ddot{\boldsymbol{r}}_1 - \ddot{\boldsymbol{r}}_2\right) &= (m_1 + m_2)\, \boldsymbol{F}, \\ m_{\mathrm{r}} \left(\ddot{\boldsymbol{r}}_1 - \ddot{\boldsymbol{r}}_2\right) &= \boldsymbol{F}. \end{aligned} \tag{2.30}$$

The analyses carried out in this subsection are summarized in Figure 2.4, where the transformation to and from the different frames of references employed is visually represented.

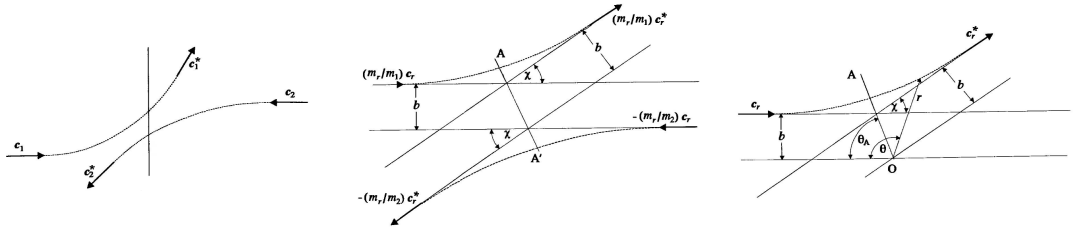

(a) Laboratory frame of reference **(b)** Mass frame of reference **(c)** Fixed center of force reference

Figure 2.4: Frames of reference for the analysis of binary collisions [91].

Figure 2.4 also shows that, due to the conservation of angular mometum, the projected distance (b)

between post-collision and pre-collision velocities is the same. The symmetry about the apse line allows for the definition of the inverse collision to the one just analyzed, that is, from molecules of class $\boldsymbol{c}^*$ to molecules of class $\boldsymbol{c}$.

From this description of binary elastic collisions, it can also be noted that both $\boldsymbol{c}_\mathrm{m}$ and $\boldsymbol{c}_\mathrm{r}$ can be defined based on the pre-collision velocities. Therefore, the complete determination of the post-collision velocities reduces to the calculation of the change in direction χ of the relative velocity vector.

Apart from the translational velocities of the two collision partners, two impact parameters are required to fully specify a binary elastic collision between spherically symmetric molecules. The first is the distance of closest approach (b) of the undisturbed trajectories in the center of mass frame of reference. The second impact parameter is chosen as the angle ϵ between the collision plane and some reference plane. As shown in Figure 2.5, the plane in which the trajectories lie in the center of mass frame is called the collision plane, and the line of intersection of the collision and reference plane is parallel to $\boldsymbol{c}_\mathrm{r}$. The differential cross-section ($\sigma d\Omega$) for the collision specified by the impact parameters b and ϵ is defined by

$$\sigma \mathrm{d}\Omega = b\ \mathrm{d}b\ \mathrm{d}\epsilon, \tag{2.31}$$

where $d\Omega$ is the unit solid angle about the vector $\boldsymbol{c}_\mathrm{r}^*$. From Figure 2.5 it can be deduced that $\mathrm{d}\Omega = \sin\chi \mathrm{d}\chi d\epsilon$ and $\sigma = (b/\sin\chi)|\mathrm{d}b/\mathrm{d}\chi|$. Thus, the total collision cross-section can be defined by

$$\sigma_\mathrm{T} = \int_0^{4\pi} \sigma \mathrm{d}\Omega = 2\pi \int_0^{\pi} \sigma \sin\chi \mathrm{d}\chi \tag{2.32}$$

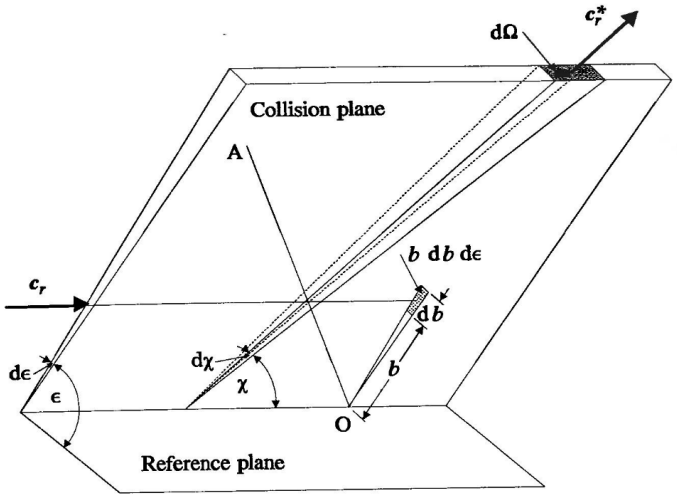

Figure 2.5: Impact parameters schematic [91].

For hard sphere molecules, σ is independent of χ and the scattering is isotropic in the center of mass frame of reference; that is, all directions are equally likely for $\boldsymbol{c}_\mathrm{r}^*$.

2.1.5 Velocity distribution function

A gas flow would be completely described by the position, velocity, and internal state of every molecule at a particular instant. However, the number of molecules in a real gas, even in a dilute gas, is so large that such a description is unfeasible. Instead, a statistical description in terms of probability distributions must be employed. When considering a sample of homogeneous gas containing N identical molecules, the three-dimensional physical space where particles move is defined by the Cartesian axes r_1, r_2 and r_3. Analogously, the velocity space is defined by the velocity components in Cartesian coordinates c_1, c_2 and c_3. As shown in Figure 2.6, each molecule can be represented in this space by the point defined by its velocity vector. For a gas molecule of velocity $\boldsymbol{c}$, the velocity distribution function $f(c)$ is defined by

$$\mathrm{d}N = Nf(\boldsymbol{c})\mathrm{d}\boldsymbol{c}, \tag{2.33}$$

where $\mathrm{d}N$ is the number of molecules in the sample with velocity components within the element $\boldsymbol{c} + \mathrm{d}\boldsymbol{c}$. Since both $\mathrm{d}N$ and N refer to the molecules in the same volume of physical space, the fraction of molecules within the velocity space element $\mathrm{d}\boldsymbol{c}$ can be expressed as

$$\mathrm{d}n/n = f\mathrm{d}\boldsymbol{c}, \tag{2.34}$$

where f is used instead of $f(\boldsymbol{c})$ for brevity. This distribution function is normalized, as its integration over all velocity space yields unity, that is,

$$\int_{-\infty}^{\infty} f \, \mathrm{d}c = N/N = 1. \tag{2.35}$$

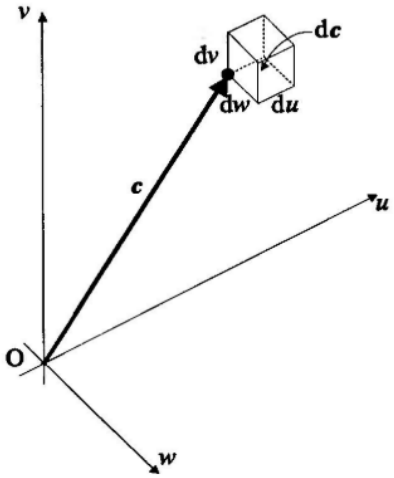

Figure 2.6: Molecule and element in velocity space [91].

The macroscopic flow properties are generally functions of position ($\boldsymbol{r}$) and time (t). A volume element in physical space may be denoted as d$\boldsymbol{r}$. Hence, the product d$\boldsymbol{r}$d$\boldsymbol{c}$ describes a volume element in the phase space, which is the multidimensional space formed by the combination of physical space and velocity space. Therefore, when used in a context in which $f(\boldsymbol{c})$ also depends on position and velocity, the single particle distribution function in phase space can be defined as

$$\mathrm{d}N = nf(\boldsymbol{c})\mathrm{d}\boldsymbol{c}\ \mathrm{d}\boldsymbol{r}, \tag{2.36}$$

where dN now represents the number of molecules in the phase space element d$\boldsymbol{c}$d$\boldsymbol{r}$. Note that the integration of nf in Eq. 2.36 over the entire phase space yields the total number of molecules in the system N rather than unity. At any instant, a complete system of N monatomic molecules can be represented by a point in the $6N$ dimensional phase space. In an ensemble of such systems, the probability of finding a system in the volume element $\mathrm{d}\boldsymbol{c}_1\mathrm{d}\boldsymbol{c}_2\ldots\mathrm{d}\boldsymbol{c}_N\ \mathrm{d}\boldsymbol{r}_1\mathrm{d}\boldsymbol{r}_2\ldots\mathrm{d}\boldsymbol{r}_N$ about the phase space point $\boldsymbol{c}_1, \boldsymbol{r}_1, \boldsymbol{c}_2, \boldsymbol{r}_2, \ldots, \boldsymbol{c}_N, \boldsymbol{r}_N$ is

$$F^{(\mathrm{N})}\left(\boldsymbol{c}_1, \boldsymbol{r}_1, \boldsymbol{c}_2, \boldsymbol{r}_2, \ldots, \boldsymbol{c}_N, \boldsymbol{r}_N, t\right)\mathrm{d}\boldsymbol{c}_1\ \mathrm{d}\boldsymbol{c}_2\ldots\mathrm{d}\boldsymbol{c}_N\mathrm{d}\boldsymbol{r}_1\ \mathrm{d}\boldsymbol{r}_2\ldots\mathrm{d}\boldsymbol{r}_N, \tag{2.37}$$

thus defining the N particle distribution function $F^{(\mathrm{N})}$, where the subscript denotes the number of the molecule, from 1 to N. A reduced distribution function $F^{(\mathrm{R})}$ for R of the N molecules is defined by

$$F^{(\mathrm{R})}\left(\boldsymbol{c}_1, \boldsymbol{r}_1, \boldsymbol{c}_2, \boldsymbol{r}_2, \ldots, \boldsymbol{c}_R, \boldsymbol{r}_R, t\right) = \int_{-\infty}^{\infty}\int_{-\infty}^{\infty} F^{(\mathrm{N})}\mathrm{d}\boldsymbol{c}_{R+1}\ldots\mathrm{d}\boldsymbol{c}_N\mathrm{d}\boldsymbol{r}_{R+1}\ldots\mathrm{d}\boldsymbol{r}_N. \tag{2.38}$$

The single particle distribution function $F^{(1)}(\boldsymbol{c}_1, \boldsymbol{r}_1, t)$, obtained by setting $R = 1$, is the probability of finding molecule number 1 in the phase space element $\mathrm{d}\boldsymbol{c}_1\mathrm{d}\boldsymbol{r}_1$ at time t irrespective of the position of the other $N - 1$ molecules. The two particle distribution function $F^{(2)}(\boldsymbol{c}_1, \boldsymbol{r}_1, \boldsymbol{c}_2, \boldsymbol{r}_2, t)$ is of particular importance when considering binary collisions in a dilute gas. In such a gas, the large molecular spacing allows the principle of **molecular chaos** to be valid. This principle assumes that the probability of finding a pair of molecules in a particular two particle configuration is simply the product of the probabilities of finding the individual molecules in the two corresponding one particle configurations, that is,

$$F^{(2)}\left(\boldsymbol{c}_1, \boldsymbol{r}_1, \boldsymbol{c}_2, \boldsymbol{r}_2, t\right) = F^{(1)}\left(\boldsymbol{c}_1, \boldsymbol{r}_1, t\right)F^{(1)}\left(\boldsymbol{c}_2, \boldsymbol{r}_2, t\right). \tag{2.39}$$

Although higher-order distribution functions are required for the study of dense gases, the single particle distribution function provides an adequate description of dilute gases. In general, the dimensions of the phase space are equal to the least number of scalar variables that are required to specify the position, velocity, orientation, and internal state of a molecule. Separate distribution functions are required for each species of a gas mixture.

2.1.6 The Boltzmann equation

The velocity distribution functions provide a statistical description of gas molecules at the microscopic level. A relationship between the distribution functions and the variables on which they depend can be established through the Boltzmann equation. For a simple dilute gas, this equation is

$$\frac{\partial}{\partial t}(nf) + c \cdot \frac{\partial}{\partial \boldsymbol{r}}(nf) + \boldsymbol{F} \cdot \frac{\partial}{\partial \boldsymbol{c}}(nf) = \int_{-\infty}^{\infty} \int_{0}^{4\pi} n^2 \left(f^* f_1^* - f f_1\right) c_r \sigma \mathrm{d}\Omega \mathrm{d}c_1. \tag{2.40}$$

Each of the terms in Equation 2.40 will be described in this subsection, as they provide valuable insight on the physical processes that take place within a homogeneous gas. At a particular instant, the number of molecules in the phase space element $\mathrm{d}\boldsymbol{c}\mathrm{d}\boldsymbol{r}$ is given by $nf\mathrm{d}\boldsymbol{c}\mathrm{d}\boldsymbol{r}$. If the location and shape of the element are assumed constant, the first term of Equation 2.40 describes the rate of change of the number of molecules in the element, that is,

$$\frac{\partial}{\partial t}(nf)\mathrm{d}\boldsymbol{c}\mathrm{d}\boldsymbol{r}, \tag{2.41}$$

The remaining terms of Equation 2.40 describe the processes that contribute to the change in the number of molecules within $\mathrm{d}\boldsymbol{c}\mathrm{d}\boldsymbol{r}$. These processes are illustrated in Figure 2.7 and will be briefly described independently.

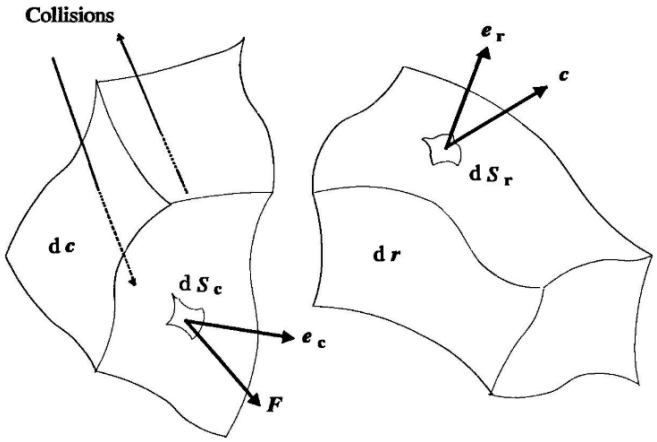

Figure 2.7: Molecular flux to and from a phase space element $\mathrm{d}\boldsymbol{c}\mathrm{d}\boldsymbol{r}$ [91].

The second term of Equation 2.40 describes the convection of molecules across the face of $\mathrm{d}\boldsymbol{r}$ by the molecular velocity ($\boldsymbol{c}$). The molecular velocity $\boldsymbol{c}$ is considered constant within $\mathrm{d}\boldsymbol{r}$, and $\mathrm{d}\boldsymbol{c}$ is considered to be located at the point defined by $\boldsymbol{r}$. The number density of class $\boldsymbol{c}$ molecules within $\mathrm{d}\boldsymbol{r}$ is $nf\mathrm{d}\boldsymbol{c}$. Therefore, the net inflow of molecules of this class across the surface of $\mathrm{d}\boldsymbol{r}$ (S_r) can be expressed as

$$-\int_{S_r} nf\boldsymbol{c}\cdot\boldsymbol{e}_r \mathrm{d}S_r \mathrm{d}\boldsymbol{c}, \tag{2.42}$$

where $\mathrm{d}S_r$ is a differential element of the surface S_r and $\boldsymbol{e}_r$ is the corresponding unit normal vector of this element. Since nf and $\boldsymbol{c}$ are constant within $\mathrm{d}\boldsymbol{r}$, and using Gauss' theorem, Equation 2.42 can be written as

$$-\nabla\cdot(nfc)\mathrm{d}\boldsymbol{r}\ \mathrm{d}\boldsymbol{c}. \tag{2.43}$$

Since only molecules of class $\boldsymbol{c}$ are considered, the velocity $\boldsymbol{c}$ may be taken outside the divergence in physical space. Therefore, the inflow of molecules of class $\boldsymbol{c}$ across the surface of $\mathrm{d}\boldsymbol{r}$ due to the velocity $\boldsymbol{c}$ is

$$-\boldsymbol{c}\cdot\frac{\partial(nf)}{\partial\boldsymbol{r}}\ \mathrm{d}\boldsymbol{c}\ \mathrm{d}\boldsymbol{r}, \tag{2.44}$$

corresponding to the second term in Equation 2.40. The third term in Equation 2.40 describes the convection of molecules across the surface of $\mathrm{d}\boldsymbol{c}$ as a result of the external force per unit mass $\boldsymbol{F}$. The effect of the acceleration $\boldsymbol{F}$ on the molecules in $\mathrm{d}\boldsymbol{c}$ is analogous to the effect of the velocity $\boldsymbol{c}$ on the molecules in $\mathrm{d}\boldsymbol{r}$. Thus, the inflow of molecules across the surface of $\mathrm{d}\boldsymbol{c}$ due to the external force $\boldsymbol{F}$ may be defined as

$$-\boldsymbol{F}\cdot\frac{\partial(nf)}{\partial c}\ \mathrm{d}\boldsymbol{c}\ \mathrm{d}\boldsymbol{r}. \tag{2.45}$$

The last term of Equation 2.40 describes the scattering of molecules into and out of the element $\mathrm{d}\boldsymbol{c}\mathrm{d}\boldsymbol{r}$ as a result of molecular collisions. In a dilute gas, collisions are assumed to be an instantaneous event in a fixed location in physical space. Therefore, as shown in Figure 2.7, molecular collision only affect the velocity space element $\mathrm{d}\boldsymbol{c}$, as the particle remains at the same point in physical space and time. In a binary collision of class $\boldsymbol{c},\boldsymbol{c}_1\rightarrow\boldsymbol{c}^*,\boldsymbol{c}_1^*$, the number of collisions per unit time suffered by a test particle moving with speed c_r among stationary field molecules of class $\boldsymbol{c}_1$ is

$$nf_1 c_r \sigma d\Omega d\boldsymbol{c}_1, \tag{2.46}$$

where f_1 denotes the value of the distribution function f at $\boldsymbol{c}_1$. Since the number of class $\boldsymbol{c}$ molecules in the phase space element is $nfd\boldsymbol{c}d\boldsymbol{r}$, the number of class $\boldsymbol{c},\boldsymbol{c}_1\rightarrow\boldsymbol{c}^*,\boldsymbol{c}_1^*$ collisions per unit time in the element is

$$n^2 f f_1 c_r \sigma d\Omega d\boldsymbol{c}_1 \, d\boldsymbol{c} \, d\boldsymbol{r}. \tag{2.47}$$

Similarly, the inverse collision of class $\boldsymbol{c}^*, \boldsymbol{c}_1^* \rightarrow \boldsymbol{c}, \boldsymbol{c}_1$ for the scattering of molecules into class $\boldsymbol{c}$ in the phase element $d\boldsymbol{c}^* d\boldsymbol{c}$ yields

$$n^2 f^* f_1^* c_r^* (\sigma d\Omega)^* \, d\boldsymbol{c}_1^* \, d\boldsymbol{c}^* \, d\boldsymbol{r}. \tag{2.48}$$

Due to $c_r^* = c_r$ and the symmetry between direct and inverse collisions, Equation 2.48 can be expressed as

$$n^2 f^* f_1^* c_r \sigma d\Omega d\boldsymbol{c}_1 \, d\boldsymbol{c} \, d\boldsymbol{r}. \tag{2.49}$$

The rate of increase of molecules of class $\boldsymbol{c}$ in the phase space element $d\boldsymbol{c}d\boldsymbol{r}$ as a result of the combined effect of direct and inverse collisions of class $\boldsymbol{c}, \boldsymbol{c}_1 \leftrightarrow \boldsymbol{c}^*, \boldsymbol{c}_1^*$ is obtained by subtracting the loss rate from the gain rate. Thus, subtracting Equation 2.49 from Equation 2.47 gives

$$n^2 \left(f^* f_1^* - f f_1 \right) c_r \sigma d\Omega d\boldsymbol{c}_1 \, d\boldsymbol{c} \, d\boldsymbol{r}. \tag{2.50}$$

Term four in Equation 2.40 is obtained by integrating Equation 2.50 over the complete cross-section and velocity space of class $\boldsymbol{c}_1$. Therefore, the total rate of increase of molecules of class $\boldsymbol{c}$ in the element as a result of collisions is

$$\int_{-\infty}^{\infty} \int_{0}^{4\pi} n^2 \left(f^* f_1^* - f f_1 \right) c_r \sigma d\Omega d\boldsymbol{c}_1 \, d\boldsymbol{c} \, d\boldsymbol{r}. \tag{2.51}$$

The Boltzmann equation for a simple dilute gas, described in Equation 2.3, is obtained by arranging Equation 2.41, Equation 2.44, Equation 2.45 and Equation 2.51 and dividing the complete equation by $d\boldsymbol{c}d\boldsymbol{r}$. The fourth term on the right-hand side of the Boltzmann equation, described in Equation 2.51, is called the collision term. Its integral form contrasts with the partial differential form of the terms that express the space and time dependence of the velocity distribution function and is responsible for much of the mathematical difficulty associated with the Boltzmann equation.

As can be noticed from Equation 2.40, nf is the only dependent variable in the Boltzmann equation. This is achieved by adding the velocity space coordinates to the list of independent variables. In doing so, while for a one-dimensional flow in physical space the Boltzmann solution becomes a three-dimensional problem, for two- and three-dimensional flows the problems become five- or six-dimensional. Then, a time

dimension needs to be considered if the problem is unsteady. Hence, the analytical solution of the Boltzmann equation for flows that involve complex geometries or large disturbances becomes unfeasible.

2.1.7 Equilibrium and the Maxwell distribution

A gas that is completely isolated from any outside influence may be regarded in equilibrium state if it remains undisturbed for a time that is sufficiently long in comparison with the mean collision time exhibited by molecules. If the number of molecules in the volume is sufficiently large, a gas in equilibrium has no gradients in the macroscopic properties with either distance or time, as statistical fluctuations at the microscopic level may be neglected. If the macroscopic gradients in a gas flow are sufficiently small and the collision rate is sufficiently high, the velocity distribution of each element of the gas adjusts to the equilibrium state appropriate to the local macroscopic properties as it moves through the gas. Each of these elements may be regarded as being in local thermodynamic equilibrium, with no variation in the velocity distribution function in time or space. Since the velocity distribution function remains constant in this finite region, the left-hand side of Equation 2.40 must be zero. Thus, the right-hand side of Equation 2.40, the collision term, must also be zero. This requirement yields the principle of detailed balance, described by

$$f^* f_1^* - f f_1 = 0 \tag{2.52}$$

This general principle found in all systems governed by finite-rate processes states that at equilibrium the rate of change in the number of molecules in the element $\mathrm{d}\boldsymbol{c}\mathrm{d}\boldsymbol{r}$ of class $\boldsymbol{c}$ is equal to the rate of change of molecules into class $\boldsymbol{c}^*$, that is,

$$\boldsymbol{c}, \boldsymbol{c}_1 \rightarrow \boldsymbol{c}^*, \boldsymbol{c}_1^* \equiv \boldsymbol{c}, \boldsymbol{c}_1 \leftarrow \boldsymbol{c}^*, \boldsymbol{c}_1^* \tag{2.53}$$

The principle of detailed balance, Equation 2.52 may also be written as

$$\ln f + \ln f_1 = \ln f^* + \ln f_1^*. \tag{2.54}$$

Thus, there is a certain function, $\ln f$, whose sum for the two particles in a collision does not change as a result of the collision, that is, a summational invariant. A general form solution to Equation 2.54 can be adopted on the basis of the linear combination of other collisional invariant molecule properties; such as mass, momentum and kinetic energy. Specifically,

$$\ln f = A1/2mc^2 + \boldsymbol{B} \cdot m\boldsymbol{c} + C, \tag{2.55}$$

where A, $\boldsymbol{B}$ and C are constants. Equation 2.55 may be expressed in terms of the thermal velocity ($\boldsymbol{c}'$) and stream velocity ($\boldsymbol{c}_0$) as

$$\ln f = A\frac{1}{2}mc'^2 + m\left(A\boldsymbol{c}_0 + \boldsymbol{B}\right)\cdot\boldsymbol{c}' + A\frac{1}{2}mc_0^2 + \boldsymbol{B}\cdot m\boldsymbol{c}_0 + C. \tag{2.56}$$

Due to the isotropic nature of a gas in equilibrium, the coefficient of $\boldsymbol{c}'$ must be zero. Hence, it can be shown that $\boldsymbol{B} = -A\boldsymbol{c}_0$ and, therefore, Equation 2.56 may be written as

$$f = \exp\left(\frac{1}{2}Amc^2 - \frac{1}{2}Amc_0^2 + C\right). \tag{2.57}$$

The introduction of a new constant β, such that $\beta = \frac{1}{2}Am$, gives

$$f = \exp\left(C + \beta^2 c_0^2\right)\exp\left(-\beta^2 c^2\right), \tag{2.58}$$

and the normalization condition, described in Equation 2.35, allows the elimination of the constant C so that

$$\exp\left(C + \beta^2 c_0^2\right) = \beta^3/\pi^{3/2}. \tag{2.59}$$

Therefore, the equilibrium or **Maxwellian distribution** function f_0 is

$$f_0 = \left(\beta^3/\pi^{3/2}\right)\exp\left(-\beta^2 c^2\right), \tag{2.60}$$

and the constant β may be related to the temperature of the gas such that

$$\beta^2 = (2RT)^{-1} = m/(2k_bT). \tag{2.61}$$

Further details on the Maxwellian distribution function and its more relevant measurements, as well as representative plots, are widely described in the available technical literature [91, 100, 123, 124].

As mentioned in section 1.2, the continuum approach is valid only for flows in which the departure from the equilibrium Maxwellian distribution is small. At higher altitudes, the deviation of the velocity distribution function of the freestream particles from the equilibrium distribution becomes significant. Furthermore, high gradients and small length scales, such as those within the strong shock layers associated with hypersonic flight, can further deviate the molecular velocity distribution function from equilibrium. Thus, the investigation of the complex physical phenomena in flows of this kind requires explicit consideration of the molecular nature of the gas.

2.2 Direct Simulation Monte Carlo

The Direct Simulation Monte Carlo (DSMC) method is a numerical technique that leverages principles of molecular dynamics to simulate complex gas flows. This approach is particularly suited for the simulation of rarefied gases, especially in the transitional flow regime. As detailed in section 1.2, this flow regime is characterized by a significant degree of flow rarefaction and important non-equilibrium phenomena, where conventional continuum numerical methods fail to provide accurate solutions. The governing equation for this flow regime is the Boltzmann equation. The DSMC method emulates the physics of the Boltzmann equation [123], as it is based on the same principles of classical kinetic theory and physical hypotheses underlying the derivation of this governing equation. In DSMC, this is achieved by simulating the motion and collisions of a large number of representative gas molecules, which in turn replicate the behavior of the real gas. In doing so, the DSMC method provides an indirect solution to the Boltzmann equation while avoiding the mathematical difficulties associated with the collision term. Furthermore, the stochastic particle nature of the DSMC method allows for easy integration of models for advanced physics that often cannot be formulated within the Boltzmann equation.

In the DSMC method, the properties of computer particles that compose the simulated flow are the same as those of real molecules; that is, position coordinates, velocity components, and internal state. The state of each simulated particle is stored and modified with time as particles move, collide and interact with surfaces and boundaries in the simulated physical space. All DSMC simulations are unsteady in nature, but steady state may be attained as the large-time state of unsteady flow, just as it occurs for real gases. In this sense, the time parameter in the simulation may be identified with the physical time in the real flow.

The DSMC method is subject to the same assumptions as the Boltzmann equation, in particular, the requirement of molecular chaos and a dilute gas. The dilute gas assumption implies three essential approximations in DSMC simulations:

- Molecular motion and intermolecular collisions can be decoupled over small time intervals on the order of the local mean collision time. Hence, simulated DSMC molecules can move in straight lines for a fraction of their mean collision time without any loss in accuracy.
- The impact parameters and initial orientations of colliding molecules can be assumed random, as there is no inherit bias in these parameters and they do not need to be deterministically simulated.
- Based on statistical arguments, only a small fraction needs to be simulated to obtain an accurate molecular description of the flow. Thus, the number of molecules can be reduced to a manageable level by regarding each simulated molecule as representing a fixed number F_N of real molecules.

An example of this last approximation is shown in Figure 2.8, where a range of molecular velocities of real molecules of a non–Maxwellian gas are represented by a reduced number of DSMC particles.

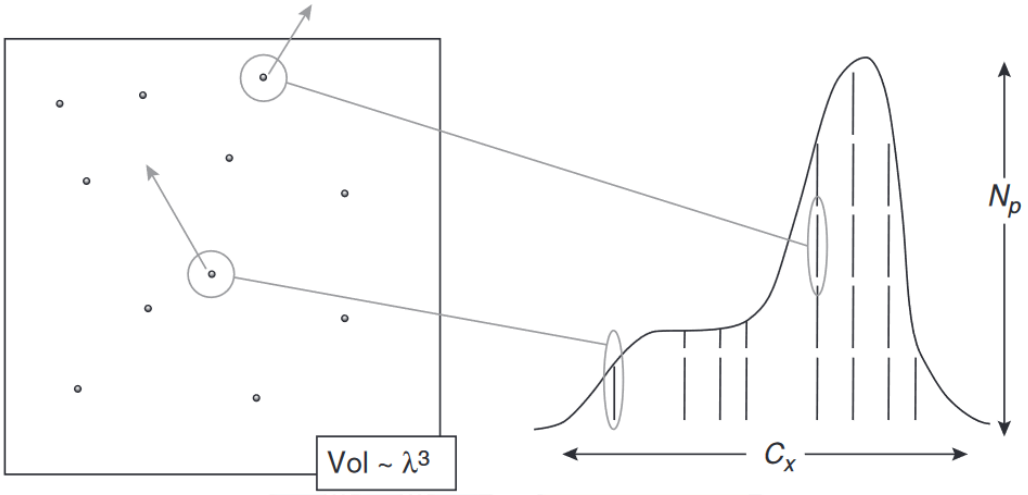

Figure 2.8: Schematic of a range of molecular velocities of a non–Maxwellian distribution represented by a reduced number of DSMC particles [100].

DSMC simulations require the discretization of physical space into a computational grid. Each cell provides a convenient reference for the sampling of the flow macroscopic properties and for the selection of potential collision pairs. In this fashion, if the volume shown in Figure 2.8 is regarded as a computational cell, the highlighted DSMC particles in Figure 2.8 represent an allowable collision pair despite their velocity vectors pointing away from each other. This is to be expected since each simulated particle represents a large number of identical real molecules of the same velocity sweeping through the volume, whose precise positions are spread throughout the volume.

To promote near-neighbor particle collisions and improve the accuracy of the method, the computational cells can be subdivided into an arbitrary number of sub-cells for the selection of collision pairs. As the number of possible collision pairs is a function of the number of particles in the cells, it is necessary to determine the optimum number of particles in each cell so that statistical accuracy can be achieved at a feasible computational cost [125, 126]. The same principle of computational efficiency applies to the size of the computational grid and the simulation time step [127]; since the accuracy of the DSMC method improves as these parameters are refined, but at the cost of a higher computational expenditure. Moreover, it has been demonstrated that, for a monatomic simple gas, the DSMC method provides a solution to the Boltzmann equation as the number of simulated particles approaches infinity and the time step and cell sizes approach zero [128].

2.2.1 Main DSMC algorithm

The basic DSMC algorithm uses an explicit time-stepping scheme in order to move particles in time and space within the computational domain. Figure 2.9 describes the basic algorithm that all DSMC solvers follow. First, after initializing the computational domain and boundary conditions, the mesh cells are populated with

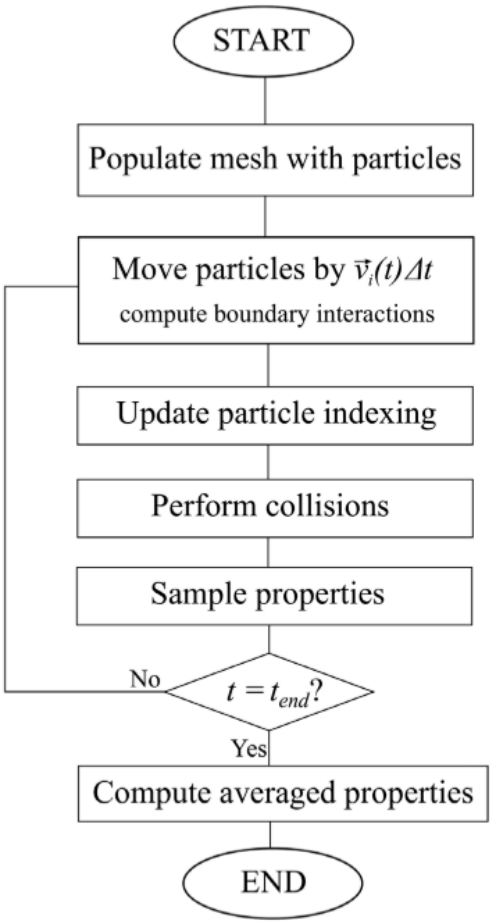

Figure 2.9: Flow chart of the basic DSMC time-integration scheme [95].

particles in thermodynamic equilibrium based on the freestream conditions. The flow develops from this initial state with time in a physically realistic manner, rather than by iterating from an initial approximation to the flow. Then, the individual steps during a single time step iteration are described as follows:

1. Move all particles in straight lines along their molecular velocity vectors for a time step Δt less than the local mean collision time. The position of all particles in the system is updated. Boundary conditions interactions for particles that collide with a surface are calculated. Particles that exit the simulation domain are removed.
2. The list of particles in each computational cell is updated to prepare for the collision routine.
3. Intermolecular collisions are performed stochastically within each cell.
4. The particle properties that are required to calculate macroscopic values are sampled in each cell.
5. Return to step 1 and repeat the process again for the next time step iteration $t + \Delta t$ until the simulation end-time (t_{end}) has been reached.

In its mathematical form, the particle movement in the simulated physical domain during a time step iteration is given by:

$$\boldsymbol{r}(t+\Delta t) = \boldsymbol{r}(t) + \boldsymbol{c}(t)\Delta t = \boldsymbol{r}(t) + \Delta \boldsymbol{r}, \tag{2.62}$$

where $\boldsymbol{c}$ is the velocity of a particular class of simulated particles and is assumed to be a linear combination of the thermal velocity and stream velocity. Once the particles have a new defined location, their indexing is updated by cell location, so that all particles in the cells can be assessed through a cross-reference list. This is because the collision and sampling routines depend on information about the current occupancy of each cell. Collisions are then performed in a probabilistic manner, for which several different collision modeling schemes have been formulated and applied.

2.2.2 The No-Time-Counter algorithm

The No-Time-Counter (NTC) algorithm [129] has proven to be a very accurate and efficient algorithm for ensuring a collision rate consistent with analytical theory. The probability of collision (P_{coll}) between two simulated molecules over the time interval Δt in a computational cell of volume V_{C} is

$$P_{\text{coll}} = \frac{F_{\text{N}}\sigma_{\text{T}}c_{\text{r}}\Delta t}{V_{\text{C}}}, \tag{2.63}$$

where F_{N} is the ratio of DSMC molecules to real gas molecules. The average number of real molecules in the cell is nV_{C} and the average number of simulated molecules is $N = nV_{\text{C}}/F_{\text{N}}$, where n is the number density in the real gas.

The complete set of collisions could be calculated using Equation 2.63 to compute the probability of collision for all $N(N-1)/2$ possible pairs in the cell. However, this approach is inefficient. Instead, maximum efficiency is achieved if only a fraction of pairs are included, where the fraction is such that the maximum probability becomes unity, and the resultant probability is increased in proportion with this fraction. The fraction is given by

$$(P_{\text{coll}})_{\text{max}} = F_{\text{N}}\,(\sigma_{\text{T}}\text{c}_{\text{r}})_{\text{max}}\,\Delta t/V_{\text{C}}, \tag{2.64}$$

and the number of pair selections per time step is obtained by multiplying Equation 2.64 by the product of the instantaneous and averaged value of the number of particles N in the cell, that is,

$$N_{\text{coll}} = \frac{1}{2}\frac{N\overline{N}F_{\text{N}}\,(\sigma_{\text{T}}\text{c}_{\text{r}})_{\text{max}}\,\Delta t}{V_{\text{C}}}. \tag{2.65}$$

The collision pairs are then tested using the acceptance–rejection method, where a random number R_f is uniformly chosen in $[0, 1]$ and the collision is accepted if

$$\frac{\sigma_{\mathrm{T}} c_{\mathrm{r}}}{(\sigma_{\mathrm{T}} c_r)_{\max}} > R_f. \tag{2.66}$$

If the collision were to be rejected, a new pair is randomly chosen and the procedure is repeated. The value of the parameter $(\sigma_{\mathrm{T}} c_r)_{\max}$ should be updated during a binary collision if the product $\sigma_{\mathrm{T}} c_r$ were to be greater than the stored value of $(\sigma_{\mathrm{T}} c_r)_{\max}$. In summary, in the NTC method, Equation 2.65 defines the number of collision pairs that are selected from the cell at each time step, and the collision is computed when the condition described in Equation 2.66 is met.

Other collision methods based on the principle of the maximum collision rate per time step include the Time Counter (TC) [130], Null Collision (NC) [131, 132], and Majorant Collision Frequency (MCF) [133] schemes. Contrary to the NTC method, these collision algorithms use a time-interval of δt_i for each captured collision within a time-step interval of Δt for the DSMC procedure and the collision process continues until $\sum_i \delta t_i > \Delta t$ [134].

Models based on classic kinetic theory, such as TC and NTC, need around 10–20 particles per cell and usually suffer from repeated collisions [134]. To address this problem, other methods based on the definition of a collision probability function for each particle pair, checking all pair combinations for collision occurrence, were introduced. Particularly, the MCF scheme has the advantage of reproducing the exact Poisson distribution of collision time as well as the mean collision time with a reduced sample size [135], since it has been shown to require fewer total particle number and an independence from the particle number in the cell [136, 137]. Another method based on the definition of collision probability function is the Simplified Bernoulli Trials (SBT) scheme [138, 139], which has a linear dependency of the computational cost on the particle number in cells and a higher computational efficiency.

2.2.3 Variable Hard Sphere

As described in subsection 2.1.4, in binary elastic collisions, all directions are equally possible for the post-collision velocity in a reference frame based on the center of mass. The most widely used DSMC collision cross-section model for elastic collisions is the Variable Hard Sphere (VHS) model. The VHS model is based on the Hard Sphere (HS) model, described in subsection 2.1.1, and shares some of the same principles but incorporates an explicit dependence between the total cross-section and the relative speed of colliding molecules [140]. The variable diameter employed in the VHS model is defined such that

$$d = d_{\mathrm{ref}} \left(\frac{(c_r)_{\mathrm{ref}}}{c_r} \right)^{-\omega}, \tag{2.67}$$

and, therefore, the collision cross-section diameter can be expressed as

$$\sigma_{\mathrm{T}}^{\mathrm{VHS}} = \sigma_{\mathrm{ref}} \left(\frac{(c_r)_{\mathrm{ref}}}{c_r} \right)^{-2\omega}, \tag{2.68}$$

where the exponent ω and the reference values d_{ref} and $c_{r,\mathrm{ref}}$ can be set to better emulate the behavior of real molecules during intermolecular collisions. Furthermore, it can be shown that the dynamic viscosity coefficient (μ) and the gas temperature are related by

$$\mu \propto T^{\omega}. \tag{2.69}$$

Thus, for a gas in equilibrium, the viscosity coefficient can be calculated as

$$\mu^{VHS} = \mu_{\mathrm{ref}}^{VHS} \left(\frac{T}{T_{\mathrm{ref}}} \right)^{\omega}, \tag{2.70}$$

where

$$\mu_{\mathrm{ref}}^{VHS} = \frac{15\sqrt{2\pi m_r k_b T_{\mathrm{ref}}}}{2(5-2\omega)(7-2\omega)\pi d_{\mathrm{ref}}^2} \tag{2.71}$$

For VHS molecules, the mean collision rate per molecule in an equilibrium gas can be expressed as

$$\nu = 4 d_{\mathrm{ref}}^2 n \left(\frac{\pi k_b T_{\mathrm{ref}}}{m} \right)^{1/2} \left(\frac{T}{T_{\mathrm{ref}}} \right)^{1-\omega}, \tag{2.72}$$

and the equilibrium mean free path may be written as

$$\lambda = \left(\sqrt{2}\pi d_{\mathrm{ref}}^2 n \left(\frac{T_{\mathrm{ref}}}{T} \right)^{\omega-1/2} \right)^{-1}. \tag{2.73}$$

An alternative for Equation 2.73 can be formulated based on the macroscopic flow properties [141] such that

$$\lambda = \frac{2(5-2\omega)(7-2\omega)}{15} \left(\frac{m}{2\pi k T} \right)^{1/2} \left(\frac{\mu}{\rho} \right). \tag{2.74}$$

The values of the reference and molecular parameters for the most common gas species are available in the related technical literature [91, 100].

2.2.4 Internal energy exchange

In the case of diatomic or polyatomic molecules, inelastic collisions must be considered to account for the energy exchange between the translational and internal energy modes. The most common method for the exchange between energy modes in DSMC simulations is the phenomenological Larsen–Borgnakke model [142]. In this model, the relaxation rate of internal energy modes is controlled by considering only a fraction Λ of collisions as inelastic collisions, while the rest of collisions $1-\Lambda$ are considered to be inelastic. The fraction Λ can be interpreted as the average probability (φ) of energy exchange between a particular mode of internal energy and the translational energy, i.e., $\Lambda \equiv \varphi$. The relaxation time (τ_{rel}) is defined as the time it takes for a disturbance to the equilibrium state to decay. It depends on the local flow properties and may be related to the relaxation collision number Z such that

$$Z = \frac{\tau_{rel}}{\tau_c}. \tag{2.75}$$

The collision number represents the average number of molecular collisions that are required for a particular mode to reach equilibrium. In doing so, the average probability φ can be defined as

$$\varphi = \frac{1}{Z} \tag{2.76}$$

In the case of rotational relaxation, DSMC simulations usually employ a fixed relaxation collision number Z_{rot}, and thus a constant relaxation probability φ_{rot}. When a collision is to take place, rotational relaxation is first tested using the acceptance-rejection method, and is accepted if

$$\frac{1}{Z_{\text{rot}}} > R_f, \tag{2.77}$$

where R_f is a random number from a uniform distribution between 0 and 1. If a collision is regarded as inelastic, the particle is assigned a new rotational energy following the conservation of energy principle. The total collision energy (E_{coll}) is reassigned between the translational and internal modes by sampling from the equilibrium distributions of these modes that are appropriate for this total energy. The acceptance-rejection method is used to define the post-collision translational energy (E^*_{tr}) and post-collision internal energy (E^*_{int}), while decreasing the total translational energy accordingly. The post-collision relative speed (c^*_r) in the center-of-mass frame of reference can be calculated as

$$c^*_r = 2\sqrt{\frac{E^*_{\text{tr}}}{m_r}}, \tag{2.78}$$

and a new direction for this speed may be chosen at random.

In contrast to the rotational energy mode, the vibrational energy levels are widely spaced and vibration can rarely be regarded as being fully excited. Thus, the Larsen-Borgnakke method can be applied to the vibrational modes through a quantum approach that assigns a discrete vibrational level to each molecule. For vibrational energy transfer, this model contains an implicit temperature T_{coll} based on the total collision energy E_{coll} that is being redistributed. This temperature can be written as

$$T_{\text{coll}} = \frac{i_{\max}\Theta_{\text{vib}}}{\frac{7}{2} - \omega}, \tag{2.79}$$

where Θ_{vib} is the characteristic vibrational temperature of the gas specie and ω the temperature exponent of viscosity. The quantum versions of the Larsen-Borgnakke method restrict the values of the vibrational energy of a molecule to those that correspond to the discrete quantum levels of an equally spaced harmonic oscillator. In Equation 2.79, $i_{\max}$ is the maximum quantum level available to the particles and can be defined as

$$i_{\max} = \left\lfloor \frac{E_{\text{coll}}}{k_b\Theta_{\text{vib}}} \right\rfloor, \tag{2.80}$$

where the operation $\lfloor \ldots \rfloor$ denotes truncation. Equation 2.79 can be used to calculate the vibrational collision number (Z_{vib}) such that

$$Z_{\text{vib}} = \left(\frac{\Theta_d}{T_{\text{coll}}}\right)^{\omega} \left[Z_{\text{ref}}\left(\frac{\Theta_d}{T_{\text{ref}}}\right)^{-\omega}\right] \exp\left[\left(\sqrt[3]{\frac{\Theta_d}{T_{\text{coll}}}} - 1\right) / \left(\sqrt[3]{\frac{\Theta_d}{T_{\text{ref}}}} - 1\right)\right], \tag{2.81}$$

where Θ_d is the characteristic dissociation temperature and Z_{ref} is the vibrational collision number at a reference temperature and T_{ref}, which is usually set to the characteristic vibrational temperature [143]. In DSMC simulations, vibrational relaxation is tested before rotational and translational energy exchanges. The vibrational collision number Z_{vib} is used in combination with the acceptance-rejection method to test for vibrational energy exchange, which is accepted if

$$\frac{1}{Z_{\text{vib}}} > R_f, \tag{2.82}$$

where R_f is a random number between 0 and 1. The post-collision vibrational quantum level i^* is chosen uniformly between 0 and the maximum possible level $i^*_{\max}$ and is then accepted through an acceptance-rejection based on the probability ratio

$$\frac{P}{P_{\max}} = \left(1 - \frac{i^* k_b\Theta_{\text{vib}}}{E_{\text{c}}}\right)^{3/2-\omega_{pq}} \tag{2.83}$$

where ω_{pq} is the average viscosity exponent of the collision pair p and q. If accepted, the total energy of the colliding pair is reduced accordingly before proceeding to the rotational and translational energy exchange procedure.

An alternative physical based method called *energy sink* was used [144, 145, 146] as an alternative to the phenomenological Larsen-Borgnakke method. However, it was not widely adopted for internal energy exchange modeling since it didn't satisfy the principle of detailed balance and led to distortions of the equilibrium distribution function [101].

The most widely used chemistry model for DSMC simulations of rarefied hypersonic reacting flows is the Total Collision Energy (TCE) Model [91]. However, the restrictions phenomenological TCE model prompted the development of the Quantum-Kinetic (QK) [147] physical model for dissociation and recombination reactions. The QK chemistry model links chemical reaction and cross sections to the energy exchange process and the probability of transition between vibrational energy states, avoiding the requirement of experimental data. Chemical reactions and molecule dissociation are outside the scope of this investigation, but further information on DSMC chemical models can be found in the available technical literature [91, 100, 147, 148].

2.2.5 Gas-surface Interactions

Particles may collide with solid boundaries as they move through the simulated domain, requiring the computation of the interaction between the colliding particles and the surface. In DSMC simulations, the primary models employed to handle gas-surface interactions are specular reflection and diffuse reflection.

In the case of specular reflection, shown in Figure 2.10a, the molecular velocity component normal to the surface is reversed, while the parallel component of the velocity remains unchanged. This model assumes perfectly elastic collisions with no exchange of momentum. From a physical standpoint, it represents a perfectly smooth surface and is functionally identical to a plane of symmetry.

In contrast, the diffuse reflection model emulates a rough surface on the microscopic scale, and thus is more realistic and appropriate for practical applications. In diffuse reflection, the microscopic state of each molecule after reflection is independent of its previous microscopic state before colliding with the surface, as the post-interaction velocity is not calculated from the pre-interaction velocity. Instead, the velocities of the reflected molecules are distributed in accordance with the Maxwellian distribution for molecules in thermal equilibrium with the local surface temperature. The Maxwellian distribution functions for the perpendicular ($f_\perp$) and parallel ($f_\parallel$) velocity components are

$$f_\perp = \frac{m}{k_b T_{wall}} c_\perp \exp\left(\frac{-mc_\perp^2}{2k_b T_{wall}}\right), \tag{2.84}$$

and

$$f_{\parallel} = \sqrt{\frac{m}{2\pi k_b T_{wall}}} \exp\left(\frac{-mc_{\parallel}^2}{2k_b T_{wall}}\right), \tag{2.85}$$

respectively. The post-interaction velocity components, perpendicular ($c_{\perp}$) and parallel ($c_{\parallel}$) to the surface, can be sampled from these distributions so that

$$c_{\perp} = \sqrt{-\frac{2k_b T_{wall}}{m} \ln(R_f)}, \tag{2.86}$$

and

$$c_{\parallel} = \sqrt{\frac{k_b T_{wall}}{m}} R_f, \tag{2.87}$$

where R_f is a uniformly distributed random number between 0 and 1. As shown in Figure 2.10b, in this model particles have equal probability of reflection in any direction. In the case of a moving boundary, the velocity of the surface could be added directly to Equation 2.86 and Equation 2.87 to obtain the instantaneous particle velocity.

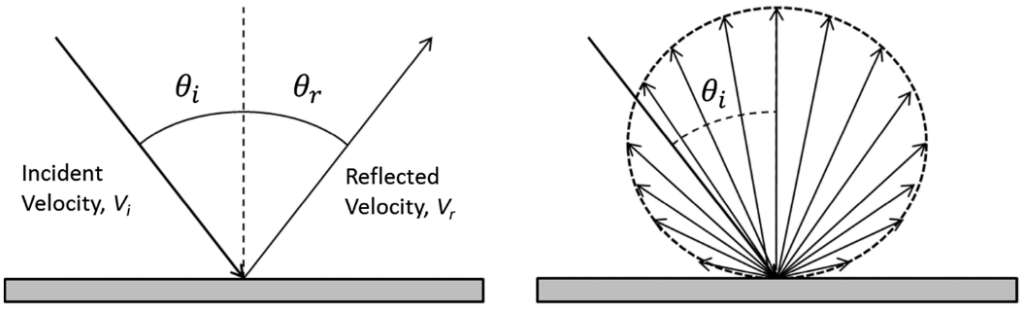

(a) Specular reflection **(b)** Diffuse reflection

Figure 2.10: Comparison of specular and diffuse reflected angular distributions [149].

3 | Validation and Verification

The DSMC method is the standard tool for the computational simulation of rarefied high-speed flows [95]. However, the DSMC method, and the dsmcFoam+ code in particular, have not been thoroughly tested for applications involving IAD reentry devices designed for CubeSats or secondary payloads. This chapter aims to demonstrate the reliability and accuracy of the dsmcFoam+ code, while endorsing its application in investigations concerning high-speed reentry flow and rarefied flow physics in small-sized IAD vehicles. To achieve this objective, a Validation and Verification (V&V) process is conducted. The V&V approach adopted in this study follows the framework proposed by the American Institute of Aeronautics and Astronautics (AIAA) [150], which provides the following definitions:

- **Validation:** The process of determining the degree to which a model is an accurate representation of the real world from the perspective of the intended use of the model.
- **Verification:** The process of determining whether a model implementation accurately represents the developer's conceptual description of the model and the solution to the model.

In this way, the V&V process performed will help to assess the accuracy and resilience of the dsmcFoam+ code under conditions similar to the simulations of the IAD concept designs under study. Both the validation and verification processes are based on previous computational work carried out by Moss *et al.*. Two main test cases were considered:

Case A (Orion): Hypersonic flow over the Orion crew module [151].

Case B (IRVE): Low-density aerodynamics of the IRVE reentry vehicle [152].

For the validation process, in each test case, the results obtained from the dsmcFoam+ solver are directly compared to the results presented by Moss *et al.* [151, 152]. Moreover, for the IRVE simulations, additional continuum-based computational fluid dynamic computations were performed by researchers from the University of Naples Federico II at the lowest altitude in analysis. For the verification process, the computational parameters considered to test the accuracy of the DSMC method [91] were: spatial discretization, time discretization, particle number assessment, and sampling effects.

3.1 Simulation description

3.1.1 Case A: Orion hypersonic reentry

The first V&V case to be analyzed is that of non-reacting hypersonic flow over the Orion crew module, previously investigated by Moss *et al.* [151]. The capsule geometry is confronted with a flow at 0° angle of attack and in conditions similar to those that could be experienced by the spacecraft during the first stages of atmospheric reentry. The complete description of the simulated geometry utilized by Moss *et al.* [151], including the exact location of relevant points of interest, is presented in Fig. 3.1. The geometry of the Orion crew module is assumed to be axisymmetric.

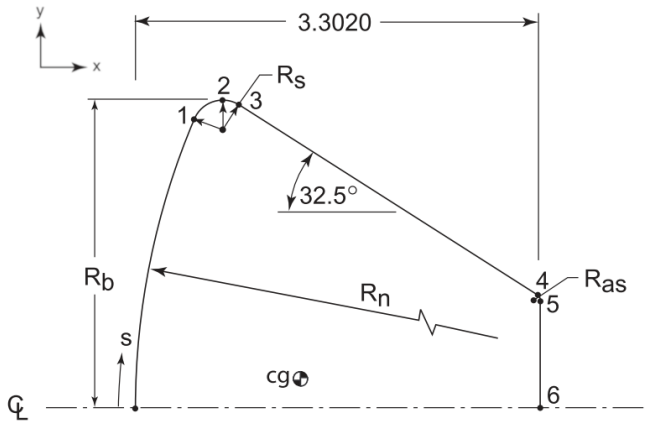

Location	x	y	s
1	0.4812	2.3615	2.4264
2	0.7126	2.5146	2.7203
3	0.8477	2.4752	2.8630
4	3.2785	0.9266	5.7451
5	3.3020	0.8838	5.7961
6	3.3020	0.0000	6.6799
cg	1.3333	0.2414	-

D_b = 5.0292 R_s = 0.2515
R_b = 2.5146 R_{as} = 0.0508
R_n = 6.0350

Figure 3.1: Orion crew module geometry description, all dimensions in meters. D_b: maximum body diameter, R_b: maximum body radius, R_n: blunt forebody spherical nose, R_s: shoulder radius, R_{as}: afterbody shoulder radius [151].

The freestream conditions and atmospheric composition at 105 km of altitude are the same as those used by Moss *et al.*; and are described in Table 3.1 and Table 3.2, respectively. A constant wall temperature (T_{wall}) of 760 K is assumed on the surface of the Orion capsule [151]. Based on the maximum body diameter (D_b) and the freestream mean free path (λ_∞), the Knudsen number (Kn) is calculated to be 0.0668. Therefore, the simulation case can be classified as in transitional regime. Taking into account the freestream conditions shown in Tab. 3.1, the Mach number (Ma) is calculated to be 25.6, well above the Ma > 5 criterion for identifying possible hypersonic phenomena [98].

The size of the computational domain was defined to be large enough so that there was no interference of the domain boundaries with the shock wave structure or the development of the flow around the spacecraft. On this basis, the flow inlet is placed 4 m upstream of the capsule, and the flow outlet was placed 6.5 m downstream of the stagnation point in front of the capsule. Following the same principle, the extension of the computational domain is set 4 m from the centerline in the z and y directions. The defined computational domain is reduced to a quarter-section of its original size, taking advantage of the axisymmetric quality of the vehicle. The simulation of a quarter-section is favored over fully axisymmetric since the latter may

Table 3.1: Freestream conditions [151].

Parameter	Value	Units
Altitude (H)	105	km
Flow speed (U_∞)	7600	m/s
Temperature (T_∞)	211	K
Pressure (P_∞)	0.0145	N/m^2
Density (ρ_∞)	2.30×10^{-7}	kg/m^3
Number density (n_∞)	4.98×10^{18}	m^{-3}
Mean free path (λ_∞)	3.36×10^{-1}	m

Table 3.2: Atmospheric composition at 105 km of altitude [151].

Gas species	n (m^{-3})	X
N_2	3.89×10^{18}	0.782
O_2	7.60×10^{17}	0.153
O	3.25×10^{17}	0.065

result in an overestimation of macroscopic properties near the stagnation line. Then, it is further reduced by removing volume from zones further away from the spacecraft. The resulting computational domain and the different types of boundary conditions used in each domain boundary are shown in Figure 3.2a. Their denomination can be described as follows: The sides marked (I) represent the flow inlets, where particles enter the computational domain with the corresponding freestream properties. The flow outlet is marked as (II), where a vacuum condition is imposed and all particles colliding with this surface are removed from the computational domain. This condition is appropriate due to the high flow velocity, which makes the probability that particles move against the flow in this area negligible [91]. Planes marked (III) account for the reduction of the computational volume to a quarter of its original size, where a specular reflection model is used for all colliding particles. Finally, the walls of the Orion reentry capsule are marked as (VI), where a diffusive wall boundary condition with full thermal and momentum accommodation is imposed.

The mesh refinement is calculated so that the cell size is equal or smaller than $1/4$ of the freestream mean free path at 105 km altitude. Cell size was further refined near the surface of the capsule and near the stagnation line region. Thus, the total number of cells used for the simulation was 9.35×10^5. The largest cell had a volume of $9.13 \times 10^{-4}\ m^3$. Calculating the average cell edge as the cubic root of its volume, the average cell edge is almost 3.5 times smaller than the freestream mean free path. Therefore, the resulting mesh can be considered in compliance with the good practices established for the method [91]. A representative mesh for 105 km of altitude is shown in Fig. 3.2b. The time step (Δt) is calculated as a fraction of the residence time (Δt_{res}) of simulated molecules in each cell. The residence time refers to the time a simulated particle spends in a particular cell and can be defined as

$$\Delta t_{\text{res}} = \frac{\overline{s_{\text{cell}}}}{c_p}, \tag{3.1}$$

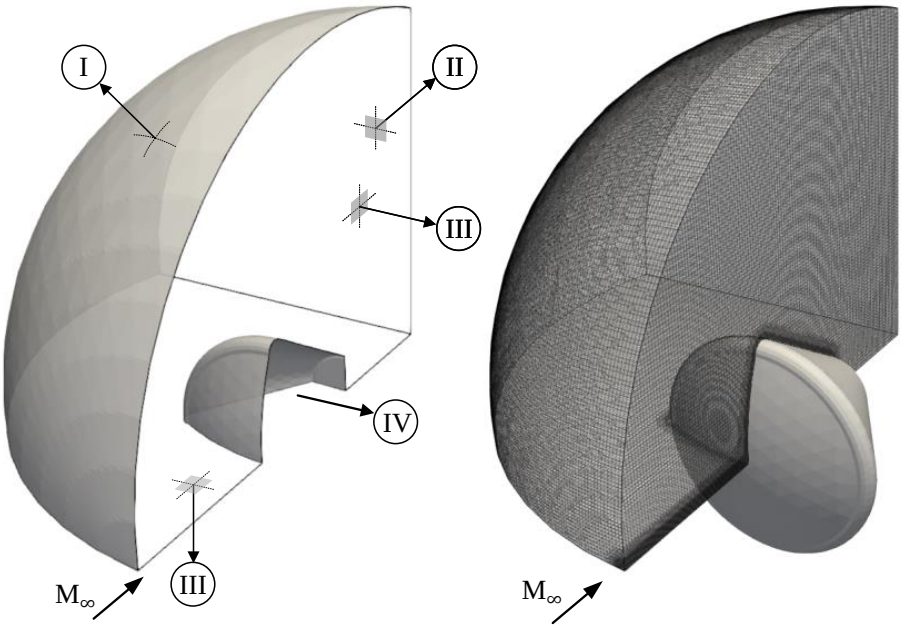

(a) Boundary denomination. **(b)** Computational mesh.

Figure 3.2: Orion capsule simulation setup. (a) Computational domain and boundary denomination. (b) Representative computational mesh for 105 km.

where the speed of DSMC particles (c_p) is calculated as the sum of the freestream flow speed and the most probable velocity of the particles, that is,

$$c_p = U_\infty + \sqrt{\frac{2T_\infty k_b}{m}}. \tag{3.2}$$

A time step of 2.5×10^{-6} is used for the simulation of the Orion crew module, equivalent to $1/3$ of the residence time. This time step is more than 60 times smaller than the τ_c of 1.6×10^{-4} exhibited by particles under these conditions. Concerning simulated particles, the number of DSMC particles to be employed in a given simulation setup can be defined in proportion to the number density of real molecules in the flow, that is,

$$N_{equiv} = \frac{n_\infty \cdot (\text{System Volume})}{(\text{No. cells}) \cdot (\text{Particles per cell})}. \tag{3.3}$$

For the simulation of the Orion reentry capsule, the mesh is initialized with a total of 1.40×10^7 particles, corresponding to an average of 15 simulated particles for each cell, with an equivalence ratio (N_{equiv}) of 1.40×10^{14} real molecules per simulated particle. In addition to being an excellent validation case for dsmcFoam+, this case and the simulation setup described in this section are used as a reference test case for the computational verification of the dsmcFoam+ solver in section 3.3.

3.1.2 Case B: IRVE low-density aerothermodynamics

A second validation and verification case study is carried out based on the numerical investigations by Moss *et al.* on the low-density high-speed aerothermodynamics of the IRVE reentry vehicle. Code validation simulations are performed considering an angle of attack of 0° and 5 altitudes of reentry (H), from 110 to 95 km. Continuum CFD simulations of the IRVE vehicle at 95 km of altitude were carried out by researchers from the University of Naples Federico II to further complement the validation process. The code verification process was carried out taking into account an altitude of 105 km as the standard test case. A complete description of the IRVE geometry model used for all V&V simulations is presented in Fig. 3.3 [152, 44]. The spacecraft geometry is assumed to be axisymmetric.

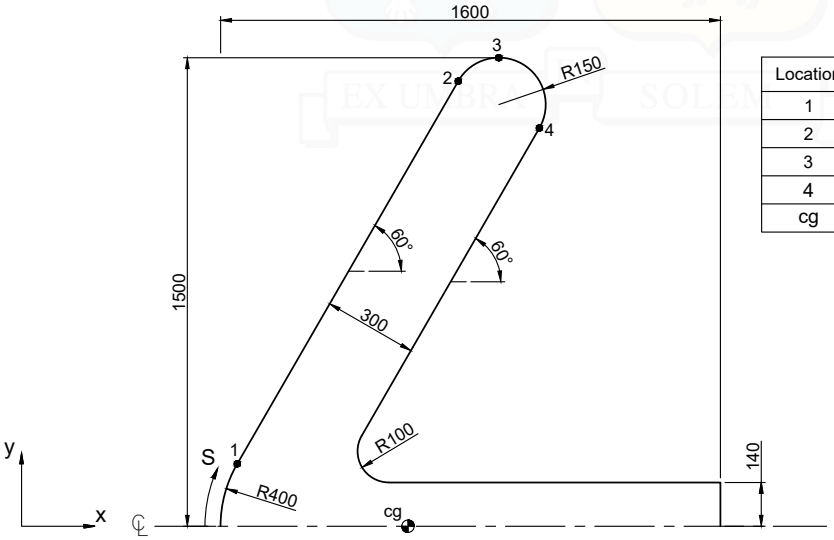

Location	x	y	s
1	53.59	200.00	209.44
2	760.84	1425.00	1623.95
3	890.75	1500.00	1781.03
4	1020.65	1275.00	2095.19
cg	601.98	0.00	-

Figure 3.3: IRVE profile geometry description, all dimensions in millimeters [152, 44].

The freestream flow properties and the atmospheric composition for each simulated altitude are presented in Table 3.3 and Table 3.4, respectively. In Table 3.3, the Knudsen number is calculated based on the maximum cross-section diameter of the IRVE spacecraft. In all IRVE simulations, a wall temperature (T_{wall}) of 300 K was used [152] and gas-surface interactions were assumed to be diffuse, with full energy accommodation.

For the DSMC computations, the size of the computational domain is defined large enough so that its boundaries do not interfere with the shock wave structure. Similarly to the procedure described in subsection 3.1.1, the full computational domain is reduced to a quarter-section of its original size, taking advantage of the axisymmetric quality of the geometry of the IRVE spacecraft. As depicted in Fig. 3.4a, four distinct boundary conditions are used. Surfaces marked (I) represent flow inlets, where particles enter the computational domain with the corresponding freestream properties; surfaces marked as (II) represent flow outlets, where colliding particles are deleted from the computational domain; sides marked as (III) are planes of symmetry, where specular collisions are imposed; and the surface of the spacecraft is marked as

Table 3.3: Freestream properties, Knudsen number (Kn) and Mach number (Ma) for all simulated altitudes [152].

Parameter	H = 110 km	H = 105 km	H = 100 km	H = 95 km	Units
U_∞	1075	1122	1159	1205	m/s
T_∞	243	208	196	188	K
P_∞	6.85×10^{-3}	1.46×10^{-2}	2.99×10^{-2}	8.09×10^{-2}	N/m^2
ρ_∞	9.23×10^{-8}	2.36×10^{-7}	5.18×10^{-7}	1.48×10^{-6}	kg/m^3
n_∞	2.04×10^{18}	5.09×10^{18}	1.10×10^{19}	3.12×10^{19}	m^{-3}
λ_∞	7.88×10^{-1}	3.36×10^{-1}	1.42×10^{-1}	5.79×10^{-2}	m
Kn	0.2627	0.1120	0.0473	0.0193	–
Ma	3.3	3.8	4.1	4.4	–

Table 3.4: Number density (n) and molar fraction (X) of gas species for all simulated altitudes [152].

H (km)	N_2		O_2		O	
	n (m^{-3})	X	n (m^{-3})	X	n (m^{-3})	X
110	1.573×10^{18}	0.770	3.990×10^{18}	0.783	8.661×10^{18}	0.784
105	2.516×10^{17}	0.123	8.054×10^{17}	0.158	1.952×10^{18}	0.177
100	2.171×10^{17}	0.106	2.992×10^{17}	0.059	4.281×10^{17}	0.039
95	2.171×10^{17}	0.106	2.992×10^{17}	0.059	4.281×10^{17}	0.039

(IV), where a diffuse reflection with full thermal accommodation is specified. The mesh refinement is defined so that the cell edge size is a fraction of the freestream mean free path of each corresponding altitude. An example of the computational mesh used for an altitude of H = 110 km is presented in Fig. 3.4b.

In DSMC simulations, the computational requirements become prohibitively expensive as altitude decreases, due to the higher atmospheric density at lower altitudes. Thus, the computational domain size and mesh refinement are adjusted accordingly. In Table 3.5, several computational parameters are presented as functions of the altitude of reentry. The calculation of these parameters follows the same procedure described in subsection 3.1.1. Figure 3.5 shows the computational mesh employed for the simulation of the IRVE spacecraft at H = 95 km.

Table 3.5: Volume of the computational domain, number of cells, number of initialised particles (N_{initial}), average number of particles in steady state ($\overline{N}_{\text{steady}}$), time step ($\Delta t$) based on simulation altitude

H (km)	Vol. (m^3)	No. cells	N_{initial}	$\overline{N}_{\text{steady}}$	Δt (s)
110	76.643	2.62×10^4	3.93×10^5	4.59×10^5	2.00×10^{-5}
105	76.643	2.18×10^5	2.17×10^6	2.56×10^6	1.50×10^{-5}
100	47.034	2.46×10^5	2.46×10^6	3.12×10^6	1.25×10^{-5}
95	41.724	2.56×10^5	2.56×10^6	3.31×10^6	5.00×10^{-6}

CFD simulations are performed using a commercial Navier-Stokes solver, ANSYS-FLUENT, with a trimmed grid that matches the degree of thickness of the DSMC mesh at the corresponding altitude. Similar boundary conditions to those employed in the DSMC simulations are used for the CFD computations, with identical freestream conditions as described in Table 3.3 and Table 3.4. The inlet and external domains are

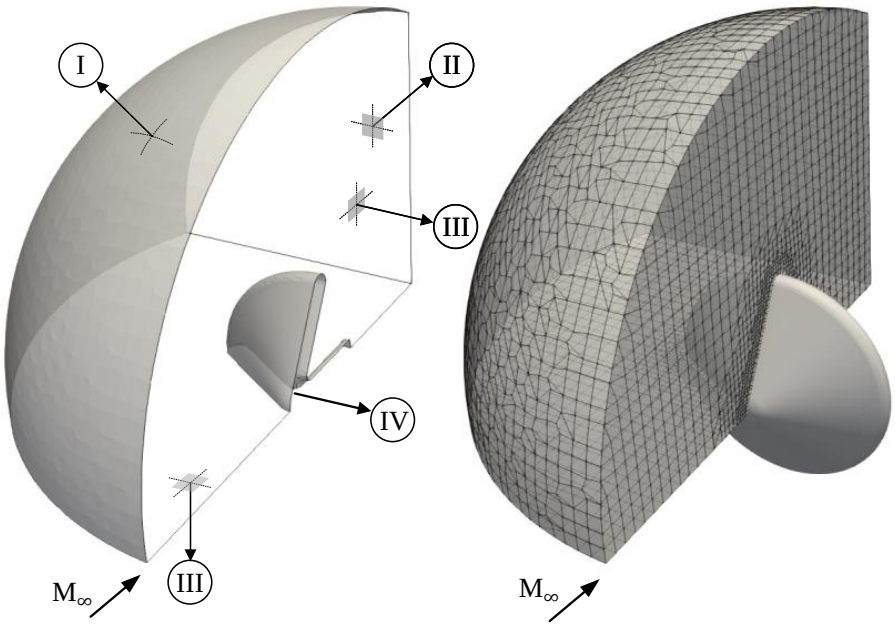

(a) Boundary denomination. **(b)** Computational mesh.

Figure 3.4: IRVE simulation setup. (a) Computational domain and boundary denomination. (b) Representative computational mesh for H = 110 km.

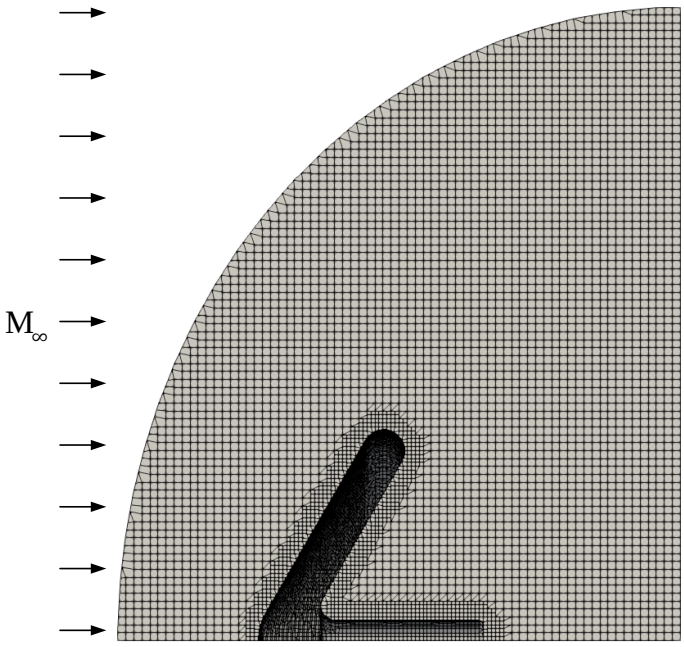

Figure 3.5: Computational mesh employed for IRVE simulations at H = 95 km.

modeled as pressure far-fields, enforcing the values of velocity, pressure, and temperature equivalent to those found at 95 km of altitude. The simulation assumes non-reacting flow, with a constant wall temperature of 300 K, consistent with the conditions described by Moss *et al.* [152] and employed in the DSMC simulations.

3.2 dsmcFoam+ code validation

3.2.1 Case A: Orion hypersonic reentry

The simulation of the Orion crew module was run until approximately 0.6 seconds of simulation time, or close to 2.4×10^5 time step iterations. The number of particles in the computational domain stabilized at 2.4×10^7 particles, upon which the problem can be said to have reached the steady state. The time average of the simulation data was initiated at 0.015 s of simulation time, over 6.0×10^4 time-step iterations after achieving steady state, ensuring that the number of particles and the average linear kinetic energy of the system had stabilized.

In Table 3.6, the aerodynamic coefficients calculated with the dsmcFoam+ code are directly compared to the results presented by Moss *et al.* [151] for the reentry of the Orion capsule. The moment coefficient about the center of gravity ($C_{m,cg}$) is defined by

$$C_{m,cg} = \frac{M_{cg}}{\frac{1}{2}\rho_\infty U_\infty^2 A_{\text{ref}} L_{\text{ref}}}, \tag{3.4}$$

and, for 0° angle of attack, the momentum about the center of gravity is calculated as

$$M_{cg} = F_A y_{cg} \equiv F_D y_{cg}, \tag{3.5}$$

where y_{cg} is the offset distance from the center line. From this table, it can be observed that the results match almost perfectly, with a maximum percentage difference of % 1.22 in relation to the momentum in the center of gravity.

In Figure 3.6, the surface heat transfer coefficient (C_h) along the nondimensional surface length (S/R_n) of the Orion crew module is presented. In this figure, the results calculated using the dsmcFoam+ code are compared with the results presented by Wilmoth *et al.* [153]. Wilmoth *et al.* [153] performed DSMC simulations of reacting flow over the Orion crew module employing the DS2V and DAC codes based on the work by Moss *et al.* [151]. In general, good agreement is found between the dsmcFoam+ results and the results presented by Wilmoth *et al.*. The slight offset in these results can be attributed to the effects of chemical reactions in the flow, where nonreactive models are known to slightly overestimate the strength and intensity of the shock wave [91, 98]. However, at 105 km of altitude, the effects of chemical reactions and the dissociation of molecules are not significant enough to cause a large deviation between the results obtained from reactive or nonreactive models.

Table 3.6: Relevant aerodynamic coefficients for the reentry of the Orion capsule at H = 105 km and AoA = 0°. [151].

Coeff.	dsmcFoam+	DS3V	% Diff.
C_D	1.696	1.709	0.76
$C_{m,cg}$	−0.081	−0.082	1.22

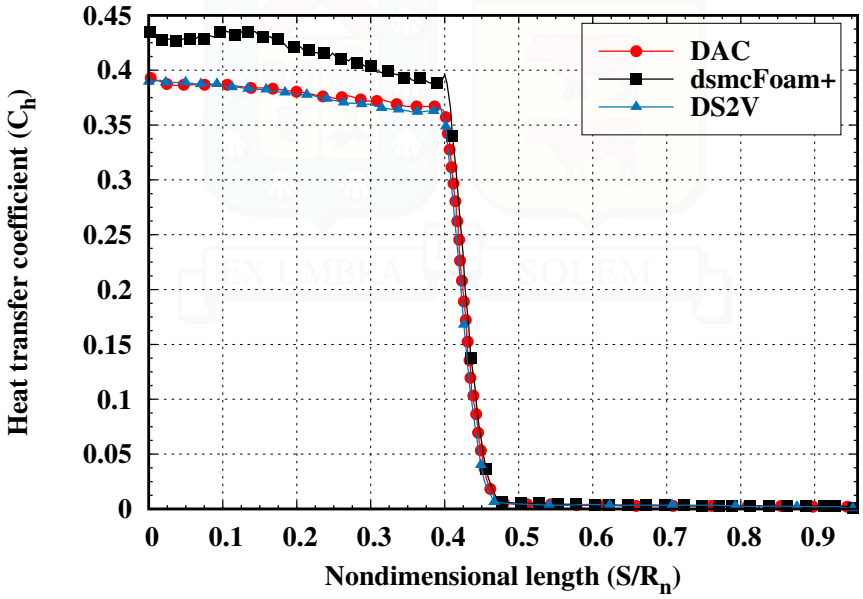

(a) Overall extension from center to afterbody shoulder.

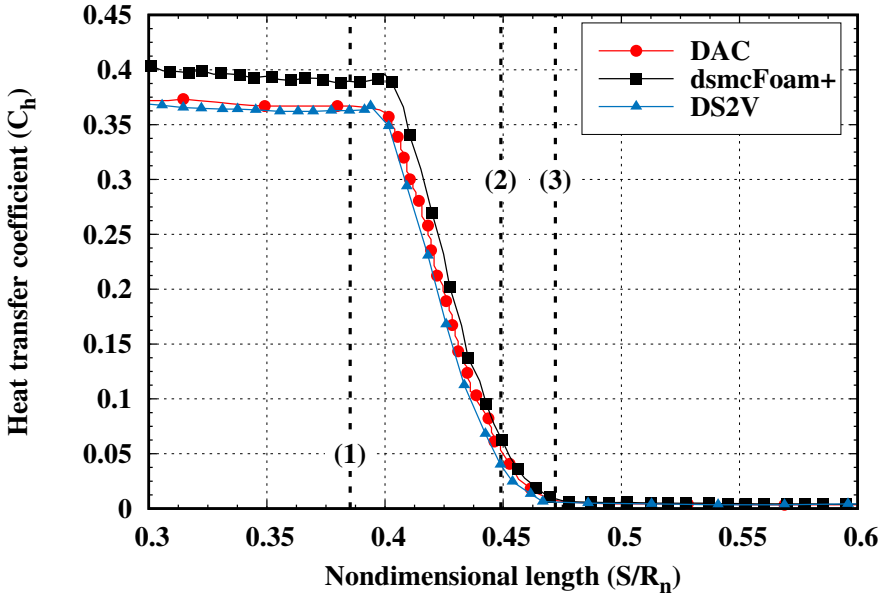

(b) Close up range near forebody shoulder section.

Figure 3.6: Surface heat transfer coefficient (C_h) comparison along Orion's dimensionless surface length (S/R_n) [151].

3.2.2 Case B: IRVE low-density aerothermodynamics

All DSMC simulations were run for over 1 second of simulation time, and the time averaging of the corresponding data fields was started once steady state had been reached. In Figure 3.7 the flow temperature and streamlines obtained from dsmcFoam+ at 110 km of altitude are compared to the results calculated by Moss *et al.* using the DS3V code [152]. Similarly, in Figure 3.8, the temperature field and streamlines calculated with dsmcfoam+ at an altitude of 95 km are visually compared with the results presented by Moss *et al.* using DS3V [152] and the results obtained from the CFD simulations.

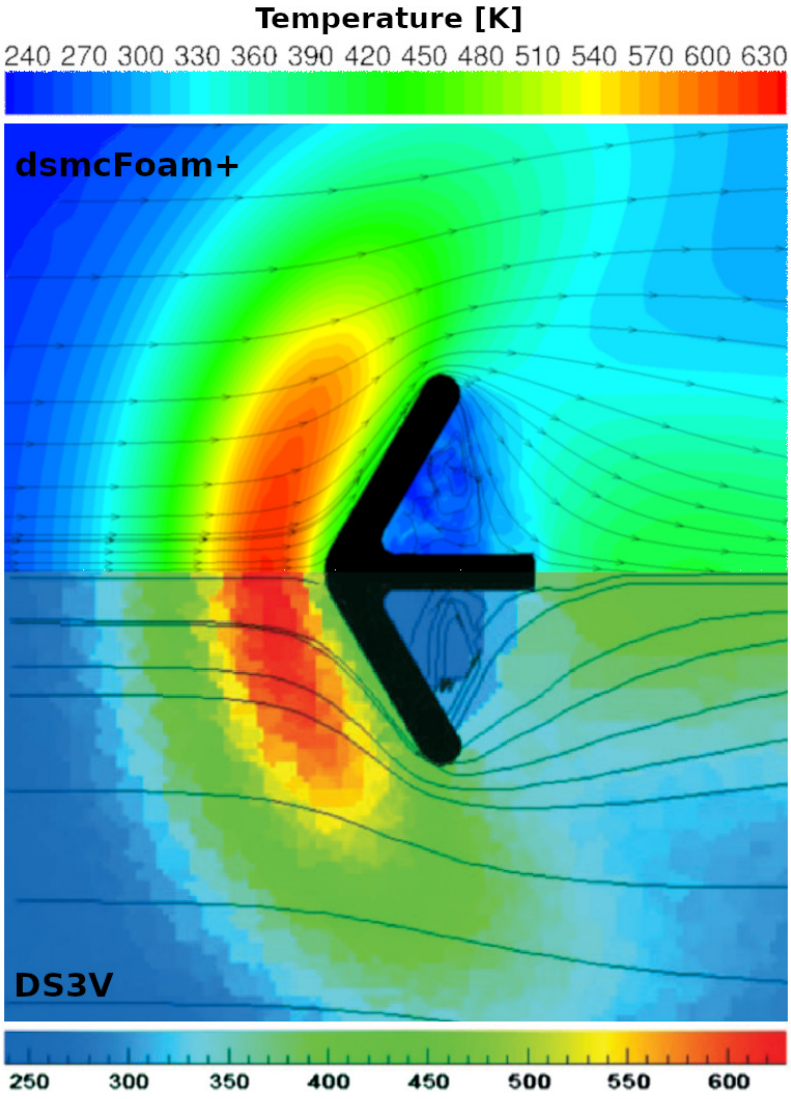

Figure 3.7: Computed temperature field and streamlines at H = 110 km. Top half: Results calculated with dsmcFoam+. Bottom half: Results presented by Moss *et al.* [152].

According to Fig. 3.7, H = 110 km, the formation of a diffuse shock wave is observed upstream of the IRVE geometry. The shock wave structure and the streamline paths are almost identical between the computed results by the dsmcFoam+ and DS3V codes. The region behind the thermal protection shield is

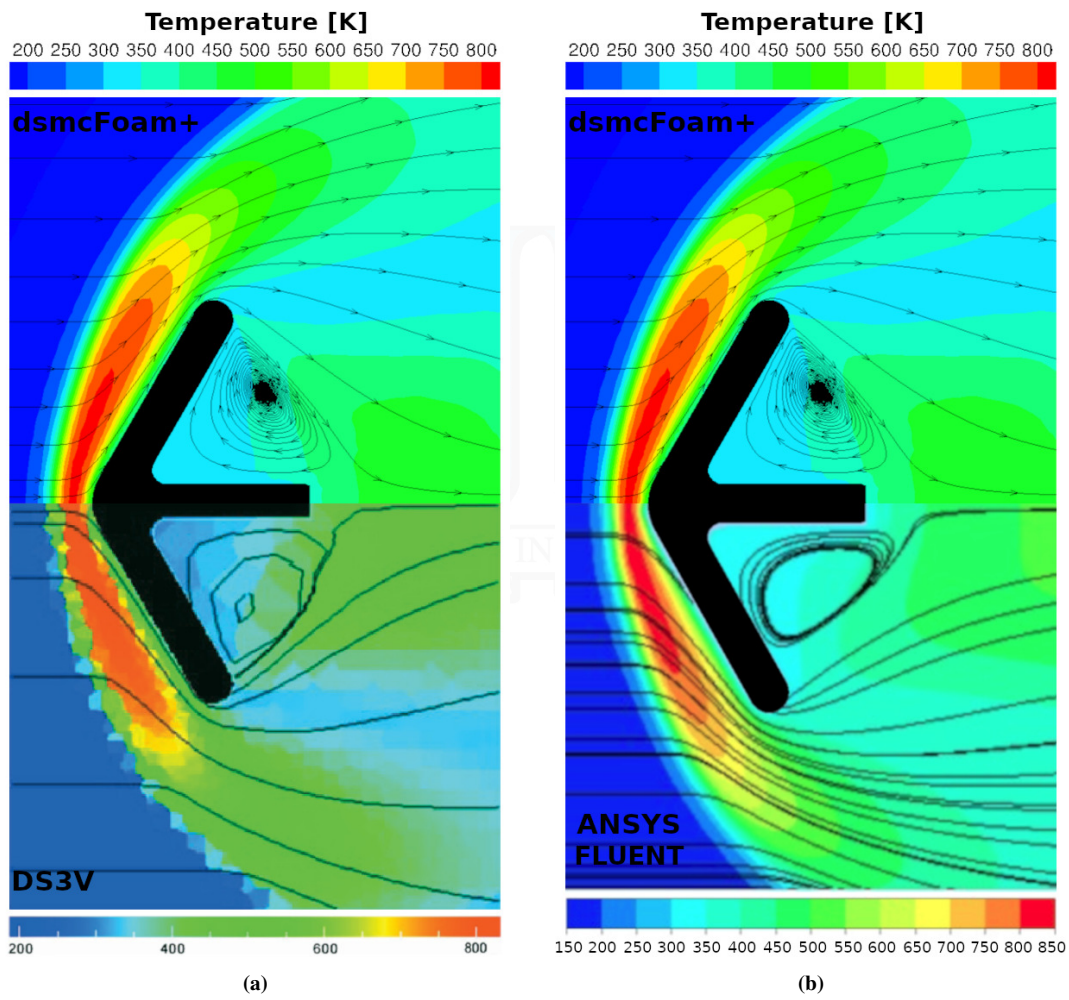

Figure 3.8: Computed temperature field and streamlines at H = 95 km. (a) Top: dsmcFoam+. Bottom: DS3V. (b) Top: dsmcFoam+. Bottom: ANSYS-FLUENT.

characterized by low particle velocity and the streamlines show the initial formation of a flow recirculation zone. This recirculation region is clearly formed for the 95 km altitude case, as shown in Fig. 3.8a and Fig. 3.8b. In addition, a good agreement can be distinguished between the temperature contour levels obtained by the dsmcFoam+ and those computed by DS3V and the continuum-based CFD solver, respectively. At 95 km altitude, a noticeable decrease in the shock wave thickness is observed along with a significant increase in the peak temperature.

Fig. 3.9 shows the heat transfer coefficient (C_h) for H = 95 km over the nondimensional vertical length of the spacecraft front surface (y/R_n). In this figure, a good agreement is observed between the dsmcFoam+ and the Langley Aerothermodynamic Upwind Relaxation Algorithm (LAURA) results. The LAURA code is a computational fluid dynamics simulation code based on the continuum Navier-Stokes equations developed by NASA [154, 152]. LAURA and ANSYS-FLUENT are capable of accounting for small degrees of non-equilibirum phenomena, such as temperature and velocity jumps. In this fashion,

Fig. 3.8b and Fig. 3.9 demonstrate a good agreement between discrete particle-based solvers, such as dsmcFoam+, and continuum-based solvers, such as ANSYS-FLUENT or LAURA.

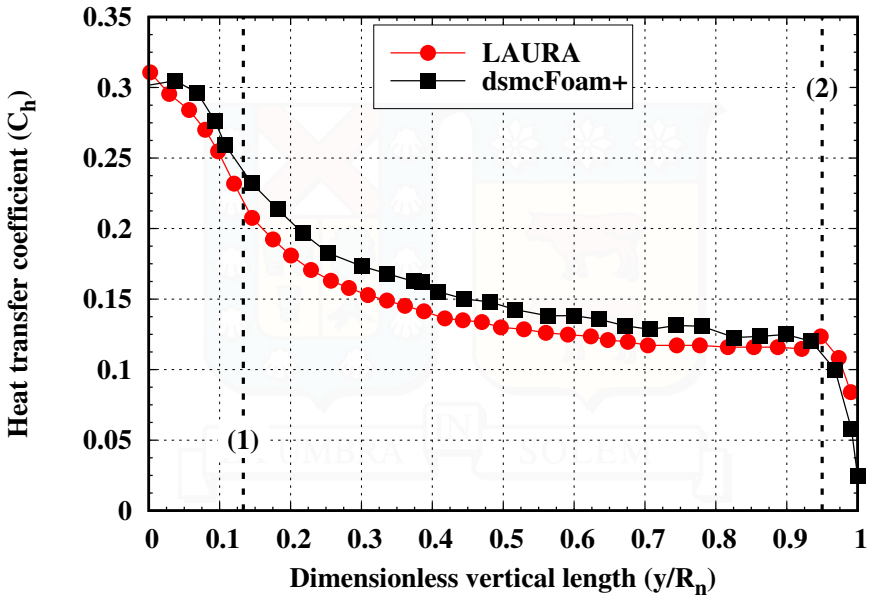

Figure 3.9: Heat transfer coefficient (C_h) over the nondimensional vertical length (y/R_n) for H = 95 km [152]. The surface coordinates (1) and (2) are specified in Figure 3.3.

Table 3.7 presents the drag coefficient (C_D) and stagnation point heat rate (q_0) obtained by the dsmcFoam+ and DS3V codes [152] from 110 to 95 km altitude. Once again, good agreement is observed between the results obtained by both codes, with a maximum percentage difference of 1.474% and 5.235 % for C_D and q_0, respectively.

Table 3.7: Drag coefficient (C_D) and stagnation point heat rate (q_0) comparison for all simulated altitudes using dsmcFoam+ and DS3V [152].

H (km)	dsmcFoam+		DS3V			
	C_D	q_0 (W/cm^2)	C_D	% Diff.	q_0 (W/cm^2)	% Diff.
110	1.856	0.0039	1.884	1.474 %	0.0041	5.000 %
105	1.644	0.0093	1.647	0.192 %	0.0098	5.235 %
100	1.544	0.0174	1.543	0.054 %	0.0179	2.833 %
95	1.493	0.0392	1.485	0.551 %	0.0402	2.519 %

Finally, Table 3.8 shows the drag coefficient (C_D), stagnation point heat rate (q_0), and stagnation point heat pressure (p_0) obtained from the dsmcFoam+, LAURA, and ANSYS-FLUENT computations for the 95 km altitude case. From this table, a good agreement is observed between dsmcFoam+ and both continuum solvers. LAURA presented a difference of 2.167 % compared to 2.969 % difference obtained from ANSYS-FLUENT simulations. The stagnation point heat rate (q_0) and pressure (p_0) calculated by dsmcFoam+ are in good agreement with the results calculated by the LAURA solver. The difference between

the computed results is small, and the maximum variation was 1.015% and 0.113% for heat rate and pressure at the stagnation point, respectively. When comparing the results of dsmcFoam+ with those obtained from ANSYS-FLUENT computations, a difference of 6.9% and 7.6% was found for the heat rate and pressure of the stagnation point, respectively.

Table 3.8: Drag coefficient (C_D), stagnation point heat transfer (q_0) and stagnation point pressure (p_0) calculated with dsmcFoam+ compared to the results of the LAURA solver [152] and the CFD simulations for 95 km altitude.

Parameter	dsmcFoam+	LAURA		CFD	
		Value	% Diff.	Value	% Diff.
C_D	1.493	1.461	2.167 %	1.538	2.969 %
q_0 (W/cm^2)	0.0392	0.0396	1.015 %	0.042	6.896 %
p_0 (Pa)	2.05	2.05	0.113 %	1.90	7.595 %

3.3 dsmcFoam+ code verification

To test the numerical resilience of the dsmcFoam+ code, its sensitivity to four key simulation parameters was studied. These parameters are; spatial discretization of the computational domain, time discretization, number of simulated particles and sampling effects.

Both reentry vehicles, Orion and IRVE, are used to carry out the verification process. The standard simulation parameters of the Orion crew module are described in subsection 3.1.1. These parameters are used as a standard case from which the key parameters mentioned above were tested. Similarly, the conditions and parameters described in subsection 3.1.2 for the simulation of IRVE at an altitude of H = 105 km are used as the standard case for this vehicle.

Each simulation parameter under study, for each test case considered, is analyzed through its effect on the macroscopic flow properties along the stagnation line and on the properties on the corresponding spacecraft surface. For each parameter and case tested, the macroscopic flow properties profiles over the nondimensional length of the stagnation line (x/L) considered in the analyses were; the translational temperature ratio (T_{tr}/T_∞), flow pressure ratio (P/P_∞), number density ratio (n/n_∞) and flow velocity ratio (U_x/U_∞). In addition, for each parameter and case under analysis, the skin friction coefficient (C_f), heat transfer coefficient (C_h) and pressure coefficient (C_p) along the nondimensional surface length of the corresponding spacecraft are used to further investigate the effects of the aforementioned key simulation parameters on the numerical solution.

3.3.1 Spatial discretization effects

For the Orion test case, three different mesh refinements were analyzed. The standard simulation setup, described in subsection 3.1.1, has a total of 9.20×10^5 computational cells. This standard mesh is compared to a coarser mesh of 4.33×10^5 cells and a finer mesh consisting of 1.29×10^6 cells. The average cell edge length

of the coarser and finer meshes is equivalent to $1/3$ and $1/5$ of the mean free path, respectively. Similarly, for the IRVE test case, the effects of spatial discretization on the flow solution are investigated by comparing the standard mesh, consisting of 2.53×10^5 cells, with finer and coarser grid resolutions of 6.03×10^6 and 1.20×10^5 cells, respectively. The standard, fine, and coarse meshes were defined considering an equivalent of 4 times, 6 times, and 3 times the mean free path, respectively. The mean free path ratio to the largest average cell edge length is 2.9, 3.9 and 5.6 for coarse, standard, and fine meshes.

The effects of spatial discretization on the macroscopic flow properties for the Orion and IRVE test cases are shown in Figure 3.10 and Figure 3.11, respectively. The effects of this parameter on the surface properties of each reentry vehicle are shown in Figure 3.12 and Figure 3.13, for the Orion and IRVE test cases, respectively. Moreover, for both test cases, the aerodynamic forces showed no particular sensitivity to the changes in mesh refinement. On the basis of these results, for both test cases, the set of meshes tested shows no relevant discrepancy in the calculated flow and surface properties; thus, grid independence can be ensured.

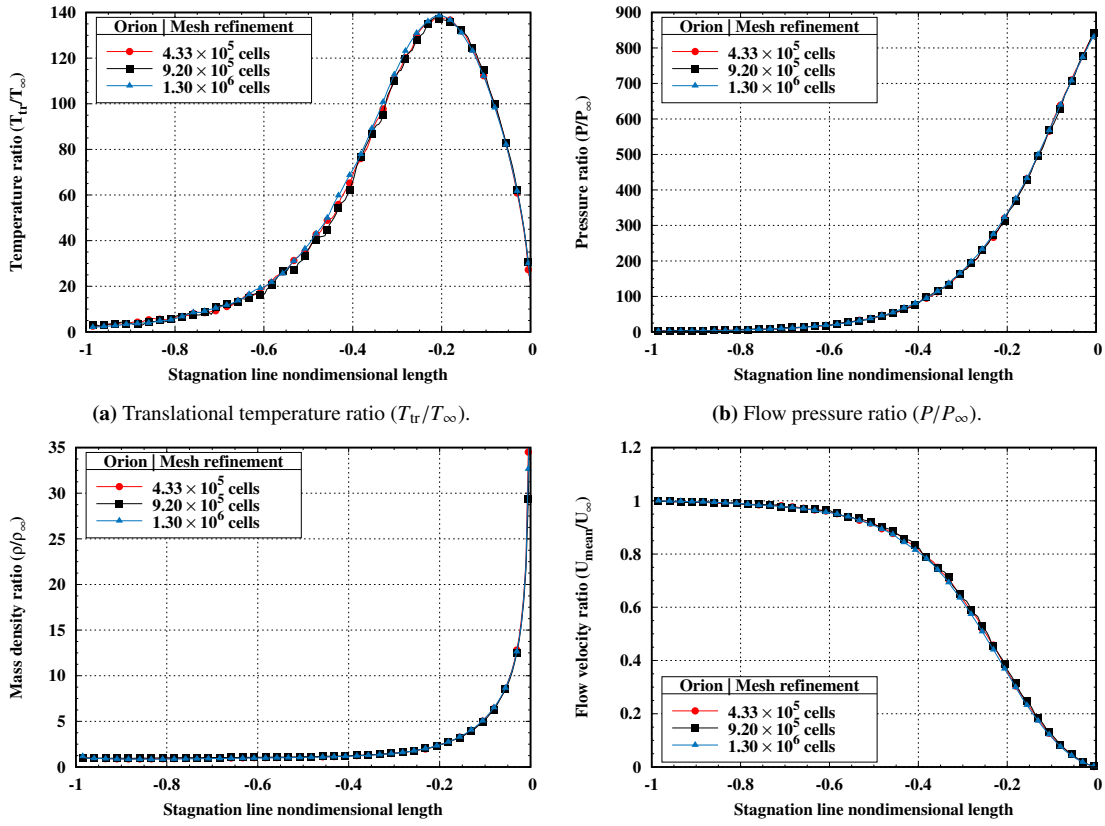

(a) Translational temperature ratio (T_{tr}/T_∞).

(b) Flow pressure ratio (P/P_∞).

(c) Mass density ratio (ρ/rho_∞).

(d) Flow velocity ratio (U_x/U_∞).

Figure 3.10: Spatial discretization effects on the flow macroscopic properties along the stagnation line nondimensional length (x/L) of Orion.

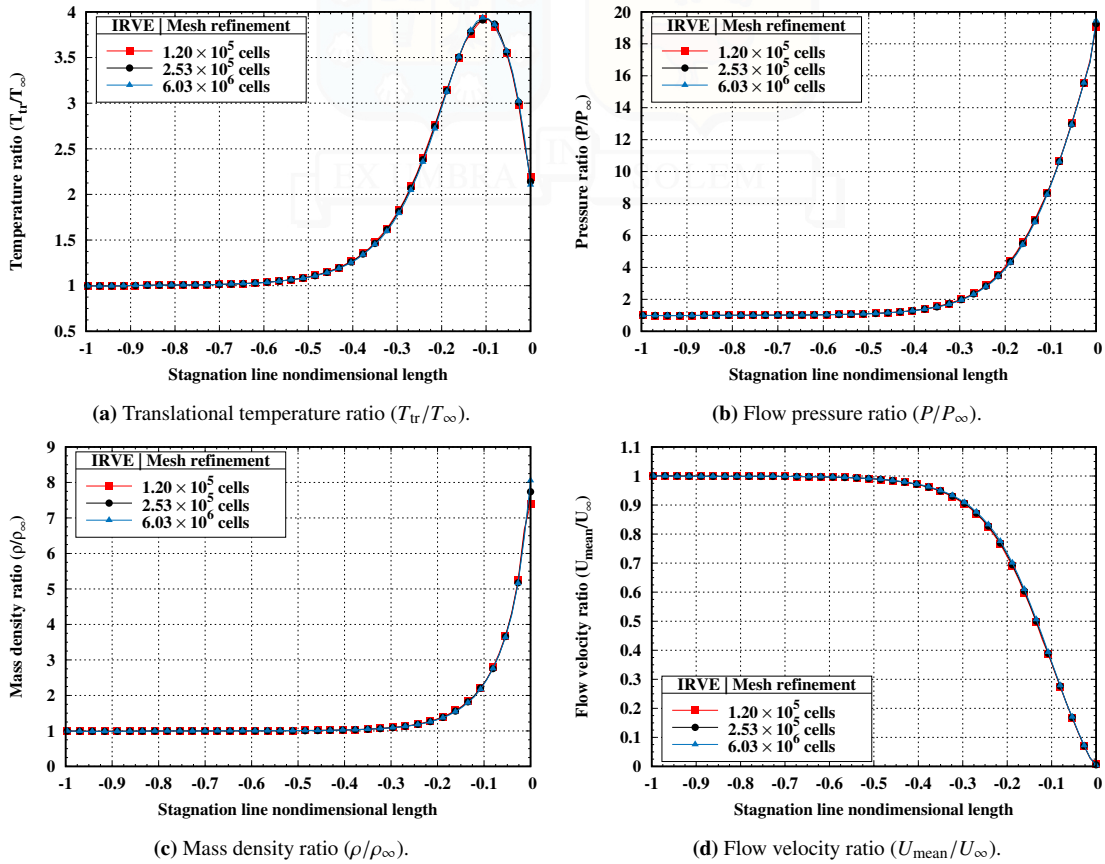

(a) Translational temperature ratio (T_{tr}/T_∞).

(b) Flow pressure ratio (P/P_∞).

(c) Mass density ratio (ρ/ρ_∞).

(d) Flow velocity ratio (U_{mean}/U_∞).

Figure 3.11: Spatial discretization effects on the flow macroscopic properties along the stagnation line nondimensional length (x/L) of IRVE.

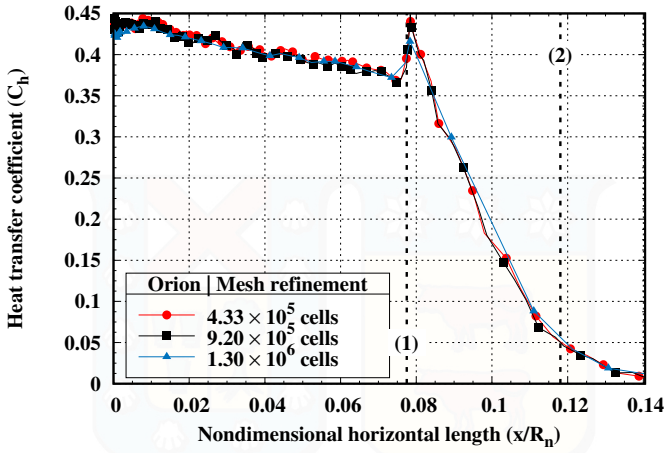

(a) Heat transfer coefficient (C_h).

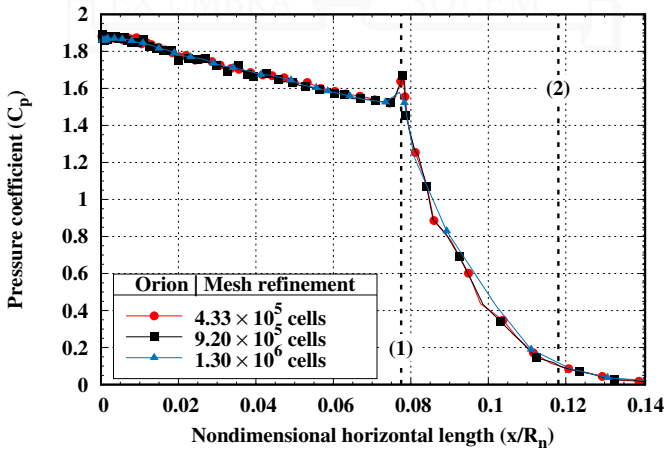

(b) Pressure coefficient (C_p).

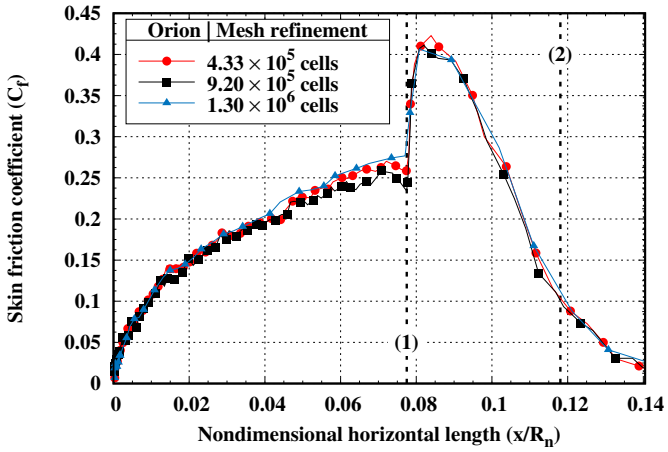

(c) Skin friction coefficient (C_f).

Figure 3.12: Spatial discretization effects on the aerothermal surface coefficients over Orion's surface nondimensional length (x/R_n).

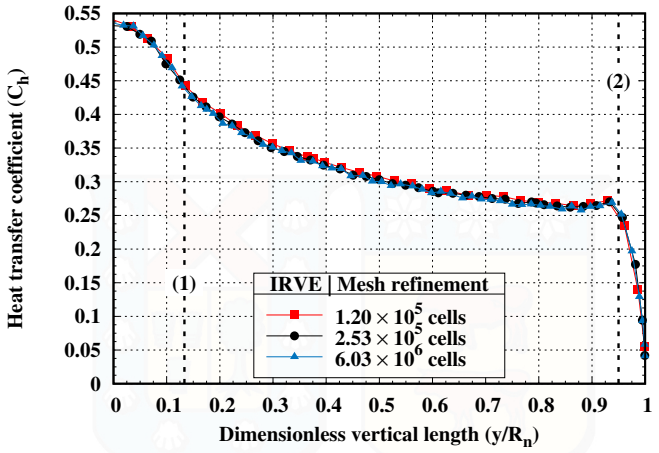

(a) Heat transfer coefficient (C_h).

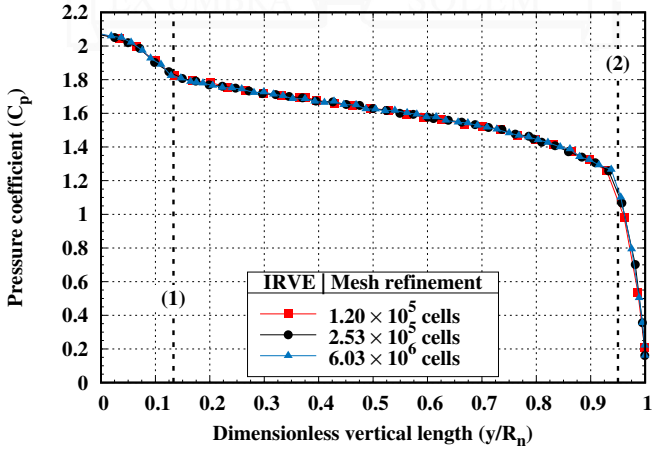

(b) Pressure coefficient (C_p).

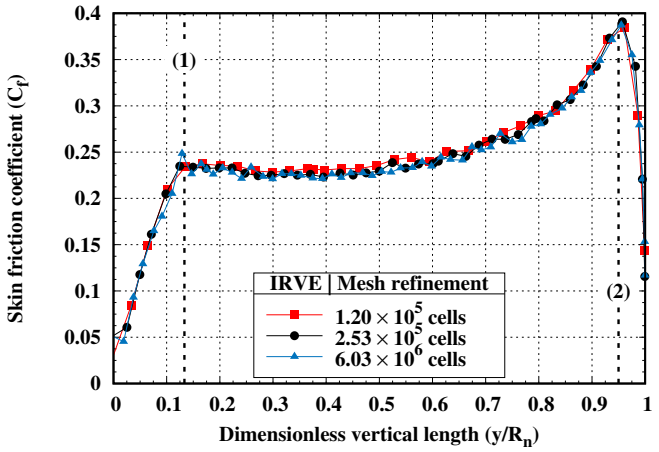

(c) Skin friction coefficient (C_f).

Figure 3.13: Spatial discretization effects on the aerothermal surface coefficients over the vertical surface nondimensional length (y/R_n) of IRVE.

3.3.2 Time discretization effects

The assessment of the code sensibility to changes in the time step size is studied through the analysis of three different time discretizations. For each spacecraft being analyzed, the corresponding standard time step value is compared with larger and smaller time steps to observe the effect of this parameter in the numerical solution. For the Orion test case, the defined standard time step value of 2.5×10^{-6} is doubled and lowered by a factor of 2.5, to 5×10^{-6} s and 1×10^{-6} s, respectively. For the time discretization analysis of the IRVE reentry vehicle, the standard time step of 1.5×10^{-5} s was doubled to 3.0×10^{-5} s and halved to 7.5×10^{-6} s. These time steps are equivalent to $2/3$, $1/3$, and $1/6$ of the residence time, respectively.

The effects of time discretization on the macroscopic properties of the flow solution for the Orion and IRVE test cases are shown in Figure 3.14 and Figure 3.15, respectively. In Figure 3.16 and Figure 3.17, the aerothermal surface coefficients are compared for each time discretization tested, for the Orion and IRVE cases, respectively. In all test cases, the behavior of the macroscopic quantities, surface properties and aerodynamic forces showed that the flow solutions are essentially independent of the time step employed.

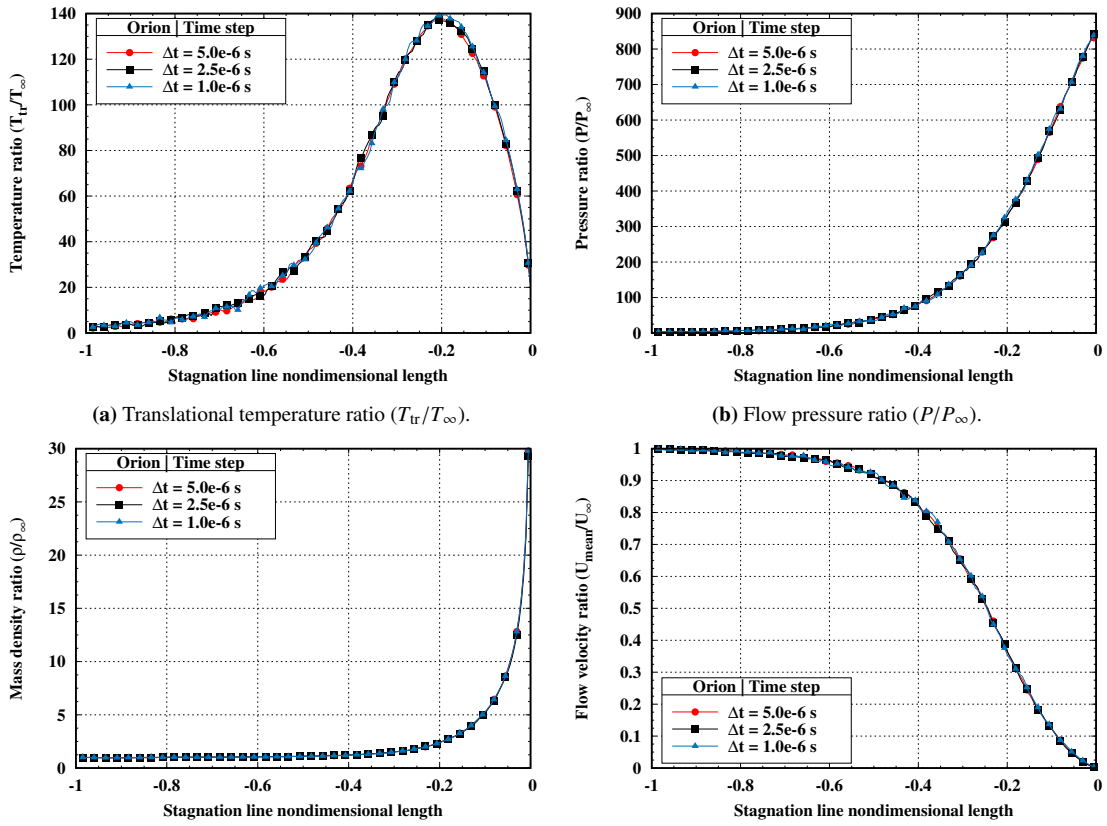

(a) Translational temperature ratio (T_{tr}/T_∞).

(b) Flow pressure ratio (P/P_∞).

(c) Mass density ratio (ρ/ρ_∞).

(d) Flow velocity ratio (U_x/U_∞).

Figure 3.14: Time discretization effects on the flow macroscopic properties along the stagnation line nondimensional length (x/L) of Orion.

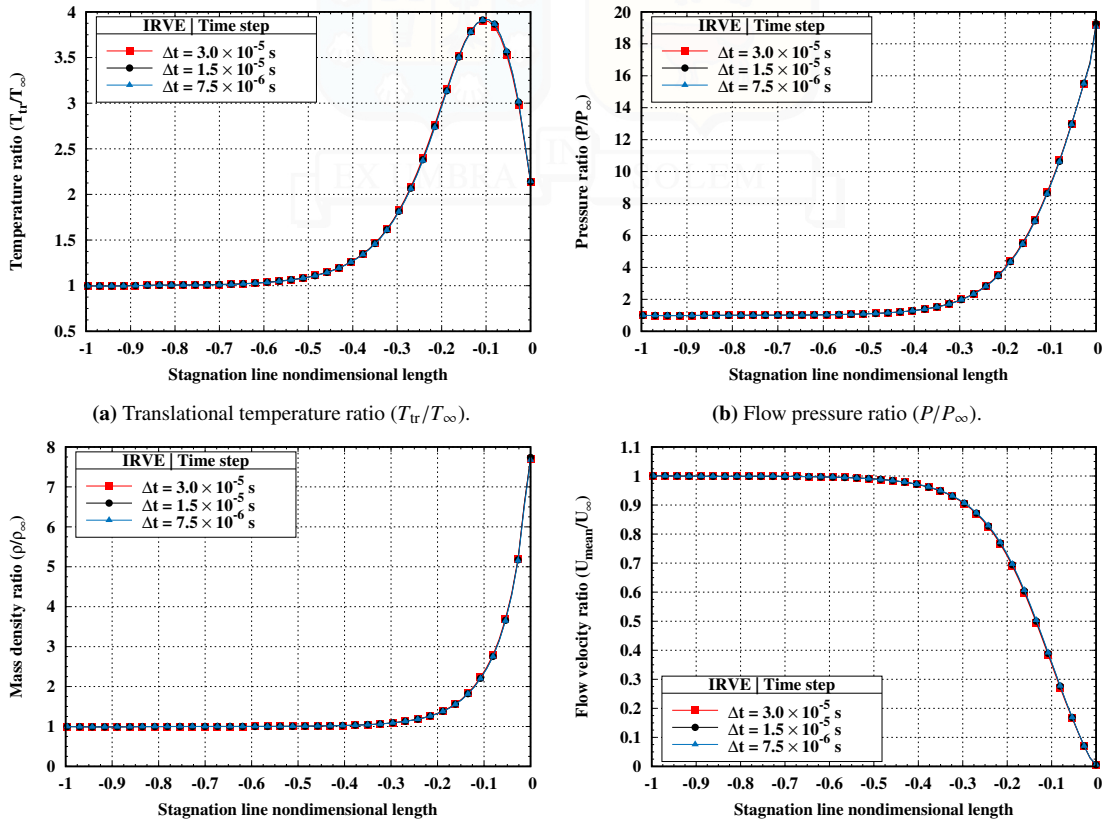

(a) Translational temperature ratio (T_{tr}/T_∞).

(b) Flow pressure ratio (P/P_∞).

(c) Mass density ratio (ρ/ρ_∞).

(d) Flow velocity ratio (U_{mean}/U_∞).

Figure 3.15: Time discretization effects on the flow macroscopic properties along the stagnation line nondimensional length (x/L) of IRVE.

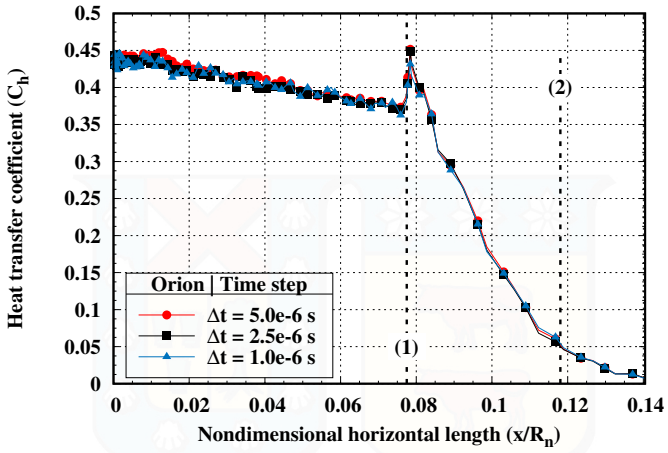

(a) Heat transfer coefficient (C_h).

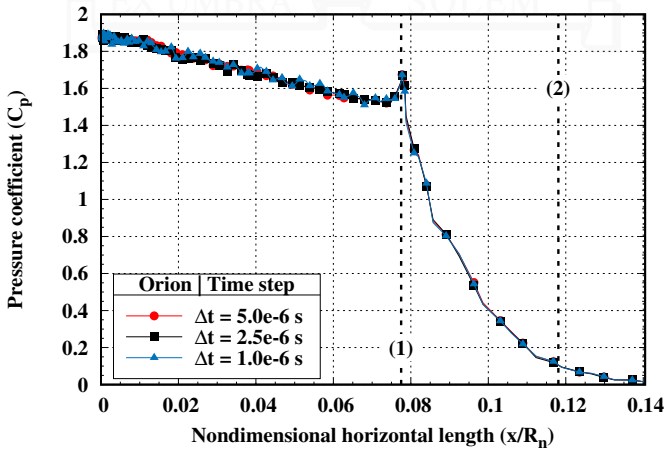

(b) Pressure coefficient (C_p).

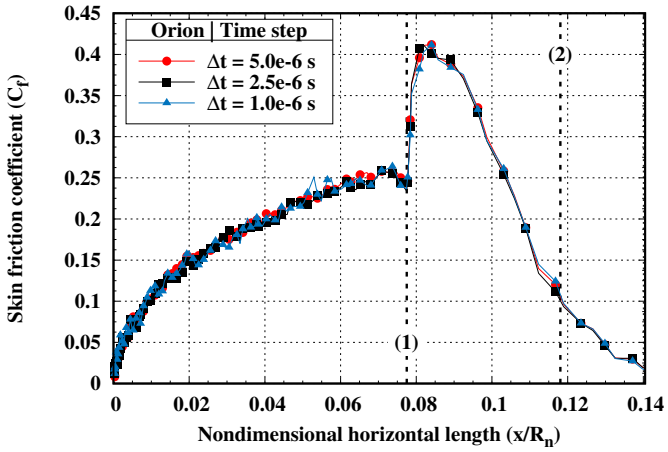

(c) Skin friction coefficient (C_f).

Figure 3.16: Time discretization effects on the aerothermal surface coefficients over Orion's surface nondimensional length (x/R_n).

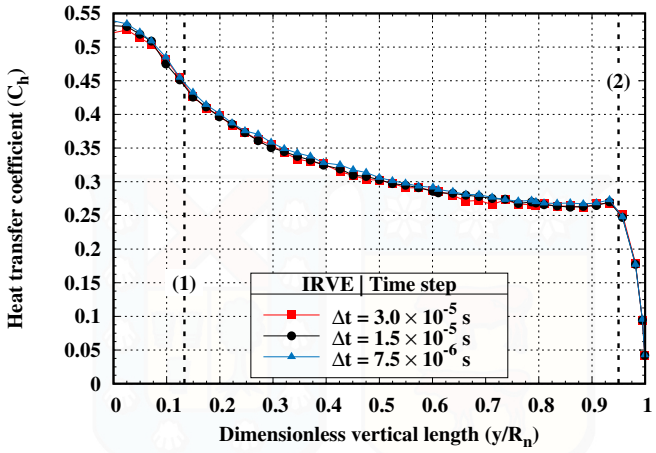

(a) Heat transfer coefficient (C_h).

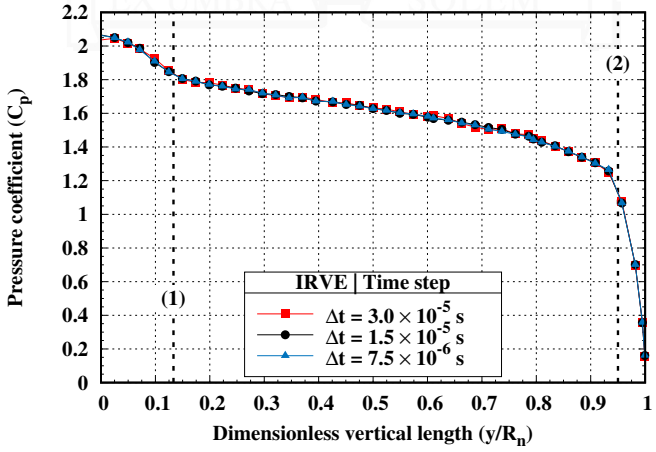

(b) Pressure coefficient (C_p).

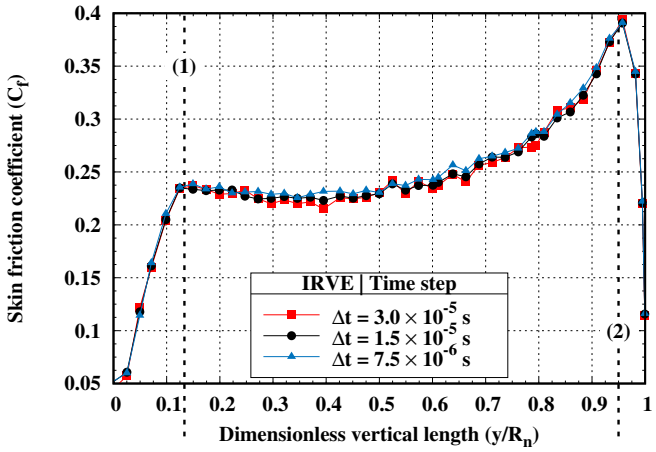

(c) Skin friction coefficient (C_f).

Figure 3.17: Time discretization effects on the aerothermal surface coefficients over the vertical surface nondimensional length (y/R_n) of IRVE.

3.3.3 Particle number assessment

The sensibility of the dsmcFoam+ code to changes in the number of particles employed is assessed by comparing three different average numbers of particles per cell during initialization. For both test cases, Orion and IRVE, the standard simulation configuration of 15 particles per cell is compared to a lower and higher value of 10 and 20 particles per cell. For the Orion test case, in steady state, the total number of particles is 1.17×10^7, 1.73×10^7, and 2.34×10^7 for 10, 15 and 20 particles per cell, respectively. For the IRVE test case, the standard simulation configuration, initialized with 15 particles per cell, reached an average of 3.79×10^6 number of particles in steady state. The other two simulations carried out, of 10 and 20 particles per cell during initialization, exhibited 2.53×10^6 and 5.06×10^6 number of particles in steady state, respectively.

In Figure 3.18 and Figure 3.19, the influence of the number of particles on the macroscopic flow properties of Orion and IRVE is shown, respectively. Similarly, the effects of the proportion of simulated particles to real molecules on the surface properties of each reentry vehicle are shown in Figure 3.20 and Figure 3.21, for Orion and IRVE, respectively. These results indicate that, under the tested conditions, the computations performed are independent of the ratio of simulated particles to real particles.

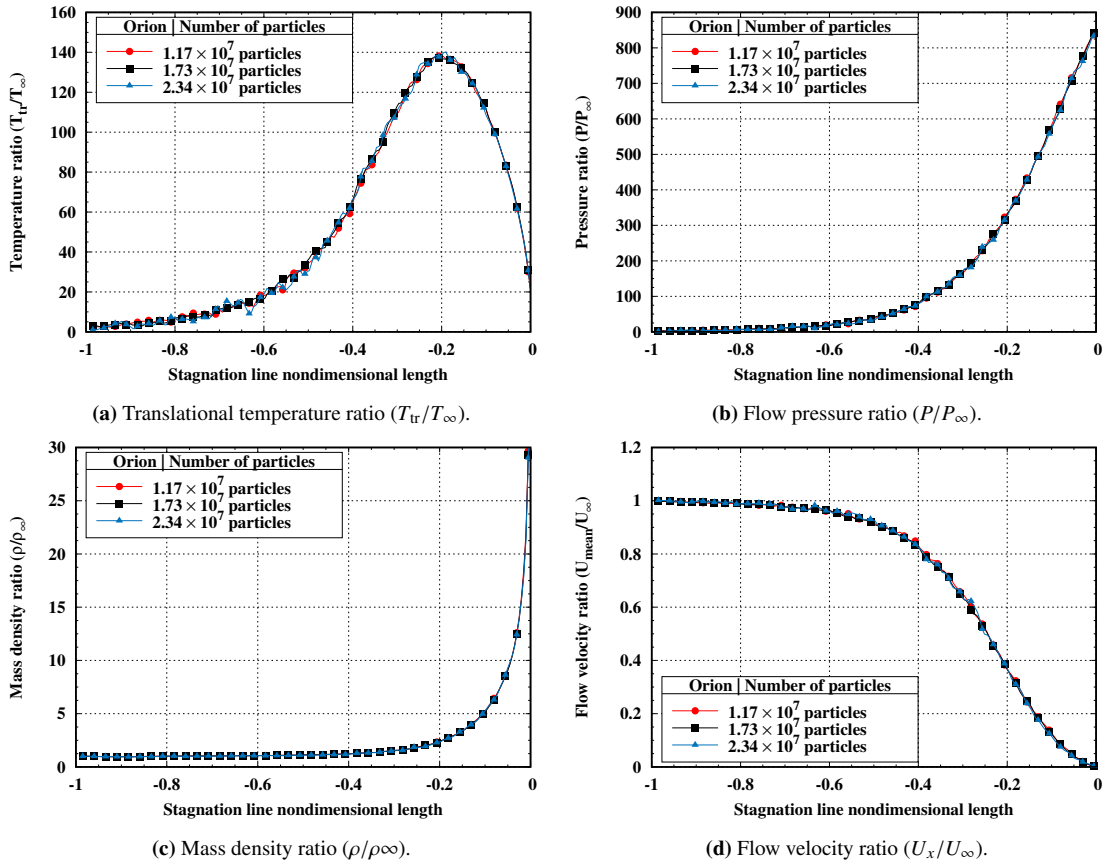

(a) Translational temperature ratio (T_{tr}/T_∞).

(b) Flow pressure ratio (P/P_∞).

(c) Mass density ratio ($\rho/\rho\infty$).

(d) Flow velocity ratio (U_x/U_∞).

Figure 3.18: Influence of the number of particles on the flow macroscopic properties along the stagnation line nondimensional length (x/L) of Orion.

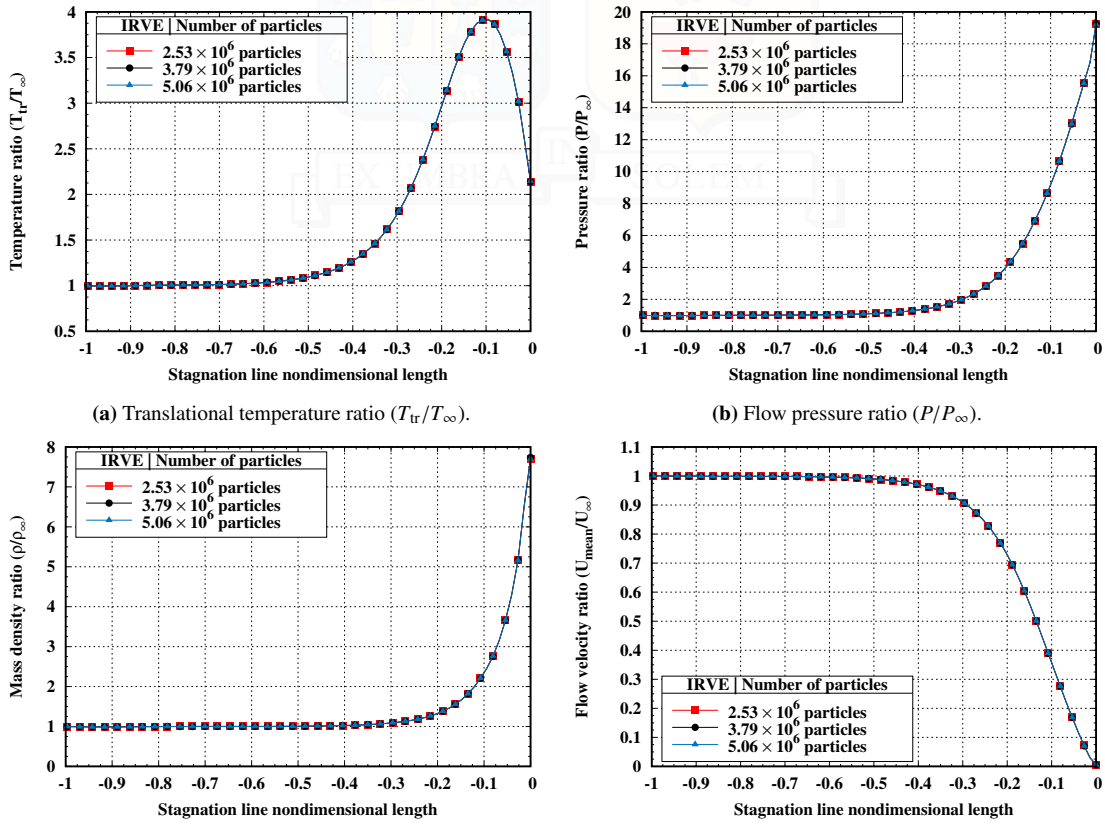

(a) Translational temperature ratio (T_{tr}/T_∞).

(b) Flow pressure ratio (P/P_∞).

(c) Mass density ratio (ρ/ρ_∞).

(d) Flow velocity ratio (U_{mean}/U_∞).

Figure 3.19: Influence of the number of particles on the flow macroscopic properties along the stagnation line nondimensional length (x/L) of IRVE.

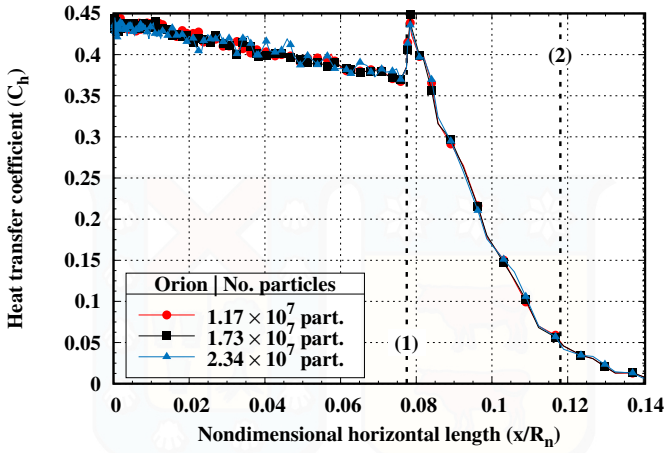

(a) Heat transfer coefficient (C_h).

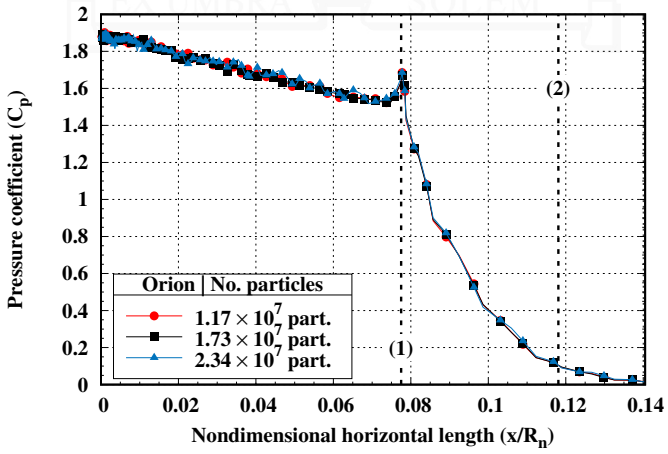

(b) Pressure coefficient (C_p).

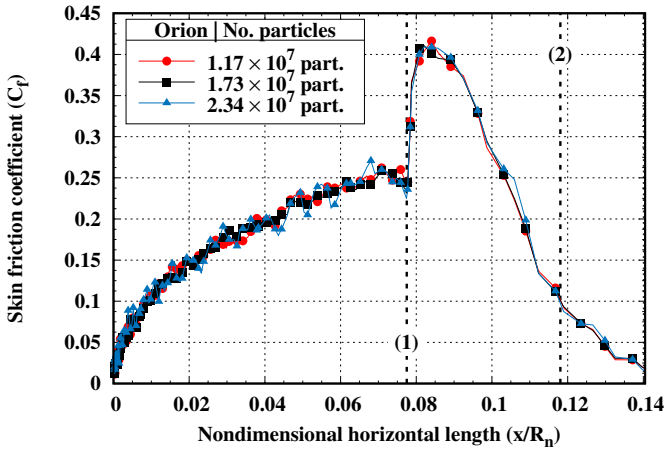

(c) Skin friction coefficient (C_f).

Figure 3.20: Influence of the number of particles on the aerothermal surface coefficients over Orion's surface nondimensional length (x/R_n).

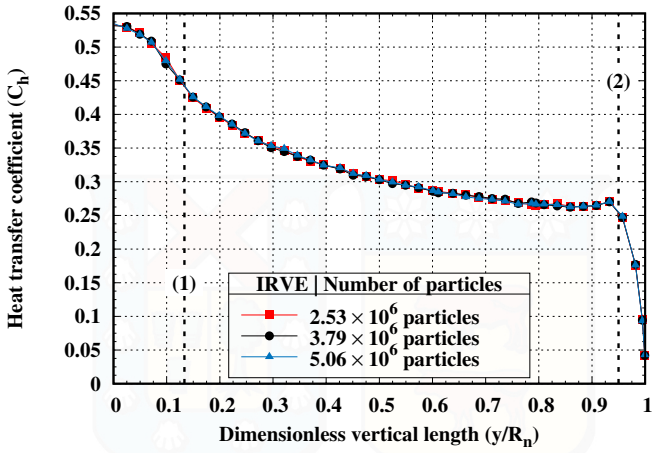

(a) Heat transfer coefficient (C_h).

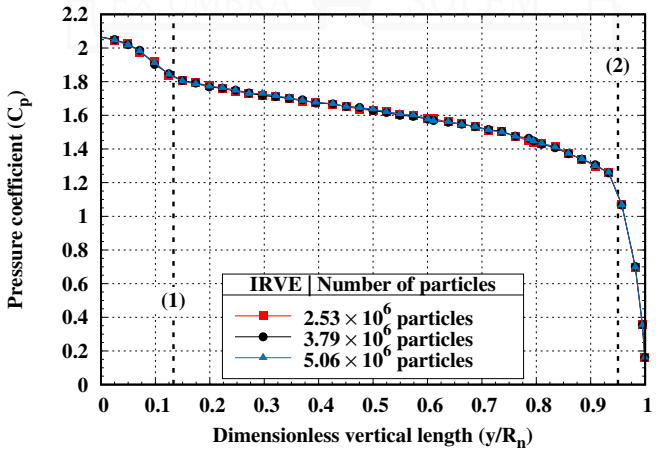

(b) Pressure coefficient (C_p).

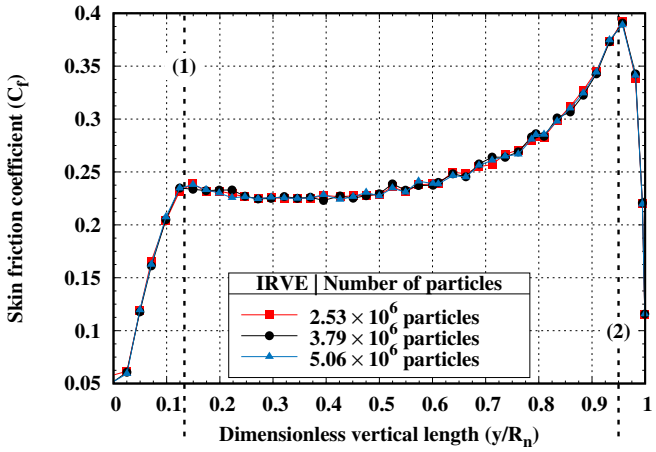

(c) Skin friction coefficient (C_f).

Figure 3.21: Influence of the number of particles on the aerothermal surface coefficients over the vertical surface nondimensional length (y/R_n) of IRVE.

3.3.4 Sampling effects

Finally, the effect of the number of sampling steps on the statistical scattering of the numerical solution is assessed. For the Orion test case, the standard simulation configuration was run for 0.6 seconds, or 2.4×10^5 time steps. Additional simulations were run until 0.3 and 0.9 seconds of simulation time, equivalent to 1.2×10^5 and 3.6×10^5 time steps, respectively. In all Orion simulations, the time averaging of the flow properties was started after 6.0×10^4 time steps, after steady state was achieved. For the IRVE test case, the standard case was run for 1 second of simulation time, or 6.6×10^4 time steps. Two more cases were run until 0.5 and 1.5 seconds of simulation time were reached, which are equivalent to 3.3×10^4 and 1.0×10^5 time step iterations, respectively. For all IRVE simulations, sampling averaging was started after 1.0×10^4 time steps, that is, once steady state was achieved. The effects of the number of sampling steps on the macroscopic flow properties along the stagnation line of Orion and IRVE are shown in Figure 3.22 and Figure 3.23, respectively. The effects of this simulation parameter on the aerothermal properties of the surface of each vehicle are shown in Figure 3.24 and Figure 3.25, for the Orion and IRVE test cases, respectively. These results show good agreement between all simulation configurations. Therefore, the number of samples of the standard cases is considered to be sufficient to make the statistical fluctuations negligible.

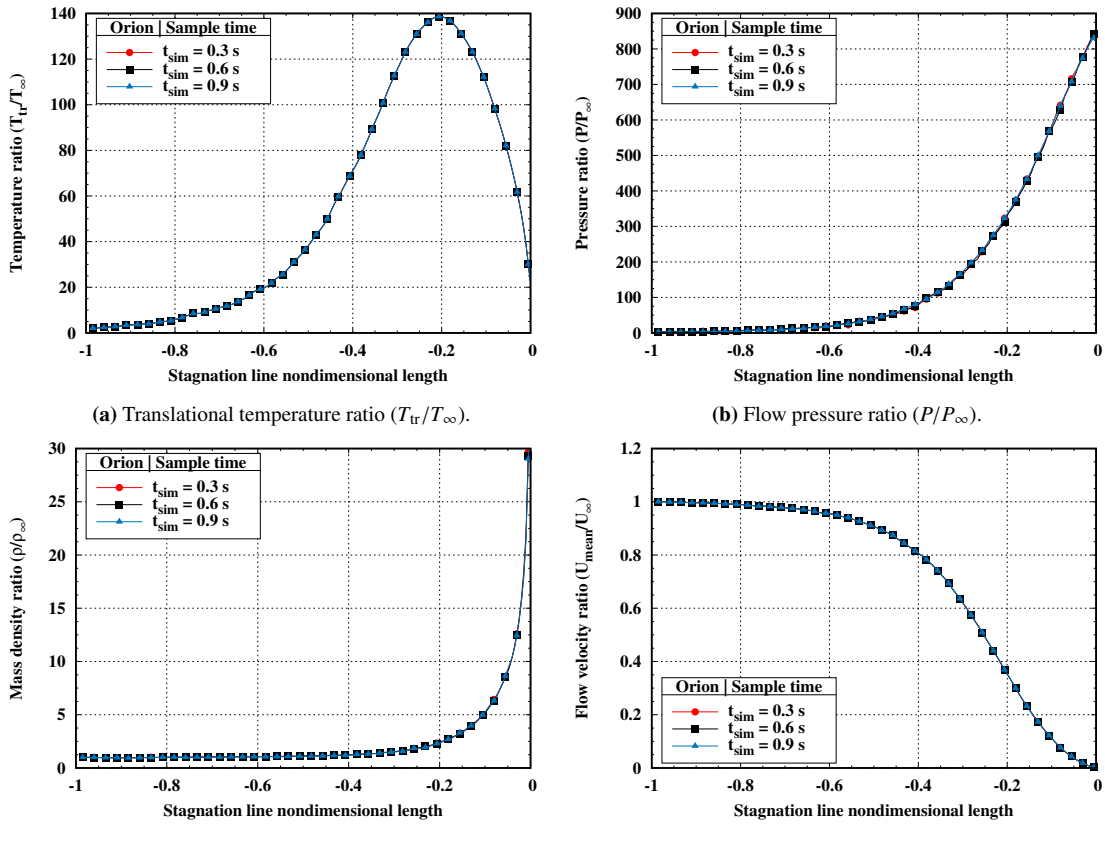

(a) Translational temperature ratio (T_{tr}/T_∞).

(b) Flow pressure ratio (P/P_∞).

(c) Mass density ratio (ρ/ρ_∞).

(d) Flow velocity ratio (U_x/U_∞).

Figure 3.22: Sampling effects on the flow macroscopic properties along the stagnation line nondimensional length (x/L) of Orion.

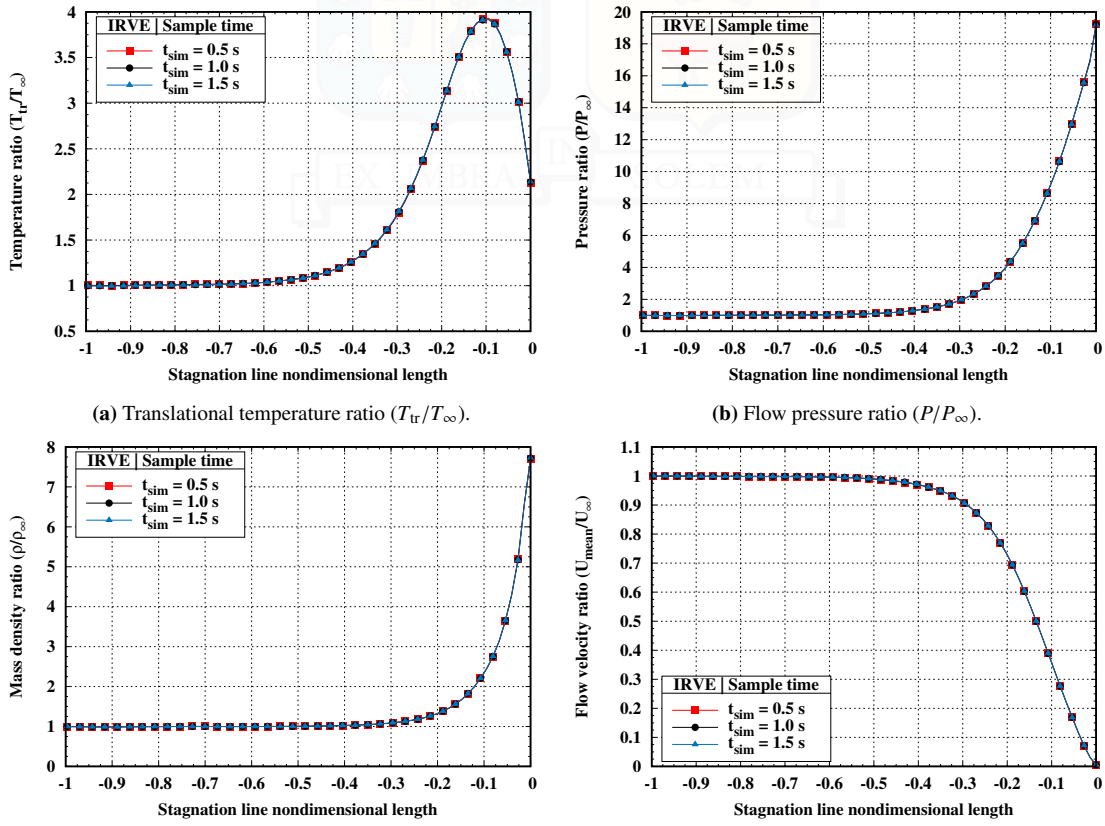

(a) Translational temperature ratio (T_{tr}/T_{∞}).

(b) Flow pressure ratio (P/P_{∞}).

(c) Mass density ratio (ρ/ρ_{∞}).

(d) Flow velocity ratio ($U_{\text{mean}}/U_{\infty}$).

Figure 3.23: Sampling effects on the flow macroscopic properties along the stagnation line nondimensional length (x/L) of IRVE.

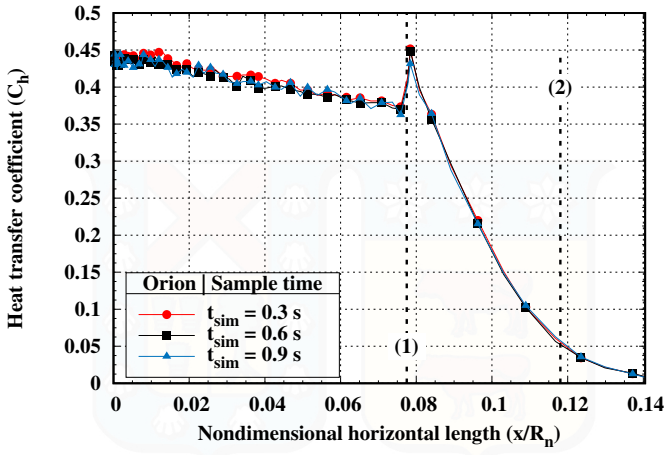

(a) Heat transfer coefficient (C_h).

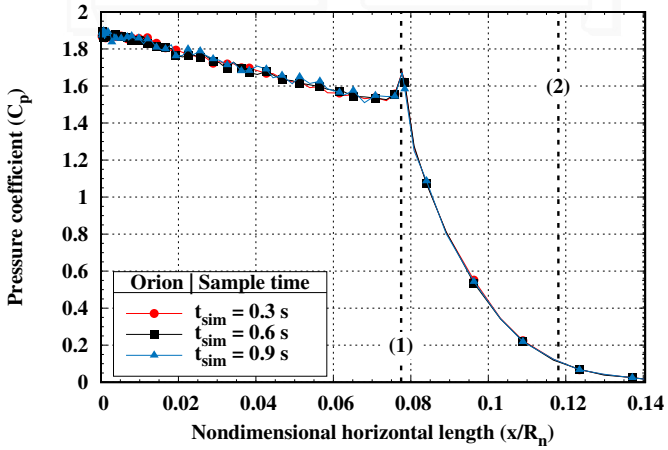

(b) Pressure coefficient (C_p).

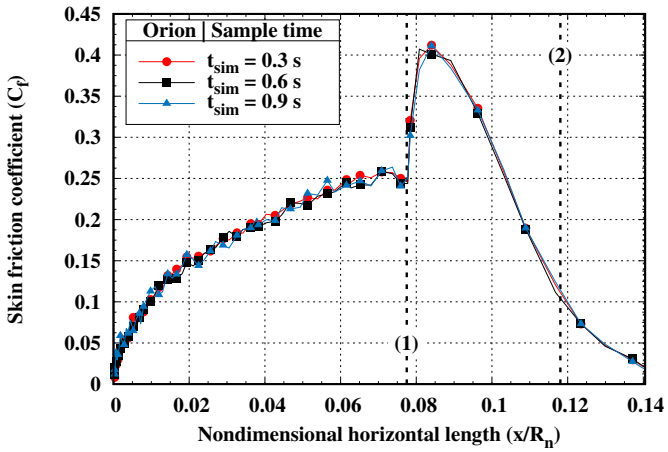

(c) Skin friction coefficient (C_f).

Figure 3.24: Sampling effects on the aerothermal surface coefficients over Orion's surface nondimensional length (x/R_n).

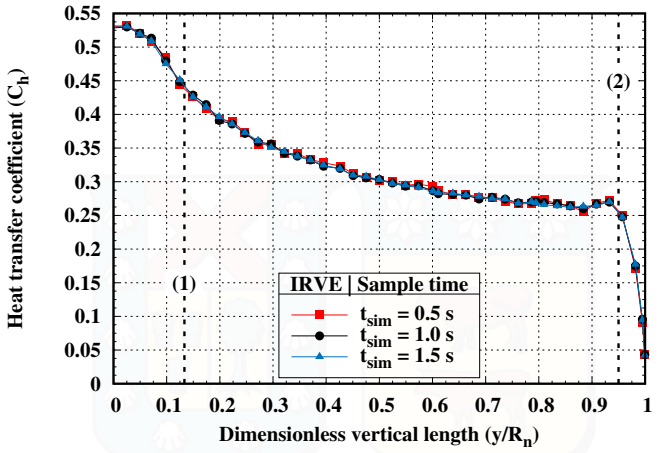

(a) Heat transfer coefficient (C_h).

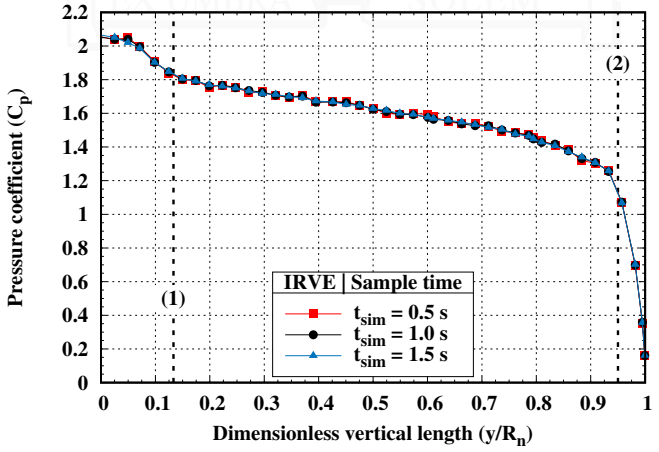

(b) Pressure coefficient (C_p).

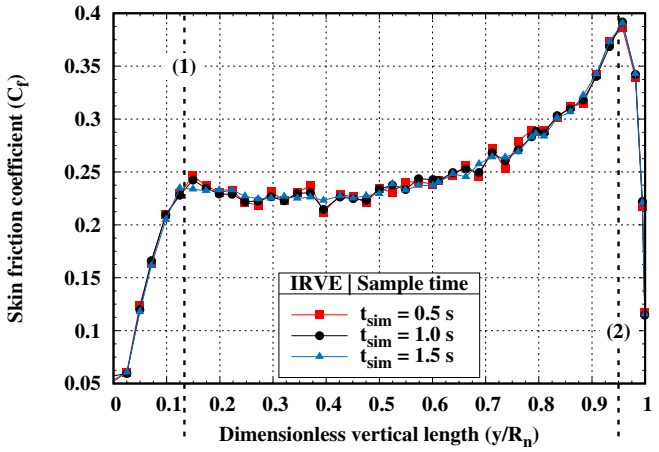

(c) Skin friction coefficient (C_f).

Figure 3.25: Sampling effects on the aerothermal surface coefficients over the vertical surface nondimensional length (y/R_n) of IRVE.

4 | Inflatable Aerodynamic Decelerators for CubeSat Reentry

Inflatable Aerodynamic Decelerator (IAD) technology is posed to become a key technology to address the challenges of CubeSat reentry and recovery and ensure a sustainable and efficient use of space. These devices are designed to expand when needed and slow down the spacecraft as it enters the planet's atmosphere, while protecting the payload from the harsh conditions of reentry. There are several IAD concepts being explored and a wide variety of shield geometry configurations have been proposed. However, as detailed in section 1.3, few aerothermodynamic analyzes have been carried out on CubeSat-sized IAD technology in rarefied reentry conditions.

The primary objective of this chapter is to assess the impact of various forebody IAD geometries on the flowfield structure and surface properties during the initial stages of reentry, where IADs are exposed to a significant degree of atmospheric rarefaction. In doing so, this work aims to further extend the understanding of the flowfield around CubeSat-based IADs and provide a useful resource for engineers and researchers developing IAD technology for CubeSat Reentry and Recovery.

This chapter presents the main results obtained from numerical simulations carried out on three distinct IAD configurations coupled with a 1U CubeSat confronted to nonreactive flow at 0° angle of attack and 105 km of altitude. The Direct Simulation Monte Carlo method is used for all computations to account for the high degree of flow rarefaction at this altitude. A detailed description of the IAD reentry vehicles and the simulation parameters employed is provided in section 4.1. The influence of the IAD forebody geometry on the flowfield structure during reentry is discussed in detail in section 4.2, where the macroscopic velocity, temperature, density, and pressure fields are carefully investigated and discussed. Subsequently, in section 4.3, the effects of the forebody geometry on the surface properties and aerodynamic forces experienced by the IAD geometries are thoroughly analyzed.

4.1 IAD simulation parameters

Three inflatable aerodynamic decelerator geometries are investigated to be used in the reentry and recovery of CubeSats. Each of the inflatable protection system under study can be stowed inside a 1U volume when folded. When fully extended, the geometry of each IAD concept is based on previously analyzed deployable or non-CubeSat IAD designs [25, 105, 38]. A complete description of each geometry is presented in Figure 4.1. In the same figure, the geometric parameters and the definition of points of interest along the IAD surface are shown. All geometries are assumed to be axisymmetric and have a maximum cross-section radius of 0.3 m.

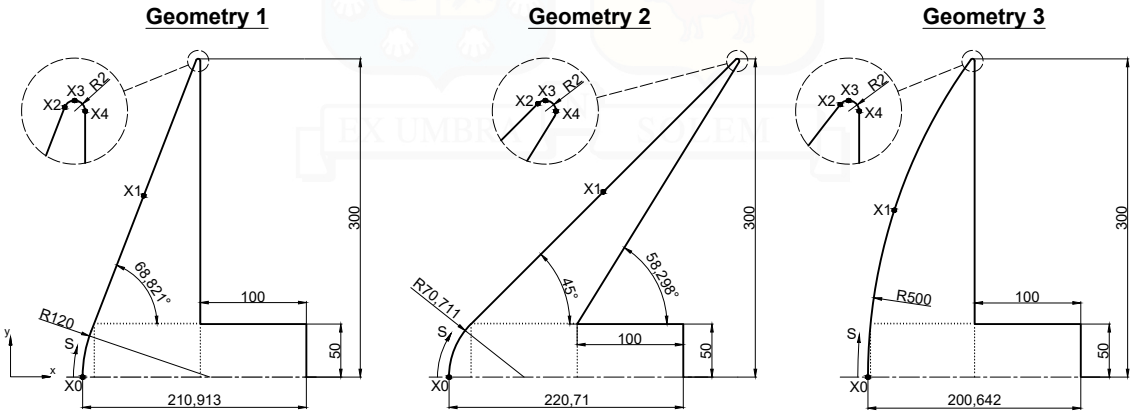

Geometry 1			
Point No.	x	y	S
X0	0.00	0.00	0.00
X1	51.63	151.48	160.31
X2	108.68	298.72	318.22
X3	110.54	300.00	320.62
X4	112.55	298.00	323.77

Geometry 2			
Point No.	x	y	S
X0	0.00	0.00	0.00
X1	127.63	155.63	204.92
X2	271.41	299.41	408.26
X3	272.83	300.00	409.83
X4	274.53	296.95	414.08

Geometry 3			
Point No.	x	y	S
X0	0.00	0.00	0.00
X1	32.79	158.52	161.30
X2	106.40	299.20	320.75
X3	108.00	300.00	322.61
X4	110.00	298.00	325.75

Figure 4.1: Geometry definition and overall dimensions.

All computations consider nonreactive flow at 0° angle of attack. The freestream properties and atmospheric composition used are described in Table 4.1 and Table 4.2, respectively. The surface temperature (T_{wall}) is set constant at 1000 K, which is representative of the surface temperature near the stagnation point. Based on the mean free path of the freestream (λ_∞), the corresponding global Knudsen number is calculated using the nose radius as the characteristic length of each vehicle. Hence, the Knudsen number is 2.8, 4.75 and 0.67 for geometries 1, 2, and 3, respectively. In this scenario, the present investigation is conducted in the transitional regime, where rarefaction effects must be acounted for.

Similarly to the simulation descriptions provided in section 3.1, for all geometries studied, the size of the computational domain is such that the shock wave structure does not reach the limits of the domain. Taking advantage of the axisymmetry of the IAD designs under investigation, only a quarter-section of the computational domain was required for the computations. Symmetry planes were employed as boundary conditions on the sides of the computational domain generated by the size reduction. As shown in Figure 4.2a, four boundary conditions are used during the DSMC computations. The flow inlet, where particles enter

Table 4.1: Freestream properties [155].

Parameter	Value	Units
Altitude	105	km
Flow speed (U_∞)	7000	m/s
Temperature (T_∞)	208.84	K
Pressure (P_∞)	0.01448	N/m^2
Density (ρ_∞)	2.33×10^{-7}	kg/m^3
Number density (n_∞)	5.02×10^{18}	m^{-3}
Mean free path (λ_∞)	3.36×10^{-1}	m

Table 4.2: Atmospheric composition at an altitude of 105 km [155].

Gas species	n (m^{-3})	X
N_2	3.89×10^{18}	0.782
O_2	7.60×10^{17}	0.153
O	3.25×10^{17}	0.065

the computational domain, is imposed on surfaces marked as I. Surface II represents a vacuum boundary condition, suitable for an outflowing gas, since there are no particles moving upstream at Mach numbers greater than 3.0 [91]. Surfaces III are defined as symmetry planes, where specular reflection is applied to colliding particles. Finally, surface IV represents the wall of the IAD coupled with a 1U CubeSat, where diffuse reflection surfaces with complete thermal accommodation are used as boundary conditions. Figure 4.2b shows a schematic of the computational mesh employed for the simulations of Geometry 1.

4.2 Macroscopic flowfield structure

The macroscopic flow and surface properties are averaged over the simulation time. Time averaging is initiated when there are no significant changes in the number of particles and the total kinetic energy in the computation domain. To ensure a statistically meaningful representation of the flow properties, a minimum of 10^4 iterations is used in all simulations. Velocity, temperature, mass density, and pressure are measured along the stagnation streamline and two profiles perpendicular to the shield's surface. As shown in Fig. 4.3, these profiles are labeled Profile 1 (P_1), Profile 2 (P_2) and Profile 3 (P_3). Profile P_1 is located at the stagnation point (X0), Profile P_2 is located at the midpoint of the frontal surface length (X1), and Profile P_3 is located at the farthest point of the shield shoulder from the center line (X3). Each profile extends from the IAD surface to the limits of the computational domain. The precise coordinate positions are described in Figure 4.1. In addition, contours of the aforementioned macroscopic properties are used to describe the flowfield structure around the IADs and 1U CubeSat payloads. Analogously, contour maps are used to describe the aerothermal properties on the IAD surfaces. The distribution of each of these properties along the nondimensional length of each IAD surface is presented.

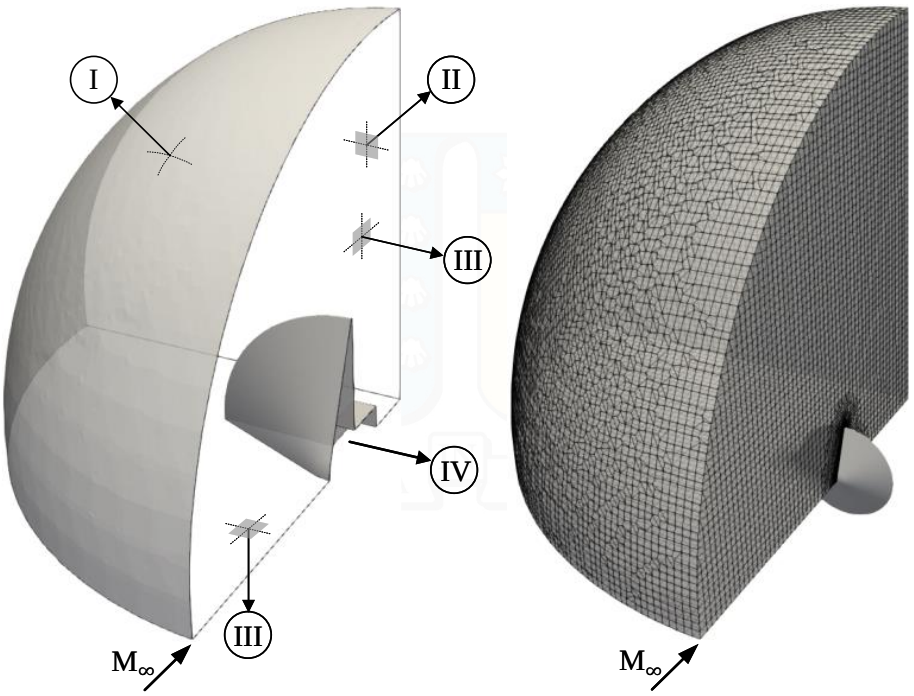

(a) Boundary denomination. **(b)** Computational mesh.

Figure 4.2: (a) Schematic computational domain boundary denomination for geometry 1. (b) Representative computational mesh for geometry 1 at H = 105 km.

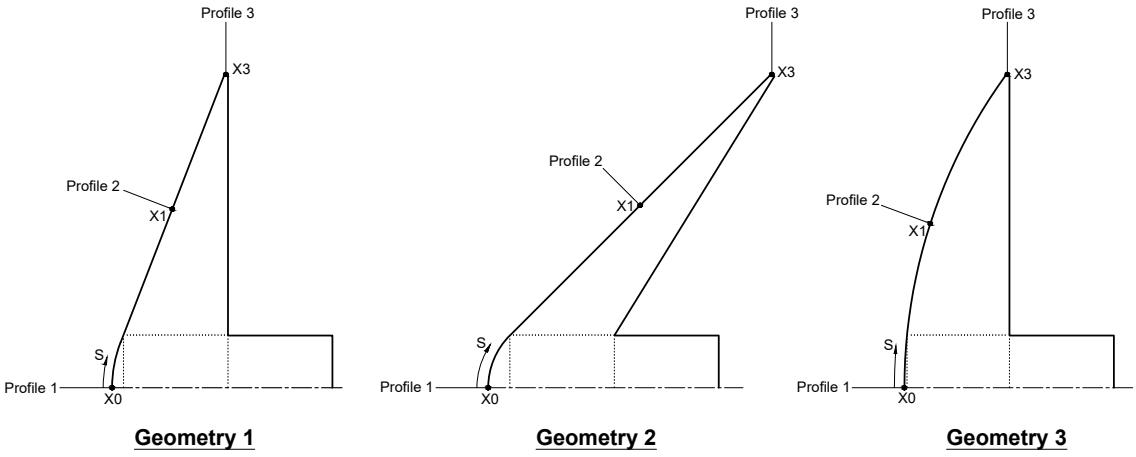

Figure 4.3: Profile lines definition and reference location.

4.2.1 Velocity flowfield

The macroscopic properties are computed from local averages of the microscopic properties. Thus, the local macroscopic velocity vector can be described by the expression

$$\boldsymbol{U} = \frac{\overline{m\boldsymbol{c}}}{\overline{m}} = \frac{\sum_{i=1}^{N} m_i \boldsymbol{c}_i}{\sum_{i=1}^{N} m_i}, \tag{4.1}$$

where m and $\boldsymbol{c}$ represent the mass and velocity vector of each individual particle, and N is the total number of simulated particles within a cell.

Figure 4.4 shows the flow velocity ratio contours and streamlines for each IAD geometry considered in the present investigation. On the left-hand side of the figure, the entire computational domain is shown, and, on the right-hand side, a closer view of the flowfield over the spacecraft is presented. According to Figure 4.4, the freestream particles enter the computational domain at a velocity of 7000 m/s, which gradually decreases as the flow approaches the spacecraft shield. When the freestream particles strike the IAD surface, a low-velocity region is formed over the shield surface. As the flow moves over the shield surface and expands at the IAD shoulder, a low-speed wake region with well-defined streamlines is observed behind the shield. A general resemblance can be distinguished between the contour level's shape for blunt geometries, that is, Geometry 1 and Geometry 3, which have a larger zone of slow-moving flow in front of the shield. In contrast to this, the flow speed flow around Geometry 2 decreases rapidly closer to its surface, which is related to the aerodynamic shape of the aeroshell. Furthermore, taking the stagnation line as a reference, the flow velocity in front of the shield reaches a third of the freestream velocity 0.14 m upstream from the stagnation point of Geometry 1, 0.06 m for Geometry 2, and 0.16 m for Geometry 3. However, at the shield's shoulder edge, the slow-moving flow close to the surface quickly accelerates to values near the freestream velocity. Hence, following the path described by the streamlines, slow particles near the front of the shield move along the surface until they reach the IAD shoulder, where the flow expands and particles are able to recover the freestream velocity. Due to the elongated shape of Geometry 2, the low-speed flow zone extends further downstream compared to the flow associated with Geometry 1 and Geometry 3. At this altitude, the streamlines show that the flow behind the shield of Geometry 2 is more erratic, due to the lack of molecular collisions.

In Fig. 4.5, the flow velocity ratio is presented for the three profiles described in Fig. 4.3. The pictures on the left side of Fig. 4.5 show the velocity ratio over the complete extension of each profile for all geometries, whereas the pictures on the right side of Fig. 4.5 focus on the portion closer to the IAD's surface, showing a tenth of the profile's full extension. From this figure, it can be observed that the flow speed is equal to the freestream velocity near the edges of the domain, corroborating the observations made from

Fig. 4.4. It can also be seen that, for profiles 1 and 2, the reduction in flow speed starts earlier for geometries 1 and 3 than for Geometry 2. This is related to the bluntness of Geometry 1 and Geometry 3, contrary to the more aerodynamic shape of Geometry 2. However, this is not the case for profile P_3, where the velocity distribution is very similar for all geometries. Looking at the profile P_1, before reaching the stagnation point, the flow velocity associated with Geometry 2 can be approximately double than that of geometries 1 and 3. This difference gradually reduces until all geometries reach a value of zero at the stagnation point. A similar behavior can be observed for profile P_2, where again the flow velocity associated with Geometry 2 is consistently higher than the other geometries. However, at this location, none of the geometries reached a velocity value of zero close to the surface. This is because in DSMC simulations the no-slip condition is not enforced, thus, profile P_2 shows that there is velocity slip at the midpoint of each geometry's surface length. The same can be observed for profile P_3, where all velocity distributions are close together and reach a non-zero minimum at the shoulder's farthest away point.

4.2.2 Temperature field

For non-equilibrium gas, the translational temperature (T_{tr}), rotational temperature (T_{rot}), and vibrational temperature (T_{vib}) in each cell in the computational domain are calculated as

$$T_{\text{tr}} = \frac{1}{3k_b}\overline{m\boldsymbol{c'}^2} = \frac{1}{3k_b}\frac{\sum_{i=1}^{N} m_i \boldsymbol{c'}^2}{N}, \tag{4.2}$$

$$T_{\text{rot}} = \frac{2m\bar{\varepsilon}_{\text{rot}}}{k_b\zeta_{\text{rot}}} = \frac{2}{k_b\zeta_{\text{rot}}}\frac{\sum_{i=1}^{N}(\varepsilon_{\text{rot}})_i}{N}, \tag{4.3}$$

$$T_{\text{vib}} = \frac{\Theta_{\text{vib}}}{\ln\left(1+\frac{k_b\Theta_{\text{vib}}}{\bar{\varepsilon}_{\text{vib}}}\right)} = \frac{\Theta_{\text{vib}}}{\ln\left(1+\frac{k_b\Theta_{\text{vib}}}{\sum_{i=1}^{N}(\varepsilon_{\text{vib}})_i}\right)}, \tag{4.4}$$

where k_b represents the Boltzmann constant, **c'** is the thermal velocity, ζ the degrees of freedom, $\bar{\varepsilon}_{\text{rot}}$ and $\bar{\varepsilon}_{\text{vib}}$ are the average rotational and vibrational energies per particle calculated within the respective cell and Θ_{vib} the characteristic vibrational temperature.

On the left-hand side of Figure 4.6, the nondimensional translational temperature contours are shown, and, on the right-hand side of the same figure, an amplified view of the temperature contours close to the IAD geometries is presented. According to this figure, a high-temperature shock wave is formed upstream of the IAD coupled to a 1U CubeSat. The shock wave originates from particles that are reflected from the surface of the spacecraft and collide with incoming freestream particles. In addition, it can be observed that the IAD geometry has a significant influence on the shock wave structure and peak temperature. Careful

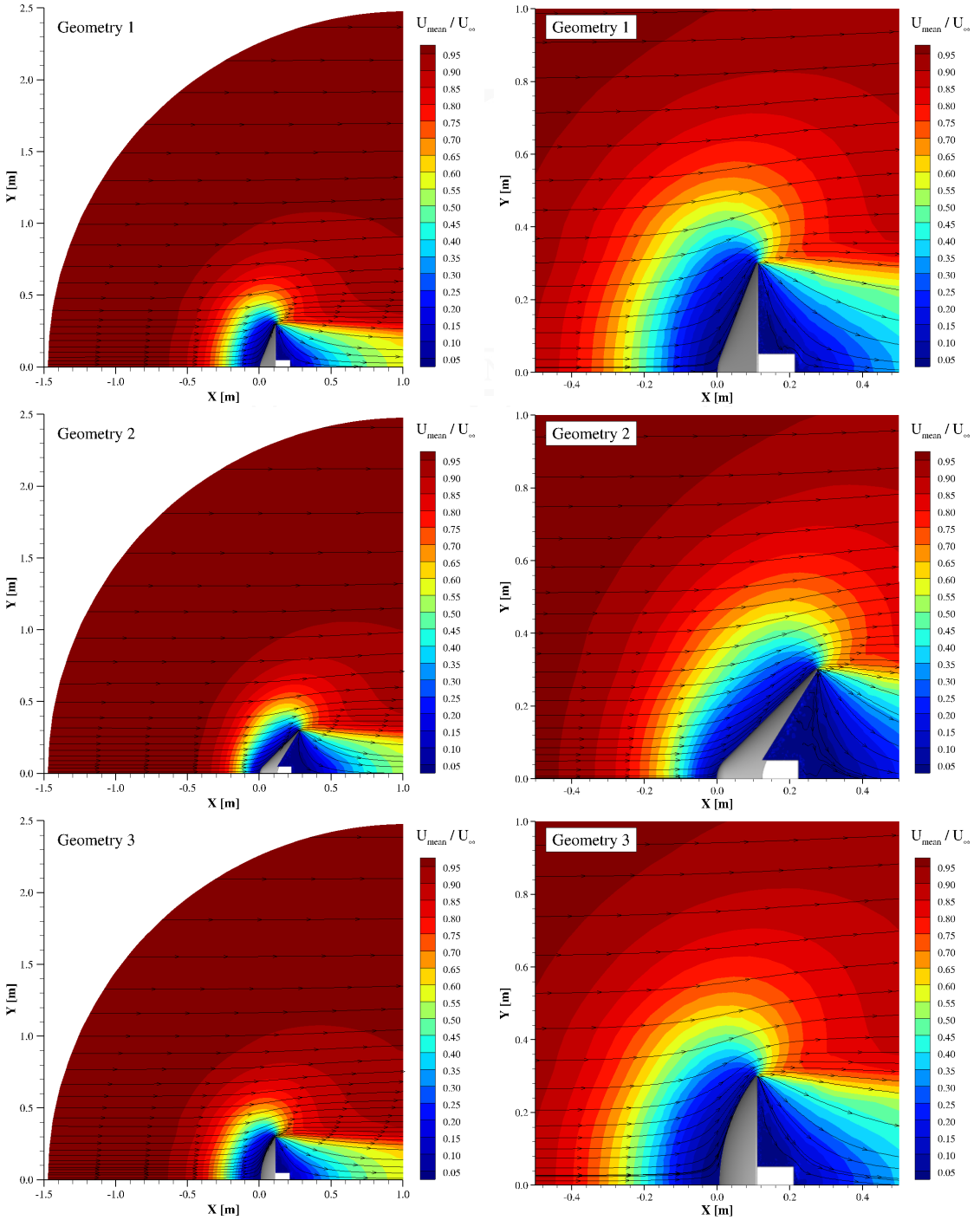

Figure 4.4: Velocity ratio contours and streamlines around the simulated geometries. Left: Full computational domain. Right: Closer view of the flowfield near the spacecraft.

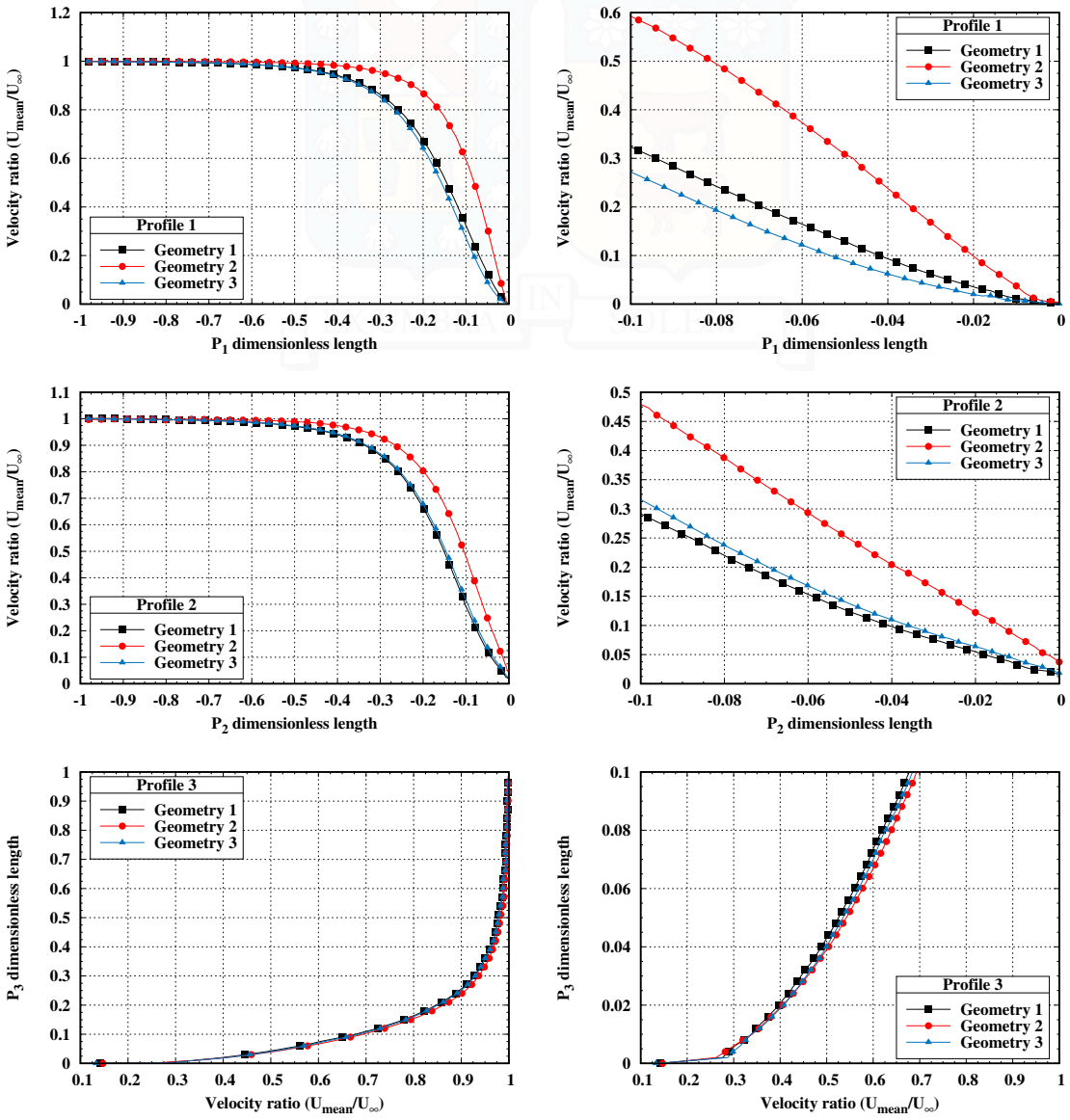

Figure 4.5: Velocity ratio along profiles normal to each geometry's surface. Left: Full computational domain. Right: Closer view of the flowfield near the spacecraft.

observation of the right side of Figure 4.6, shows that the high-temperature region of Geometry 2 is thinner and closer to the shield's surface when compared to Geometry 1 and Geometry 3. In this regard, considering the stagnation line as reference, the high-temperature region is 60 times the freestream temperature, 0.32 m thick and is located 0.06 m upstream of the shield's surface for Geometry 1 and Geometry 3. On the other hand, the high-temperature region associated with Geometry 2 is 0.16 m thick and 0.02 m upstream of the IAD surface, approximately half of the values observed for Geometries 1 and 3. However, towards the edge of the shield, there is an increase in the shock wave thickness corresponding to Geometry 2. Geometry 1 presents the maximum temperature contour level with the largest area, while Geometry 2 has the smallest maximum temperature contour level out of all vehicles. Moreover, the shock wave associated with Geometry 3 is observed to have the thickest maximum temperature contour level area of all geometries studied. The temperature contour levels in the wake region show that the gas temperature behind the IAD aeroshell is close to the freestream temperature, increasing to about 40 times the freestream temperature, 8353.6 K, at the wake's inner field behind each vehicle. Due to the shape of Geometry 2, the low-temperature region extends further downstream, which could be used to protect bigger nanosatellites, such as a 3U CubeSat.

In order to further understand the nature of the high-temperature shock wave region, the nondimensional translational temperature profiles for three profiles normal to the IAD surface are shown in Figure 4.7. From this set of figures, it is observed that the maximum temperature inside the shock wave ranges from 85 to 90 times the freestream temperature, depending on the IAD geometry. Furthermore, Geometry 1 and Geometry 3 presented similar behavior concerning the translational temperature distribution along the profiles. Concerning profile P_1, stagnation streamline, Figure 4.7 corroborates the contour maps, Figure 4.6, where it is noticed that Geometry 2 presented the lowest shock wave temperature, its maximum being 85 times the freestream temperature with its peak temperature closer to the shield's surface when compared with the other two geometries. Since the shock wave is closer to the vehicle surface, it is observed that the stagnation temperature for Geometry 2 is higher when compared to Geometry 1 and then Geometry 3. Profile P_2 shows a similar behavior to profile P_1; however, the differences in translational temperature distribution along the profile are less pronounced between the geometries. Close to the IAD surface, it is observed in profile P_2 that Geometry 2 has a higher gas temperature when compared to the other two geometries. It is observed from profile P_3 that Geometry 2 presented a lower temperature distribution when compared to Geometries 1 and 3. Due to the cone angle of 45°, the flow expansion over the IAD Geometry 2 is more intense and promotes a reduction in the translation temperature profile at this region.

Furthermore, using the methodology employed by Santos *et al.* [156], the characteristics of the shock wave structure in a transitional flow regime are specified. All of these parameters are calculated using the distribution of the temperature field on the stagnation line, as shown in profile P_1 in Figure 4.7. In Table 4.3 the maximum temperature inside the shock wave, the distance from the shock wave to the vehicle, and the thickness of the shock wave are presented. The standoff distance is defined as the distance from the center of the shock wave to the stagnation point, where the center of the shock wave is defined as the location of the

maximum temperature inside the shock wave. The thickness of the shock wave is defined as the distance of the stations corresponding to the mean temperature, that is, the average between the maximum and minimum temperatures at the center of the shock wave and the stagnation point. According to Table 4.3, similarities on the maximum temperature, standoff distance, and shock wave thickness can be observed for Geometries 1 and 3. When comparing the computed parameters for Geometries 1 and 3 with those obtained for Geometry 2, it is observed that the difference in peak temperature within the shock wave is approximately 1100 K, the standoff distance is 0.07 m smaller, and shock wave is 0.1185 m thinner for Geometry 2.

Table 4.3: Defining characteristics of the shock wave structure.

	Geometry 1	Geometry 2	Geometry 3
Max temperature (K)	18784.1	17662.2	18770.7
Standoff distance (m)	0.1849	0.1130	0.1893
Thickness (m)	0.3279	0.2094	0.3379

4.2.3 Density field

The macroscopic mass density within the computational cells on the dsmcFoam+ code is calculated as

$$\rho = n\overline{m} = \frac{\overline{N}F_N}{V_c}\frac{\sum_{i=1}^{N} m_i}{N}, \tag{4.5}$$

where n is the local number density, m is the molecular mass, and $\overline{N}$ and N are the average and total number of simulated particles within a given cell, respectively. Furthermore, F_N represents any number of real particles and V_c is the computational cell volume.

Figure 4.8 shows the mass density ratio contour map describing the flow around the simulated reentry vehicles. The same contour levels are used for all geometries, which are defined based on the maximum value of density ratio among the three vehicles, corresponding to Geometry 3. As can be seen in the pictures on the left-hand side of Figure 4.8, which show the entirety of the simulated domain, most of the mass density field is undisturbed by the geometries. However, a notable increase in mass density ratio in the area surrounding each spacecraft can be observed in the images on the right-hand side of Figure 4.8. Furthermore, the major effects of each geometry on the flow mass density are limited to the immediate region in front of the shield, where all geometries reach their corresponding maximum density ratio. Here, Geometry 1 shows values closer to those observed for Geometry 3, with a maximum density contour level of 30 times the freestream density, the highest of all geometries under study. On the other hand, Geometry 2 is observed to have a maximum contour level of approximately 22 times the freestream density, which is the lowest of all and differs from the values observed for Geometry 1 and Geometry 3 by a significant margin. Due to their blunt format, Geometry 1 and Geometry 3 cause greater interference in the path of particles, leading to a thicker layer of DSMC particles

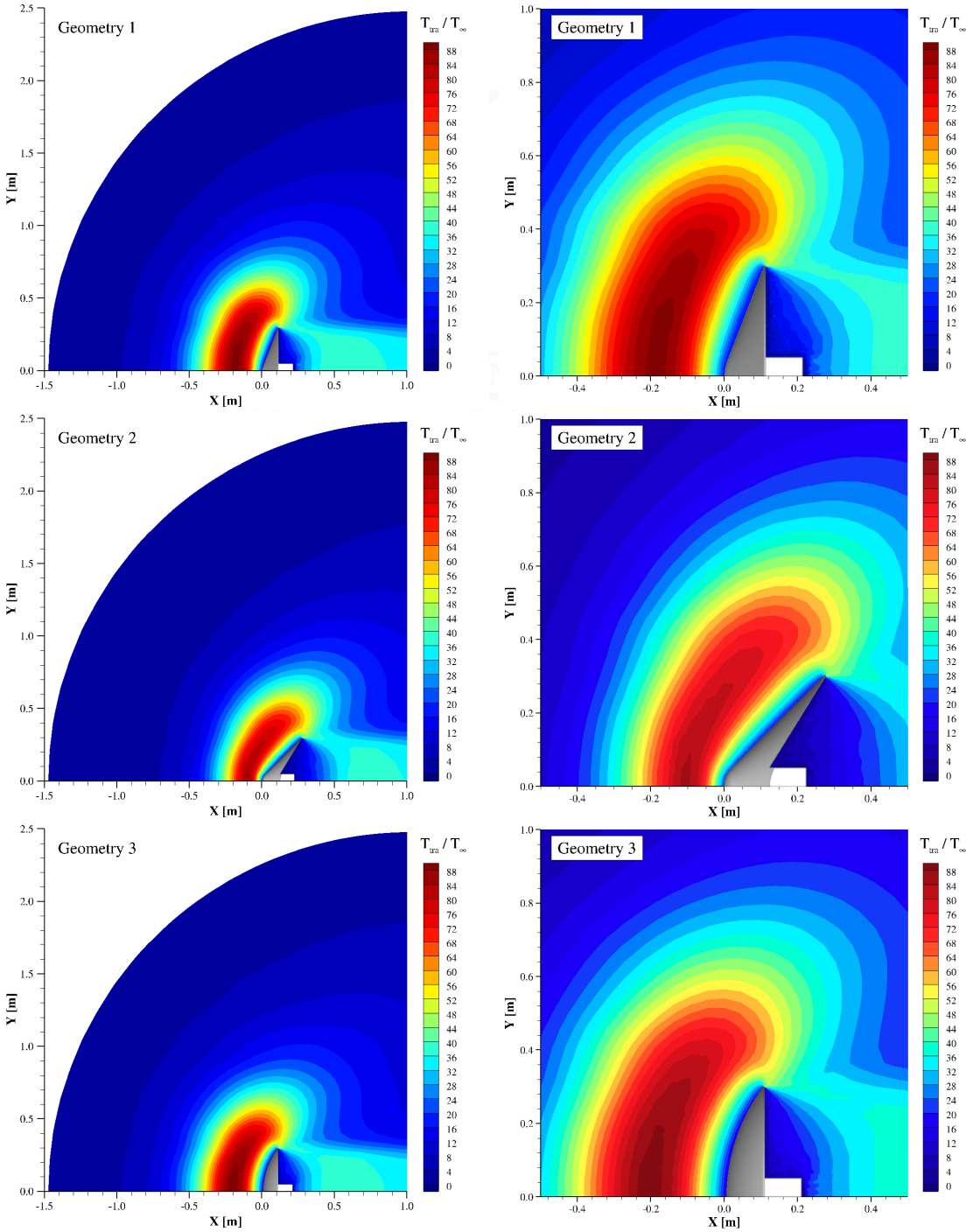

Figure 4.6: Translational temperature ratio contours around the simulated geometries. Left: Full computational domain. Right: Closer view of the flowfield near the spacecraft.

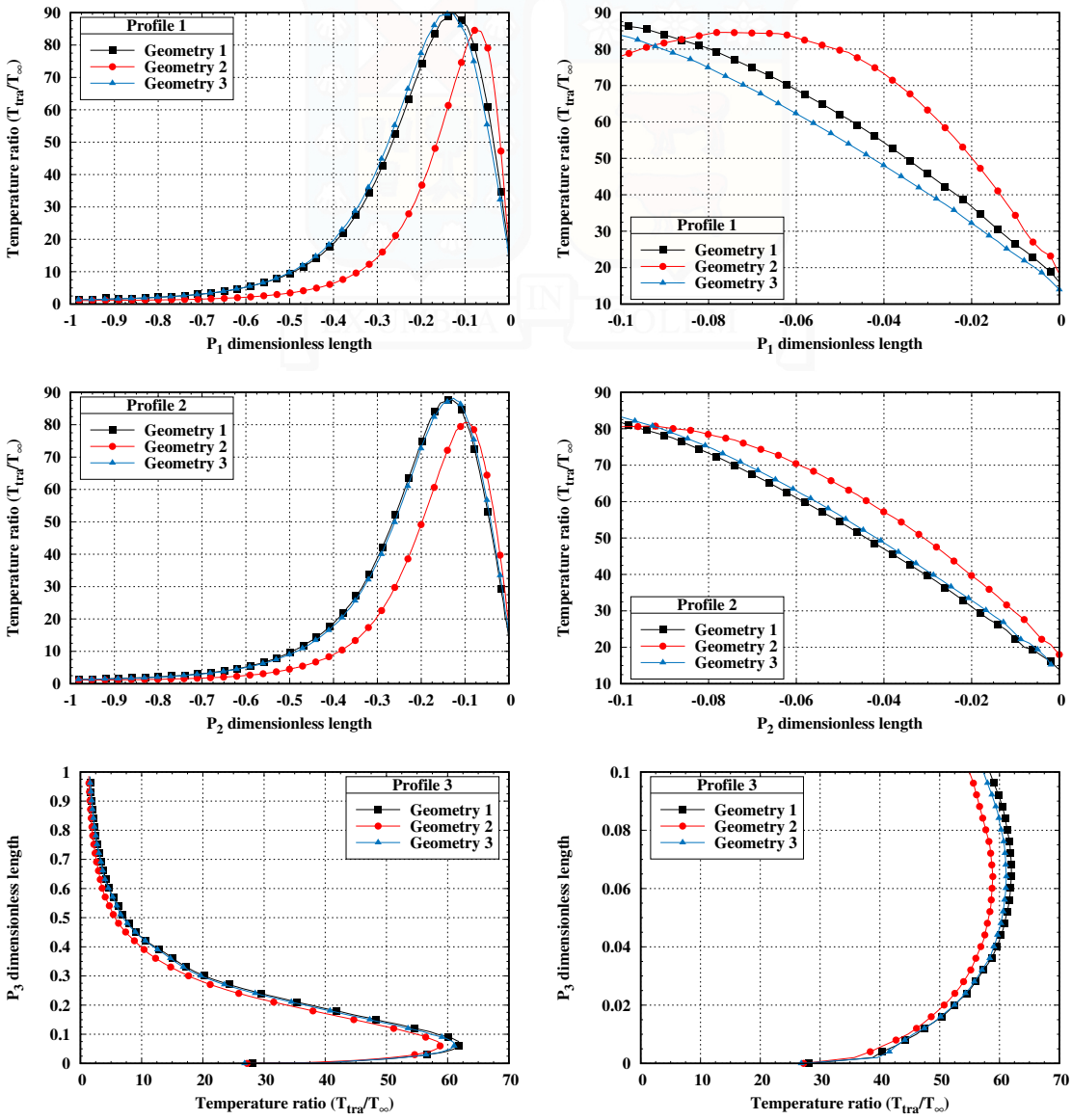

Figure 4.7: Translational temperature ratio along profiles normal to each geometry's surface. Left: Full computational domain. Right: Closer view of the flowfield near the spacecraft.

close to the IAD surfaces. The effect that Geometry 2 causes on the density ratio distribution is observed to extend 0.1 m upstream of the flexible shield. In contrast, the influence of Geometries 1 and 3 in the density flowfield occurs up 0.2 m upstream of the stagnation point.

The thickness of the high-density layer closer to the surface of the vehicles is also dependent on the shield's design. Geometries with a rounded nose and flat frontal surface, such as Geometry 1 and Geometry 2, have a thicker layer of high density over the shield. However, geometries with fully rounded aeroshells, like Geometry 3, have a thicker layer of high-density flow at the nose center that decreases gradually towards the edges.

Similarly to subsection 4.2.1 and subsection 4.2.2, Figure 4.9 shows the distribution of the mass density ratio along the three profiles normal to the IAD surface. The images on the left-hand side of Figure 4.9 provide a description of the mass density distribution over the complete extension of the profiles, i.e., from the inlet boundary condition to the IAD surface. The right-hand side of Figure 4.9 depicts the high-density layer formed over the flexible thermal protection system. According to this set of plots, similar behavior is observed between all profiles and geometries. Geometry 2 presented the lowest density ratio, reaching a maximum of 20 times the freestream density at the stagnation point (X0) and the surface midpoint (X1). In contrast, Geometry 1 reaches 26 and 30 times the freestream density at the stagnation point (X0) and the midpoint of the surface (X1), respectively. Geometry 3 is observed to have a maximum of 33 times the freestream density at the stagnation point (X0), the highest of all geometries under study, and a maximum of 30 times the atmospheric density at the midpoint of the frontal surface (X1). On the other hand, in profile P_3, is significantly decreased due to the flow expansion near the IAD shoulder. Furthermore, at the edge of the shoulder, there is little difference in the density ratio distribution between the geometries studied, and a maximum between 5.6 and 5.8 times the freestream density is observed at the IAD surface.

4.2.4 The pressure flowfield

The pressure determined by the dsmcFoam+ code is obtained using the following expression,

$$p = \frac{1}{3} nm\overline{\boldsymbol{c}'^2} = \frac{1}{3}\frac{\overline{N}F_N}{V_c}\frac{\sum_{i=1}^{N} m_i \boldsymbol{c}'^2}{N}, \tag{4.6}$$

where n is the local number density, m is the molecular mass, $\boldsymbol{c}'$ is the thermal velocity, V_c is the computational cell volume, and $\overline{N}$ and N are the average and total number of simulated particles within a given cell, respectively.

The pressure ratio contour levels calculated for each geometry are presented in Figure 4.10. Once again, the flowfield over the complete simulated domain is displayed on the right-hand side and the pressure contour close to the IAD coupled with 1U CubeSat is shown on the left-hand side. From Figure 4.10 it can

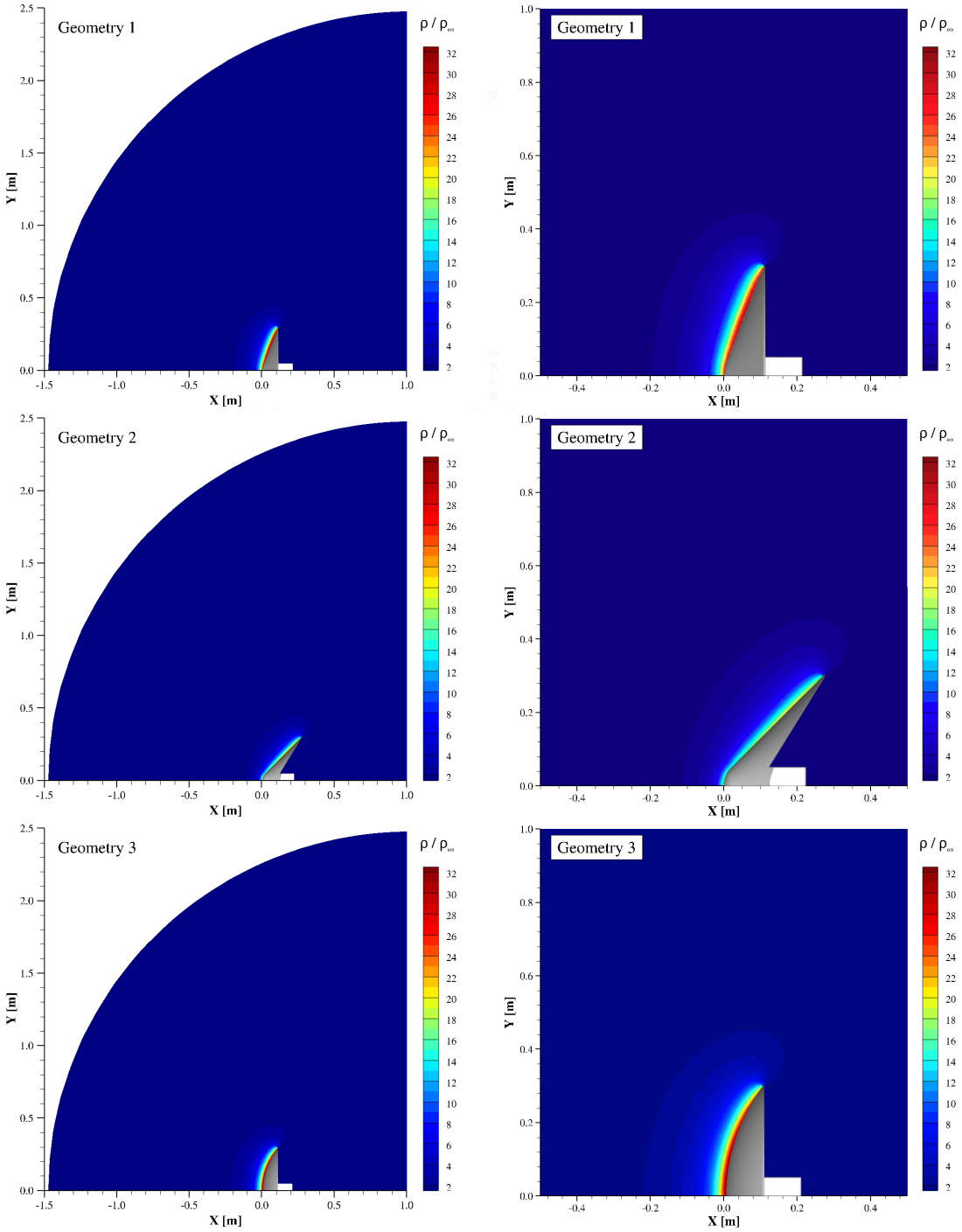

Figure 4.8: Mass density ratio contours around the simulated geometries. Left: Full computational domain. Right: Closer view of the flowfield near the spacecraft.

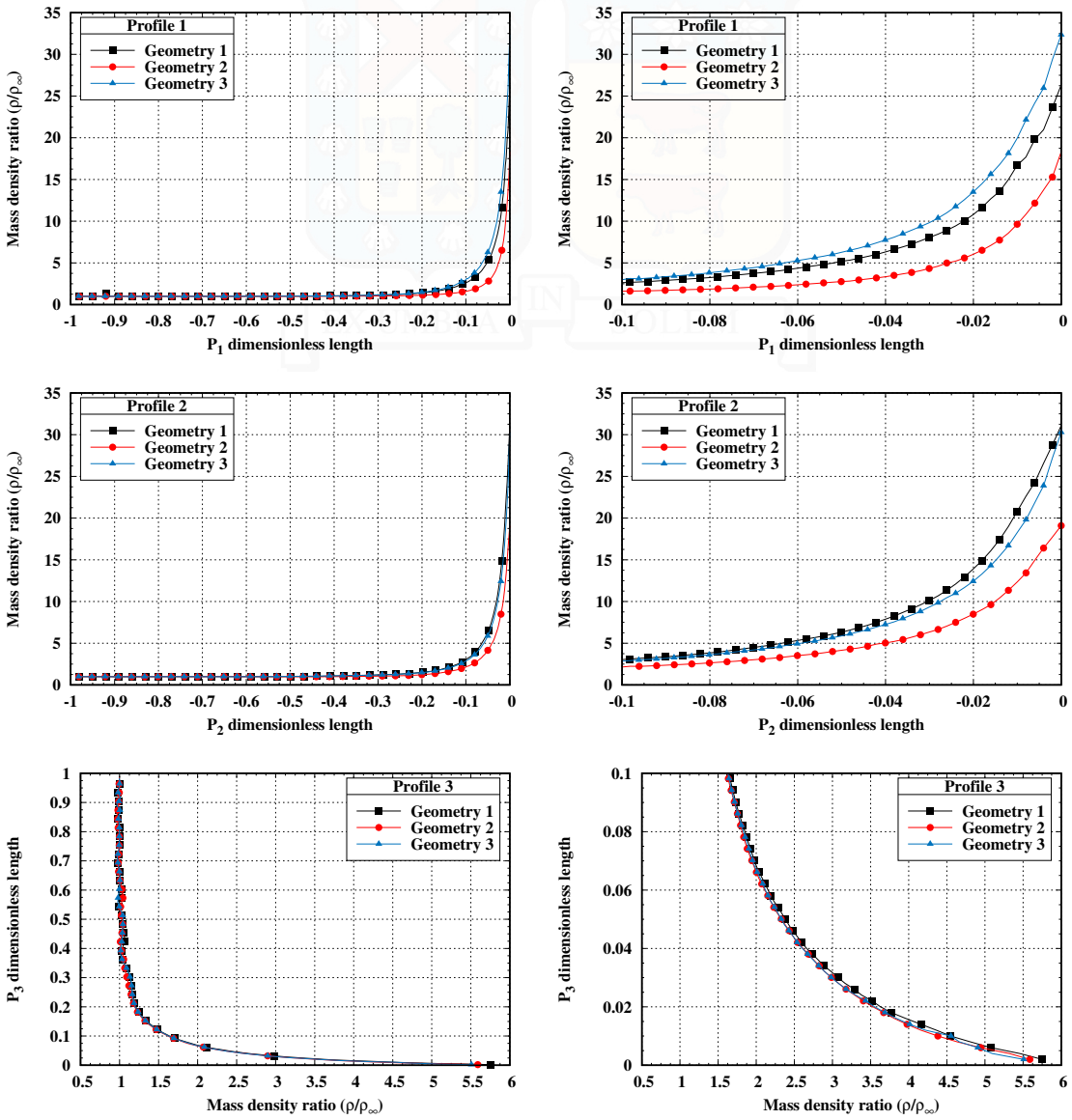

Figure 4.9: Mass density ratio along profiles normal to each geometry's surface. Left: Full computational domain. Right: Closer view of the flowfield near the spacecraft.

be observed that the pressure is low at the inlet and increases significantly as the flow moves towards the flexible aerodynamic decelerator. A high-pressure gradient can be observed in the region in front of each IAD vehicle, with the maximum pressure adjacent to the shield's surface. However, the contour maps show that the high-pressure region upstream of the surface dissipates at the IAD shoulder. The rapid decrease in pressure is associated with the flow expansion at the IAD shoulder, as particles transform stored energy in the form of pressure into kinetic energy. This behavior is consistent with the decrease in velocity and density observed in this region, as discussed in subsection 4.2.1 and subsection 4.2.3, respectively. Furthermore, it is noticed that Geometry 2 presented a lower pressure ratio compared to Geometry 1 and Geometry 3, that is, approximately 380 times the freestream pressure. In contrast, Geometry 1 and Geometry 3 show a maximum pressure ratio of approximately 480 times the freestream pressure.

Finally, Figure 4.11 shows the pressure distribution along three stations normal to the IAD surface. From this set of plots, it is observed that the pressure ratio is low at the inlet and increases significantly as the freestream molecules approach the IAD surface. Profiles P_1 and P_2 exhibit a similar pressure distribution throughout the complete extension of the profiles. For Geometry 1 and Geometry 3, profile P_1, a maximum pressure of 450 and 500 times the freestream pressure is observed at the stagnation point, respectively. However, Geometry 2 presented a maximum pressure of 350 times the freestream pressure in the same region. For profile P_2, the pressure ratio at the shield's midpoint surface of Geometry 2 increases to 400 times the freestream pressure, whereas Geometries 1 and 3 maintained values in a range between 450 and 500 times the atmospheric pressure. However, in profile P_3, the pressure ratio distribution of the geometries studied is almost identical, with all geometries reaching maximum values at the shoulder surface (X3) and decreasing towards the inlet boundary condition. In this profile, the maximum pressure ratio ranged from 200 to 220 times the atmospheric pressure, where Geometry 2 is associated with the lowest pressure field and Geometry 3 with the highest pressure field of all three geometries.

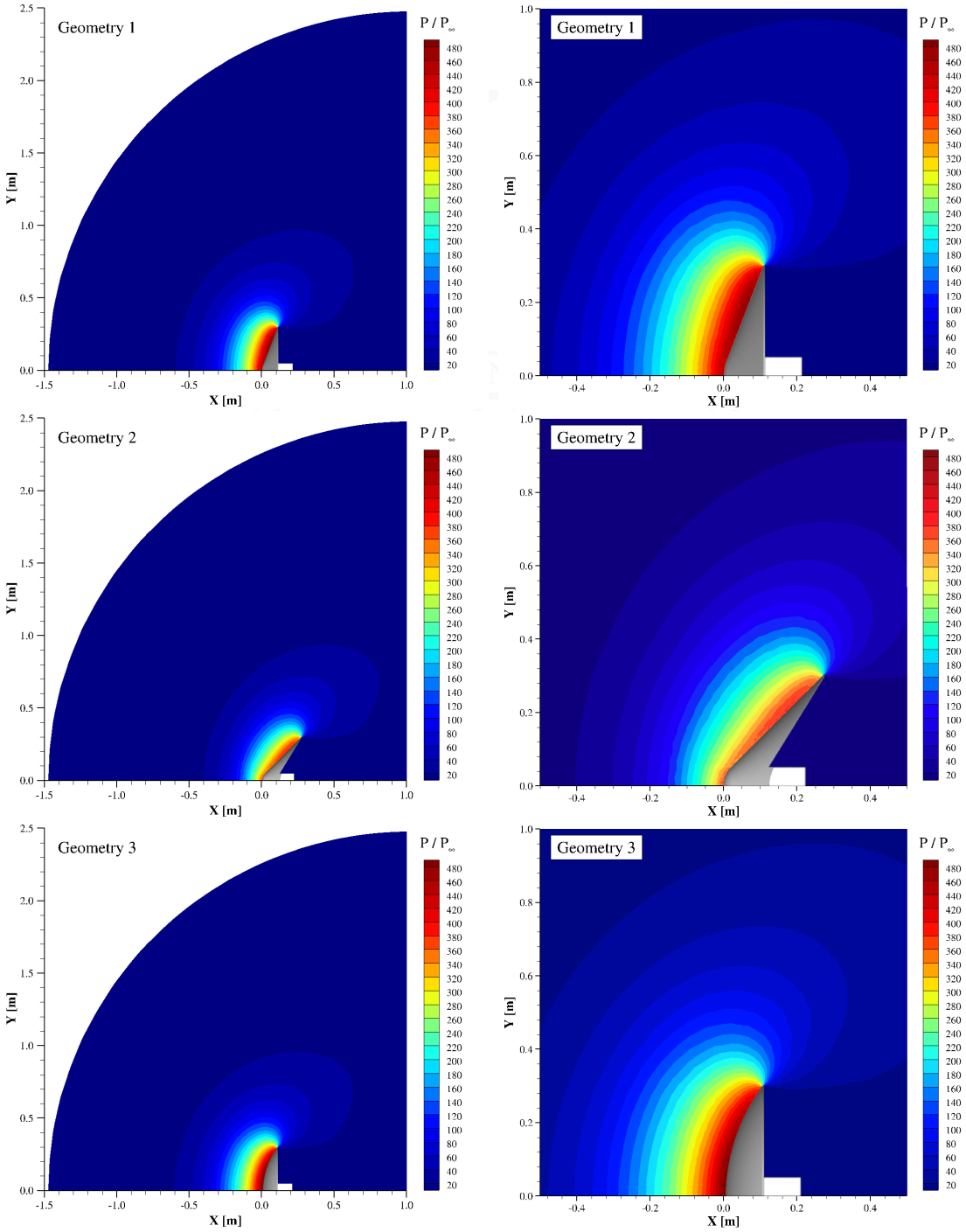

Figure 4.10: Pressure ratio contours around the simulated geometries. Left: Full computational domain. Right: Closer view of the flowfield near the spacecraft.

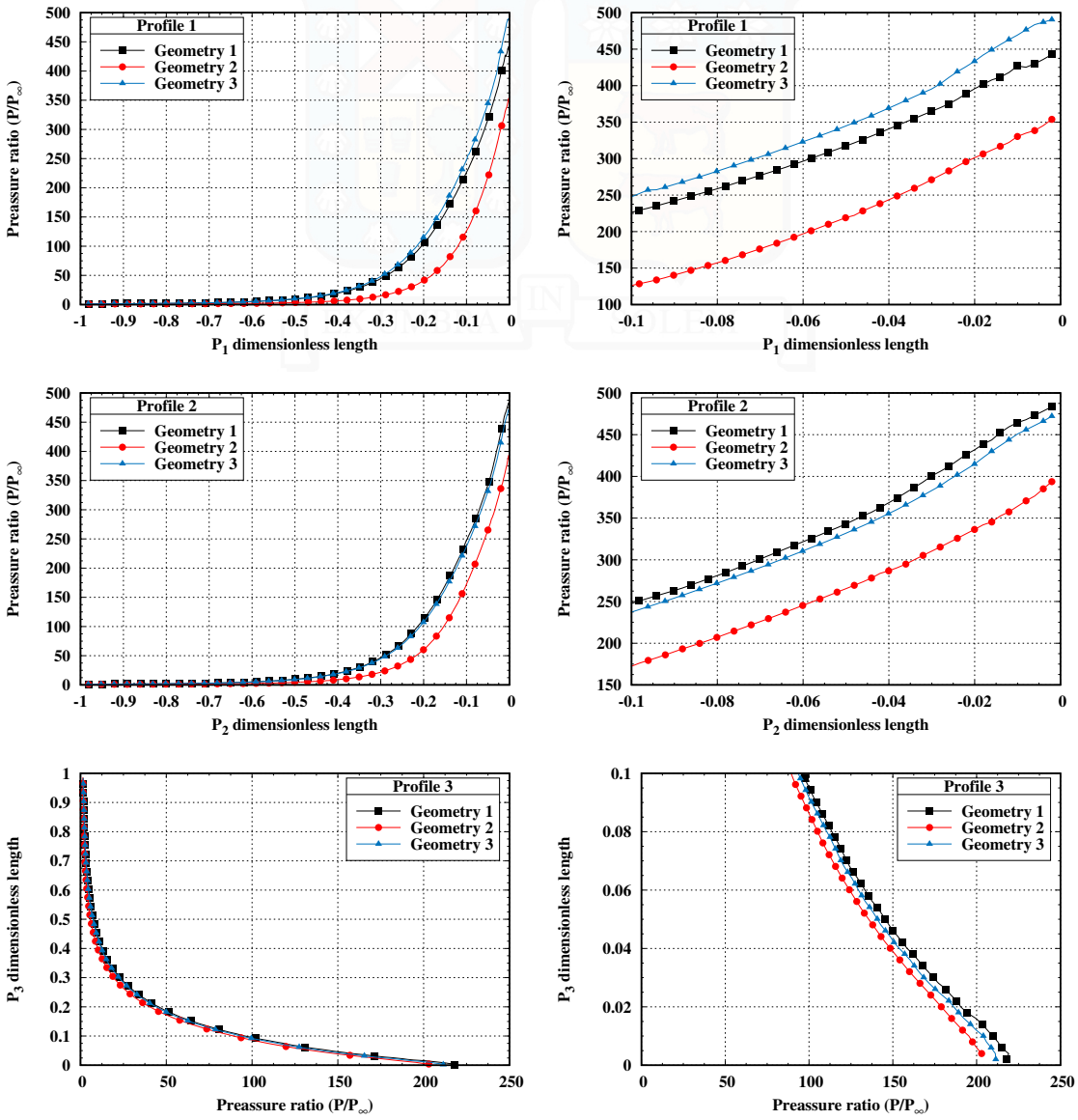

Figure 4.11: Pressure ratio along profiles normal to each geometry's surface. Left: Full computational domain. Right: Closer view of the flowfield near the spacecraft.

4.3 Surface properties

4.3.1 Surface heat transfer during reentry

The heat transfer coefficient (C_h) is used to characterize the rate of heat transfer between the particles and the IAD surface. The heat transfer coefficient is defined as

$$C_h = \frac{q_{wall}}{\frac{1}{2}\rho_\infty U_\infty^3}, \tag{4.7}$$

where the net heat flux (q_{wall}) to the surface is calculated by taking into account the energy of incident and reflected particles,

$$q_{wall} = q_i - q_r = \frac{F_N}{A\Delta t}\left\{\sum_{j=1}^{N}\left[\phi_j\right]_i - \sum_{j=1}^{N}\left[\phi_j\right]_r\right\}, \tag{4.8}$$

where F_N is the ratio of real molecules represented by a simulated molecule, A is the surface area, Δt is the time step, and N is the number of molecules that collide with the surface per unit area per unit time. The energy of each particle, with mass m and velocity c, is represented as the sum of its translational, rotational, and vibrational energies,

$$\phi_j = \frac{1}{2}m_j c_j^2 + (e_{\text{rot}})_j + (e_{\text{vib}})_j. \tag{4.9}$$

Figure 4.12 shows the heat transfer coefficient (C_h) contours over the IADs and CubeSat surfaces. The same contour levels are used for all geometries, where the C_h maximum, obtained for Geometry 2, is used as the reference value. According to Figure 4.12, significant differences in the heat transfer coefficient distribution are observed for the proposed IAD configurations. The highest heat transfer region is observed at the nose of each reentry vehicle; however, the area and intensity of this region vary depending on the forebody angle of the flexible thermal shield. Aerodynamic geometries, such as Geometry 2, presented a high heat transfer region at the nose tip with increased values of C_h when compared with those obtained for Geometry 1 and Geometry 3. At the nose tip, Geometry 1 exhibits a behavior similar to that of Geometry 2, where both geometries have a high heat transfer region restricted to the nose cone at the tip of the shield. Geometry 3 has the lowest maximum intensity of the three geometries analyzed, but its heat transfer is more evenly distributed over a larger surface area. Furthermore, over the shield surface, it is clearly observed that Geometry 1 and Geometry 3 exhibit a similar heat transfer coefficient distribution, i.e., high values at the nose with well-distributed C_h values over the shield surface. By changing the IAD geometry, it is possible to choose to distribute or concentrate the heat loads over the IAD surface, and the data obtained in this investigation may be used to determine the correct material to be employed at the IAD flexible shield and

structure.

In Figure 4.13, the heat transfer coefficient distribution along the nondimensional length of each IAD frontal and rear surfaces is shown. The length of the shield surface was normalized considering the total frontal surface length of each shield independently, defining $L_S = 0$ as the tip of the nose and $L_S = 1$ as the farthest end from the centerline in the front shoulder (X3) of each geometry, as shown in Figure 4.1.

Figure 4.13 corroborates that Geometry 2 has the highest value of C_h among all geometries studied, which are found from $L_S = 0$ to 0.03. However, the heat transfer in this geometry reduces significantly on the outer diameter of the nose cone, from $L_S = 0.03$ to $L_S = 0.175$. From this point to $L_S = 1.0$, the heat transfer coefficient over the surface is maintained at constant, with lower values when compared with Geometry 1 and Geometry 3. Furthermore, it is observed that Geometry 3 shows a gradual and slight decrease in heat transfer over the surface length, whereas Geometry 1 maintains a relatively constant value up to the shield's shoulder. Across all geometries under study, heat transfer near the shield's shoulder ($L_S = 1$) drops to negligible values. This phenomenon occurs because the flow expands near the shoulder of each shield, which reduces the amount and energy of particles colliding with the surface. For all geometries in analysis, it is observed that the heat transfer coefficient drops to insignificant levels behind the shield and over the payload, corroborating the effectiveness of IADs in reducing thermal loads for the reentry and recovery of CubeSats.

Finally, Table 4.4 shows the heat transfer coefficient of the maximum value ($C_{h,\max}$) and the total heat transfer ($\dot{Q}_s$), integrated over the entire surface of each reentry vehicle, including the payload. From this table, it is observed that Geometry 2 exhibits the most intense thermal loads, as evidenced by its higher values of $C_{h,\max}$ and $\dot{Q}_s$ compared to Geometries 1 and 3. Furthermore, the maximum value of the heat transfer coefficient of Geometry 2 is 7.5% and 14.4% higher than those computed for Geometry 1 and Geometry 3, respectively. The total heat transfer to the surface of Geometry 2 is 1.33% and 1.76% higher compared to Geometry 1 and Geometry 3, respectively. It is worth noting that Geometry 2 has a larger surface area due to its aerodynamic and elongated shape, which results in a higher total heat transfer, despite having the lowest C_h values over the IAD surface.

Table 4.4: Maximum heat transfer coefficient ($C_{h,\max}$) and total heat transfer ($\dot{Q}_s$) computed for each IAD geometry.

Parameter	Geometry 1	Geometry 2	Geometry 3
$C_{h,\max}$	0.90	0.97	0.84
$\dot{Q}_s$ (W)	8616	8731	8579

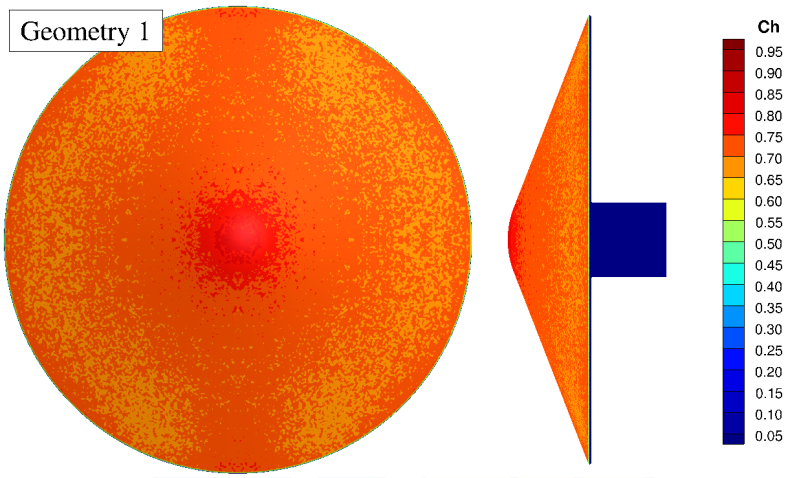

(a) Geometry 1 heat transfer coefficient (C_h).

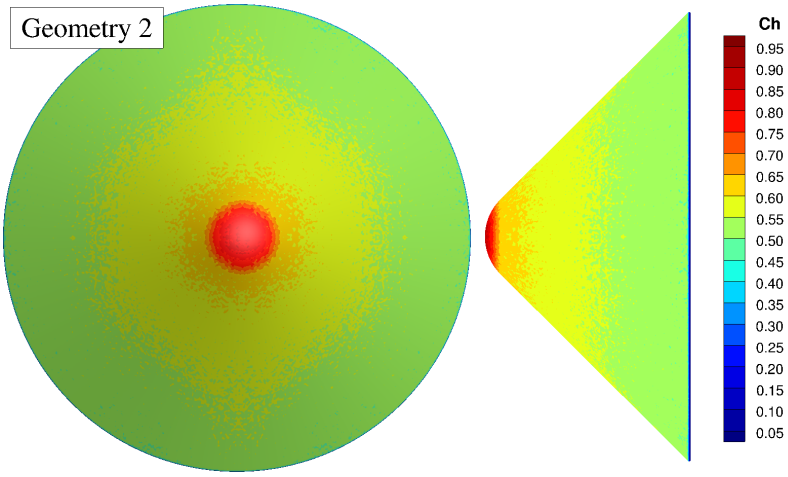

(b) Geometry 2 heat transfer coefficient (C_h).

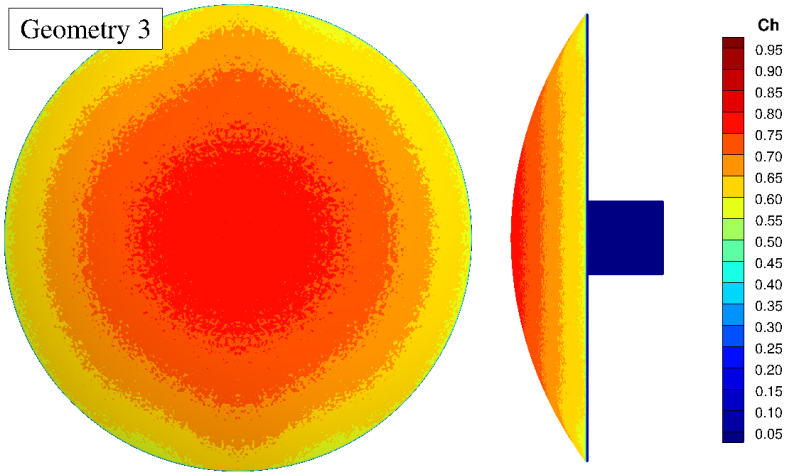

(c) Geometry 3 heat transfer coefficient (C_h).

Figure 4.12: Heat transfer coefficient (C_h) contours over the IADs surfaces.

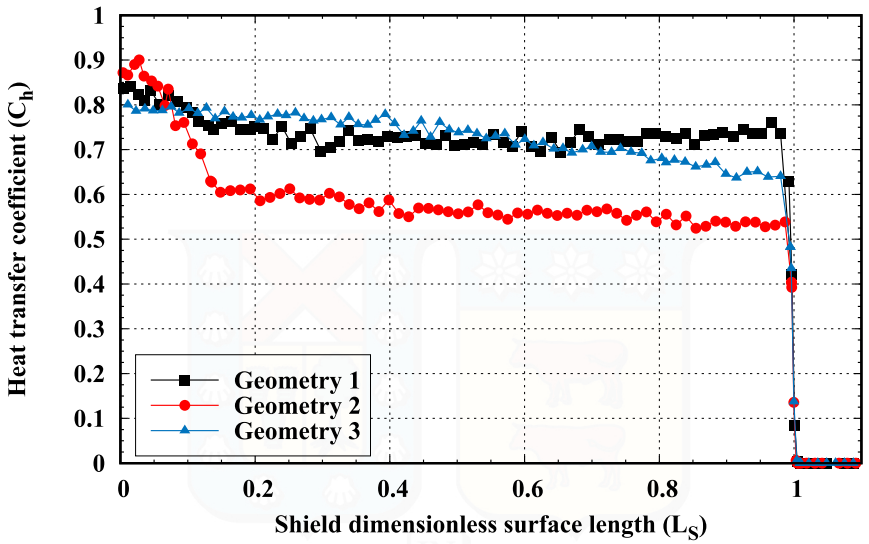

Figure 4.13: Heat transfer coefficient (C_h) distribution along the nondimensional length for each IAD surface.

4.3.2 Pressure on the reentry vehicles' surfaces

The pressure coefficient is defined as the difference between the pressure on the surface of the IAD (p_{wall}) and the freestream pressure (p_∞) normalized by the freestream dynamic pressure,

$$C_p = \frac{p_{\text{wall}} - p_\infty}{\frac{1}{2}\rho_\infty U_\infty^2}, \tag{4.10}$$

where the pressure on the surface p_{wall} is defined as the net momentum flow perpendicular to the surface as

$$p_{\text{wall}} = p_i - p_r = \frac{F_N}{A\Delta t}\sum_{j=1}^{N}\left\{\left[(mc_\perp)_j\right]_i - \left[(mc_\perp)_j\right]_r\right\}, \tag{4.11}$$

where $c_\perp$ represents the velocity component of the particle perpendicular to the surface, and the subscripts i and r indicate the incident and reflected particles, respectively. As mentioned in the previous section, F_N stands for the ratio of real molecules represented by a simulated molecule, A is the surface area, Δt is the time step, and N is the number of molecules that collide with the surface per unit area per unit time.

Figure 4.14 shows the pressure coefficient (C_p) contours over the IAD geometries. Similarly to the heat transfer coefficient analysis, the pressure contour levels are adjusted according to the maximum values obtained for Geometry 2. From this group of plots, it is noticed that all geometries exhibit a maximum value of C_p at the shield's nose, i.e., at the stagnation point. At this region, the particle's velocity is drastically reduced due to the IAD surface, resulting in a substantial increase in the normal momentum over the surface

and a higher pressure coefficient at this zone when compared to the rest of the shield. It is also observed that Geometry 1 and Geometry 2 exhibit a well-defined maximum contour level for the pressure coefficient, and that it is distributed in a small region when compared to the cross-section area of the flexible shield. On the contrary, Geometry 3 presented a maximum C_p contour level that covers a greater proportion of the shield's cross-section area, indicating a higher normal momentum in the IAD forebody surface.

Still referring to Figure 4.14, a significant difference in the pressure coefficient distribution over the IAD geometries surfaces can be noticed. Geometry 2 showed the most drastic reduction in C_p when compared with Geometry 1 and 3, where an average value of 1.17 is observed at the frontal surface. The pressure coefficient for Geometry 1 maintained constant values with an average of $C_p = 1.75$, which is significantly higher than those observed for Geometry 2. Geometry 3 shows a gradual and smooth reduction on C_p from the nose to the IAD shoulder. The pressure coefficient obtained for Geometry 3 is lower than those found for Geometry 1 and higher than those of Geometry 2 at the shield's shoulder.

Figure 4.15 shows the pressure coefficient distribution over the nondimensional surface length (L_S) for the three geometries considered in the present investigation. In the dimensionless surface length, $L_S = 0$ corresponds to the stagnation point (X0) and $L_S = 1$ corresponds to the IAD shoulder (X3) of the respective geometry, as shown in Figure 4.1.

According to Figure 4.15, the three geometries under investigation presented $C_p = 2$ at the stagnation point, $L_S = 0$. However, there are noticeable differences in the pressure coefficient along the surface of each geometry. Geometry 1 shows the least variation in pressure along its surface, with the pressure coefficient dropping from $C_p = 2$ to $C_p \approx 1.75$ between the nose and the shoulder, with an average value of 1.75. Geometry 2 exhibits a significant decrease in the pressure coefficient from $C_p = 2$ to $C_p = 1.13$, from $L_S = 0$ to $L_S = 0.13$, respectively. From $L_S = 0.13$ to $L_S = 1.0$, the pressure coefficient maintained a constant value of 1.1 with a slight decrease as the particles approaches the IAD shoulder, before the flow expansion at $L_S = 1.0$. As observed in the plot, the fully rounded forebody structure of Geometry 3 resulted in a gradual reduction of the pressure coefficient, with an average pressure coefficient value of $C_p \approx 1.69$. It is worth noting that all geometries analyzed presented pressure coefficient drops to values close to zero in the region between the beginning of the shoulder and the farthest point from the geometric center line of the IAD at $L_S = 1$. This effect occurs due to the flow expansion over the shoulder of each IAD, which reduces the effect of molecular collisions with the IAD's rear surface. In the rear section of the IAD, a significant reduction in the pressure coefficient at the CubeSat surface is noticed, reaching near zero values at the wake.

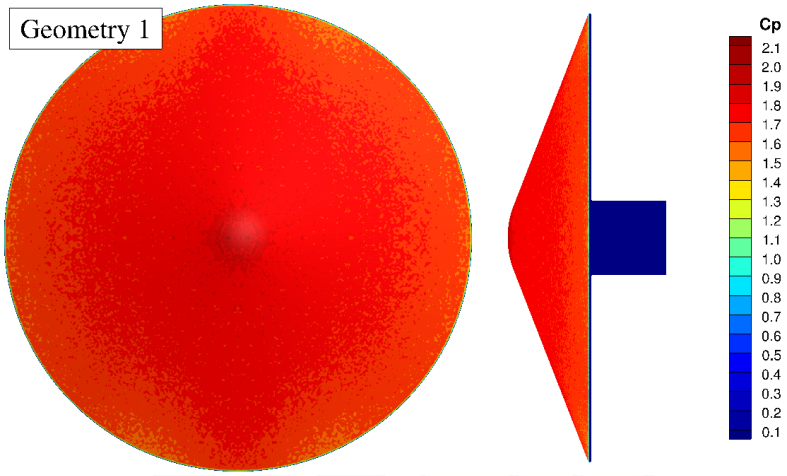

(a) Geometry 1 pressure coefficient (C_p).

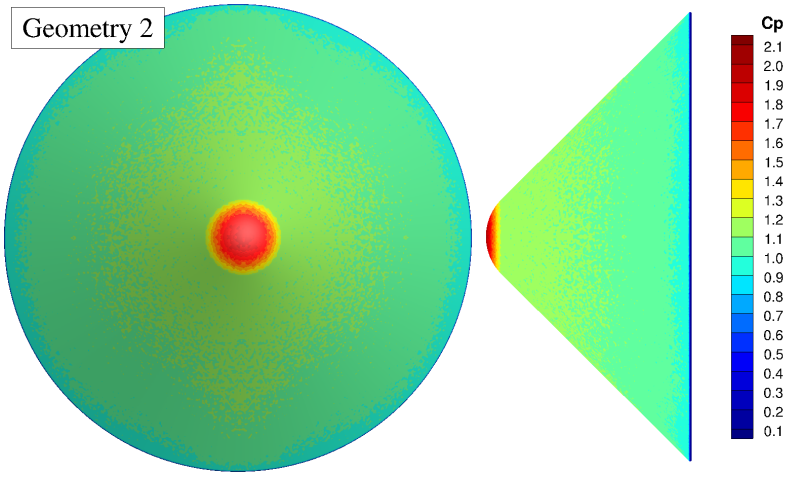

(b) Geometry 2 pressure coefficient (C_p).

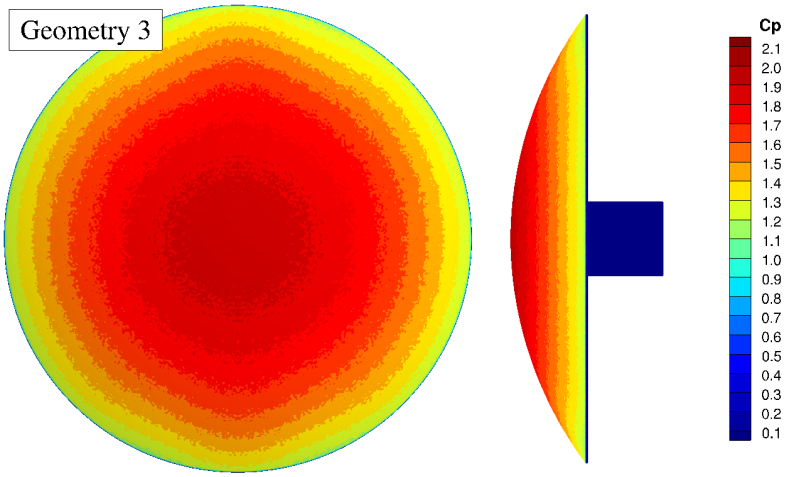

(c) Geometry 3 pressure coefficient (C_p).

Figure 4.14: Pressure coefficient (C_p) contours over the IADs surfaces.

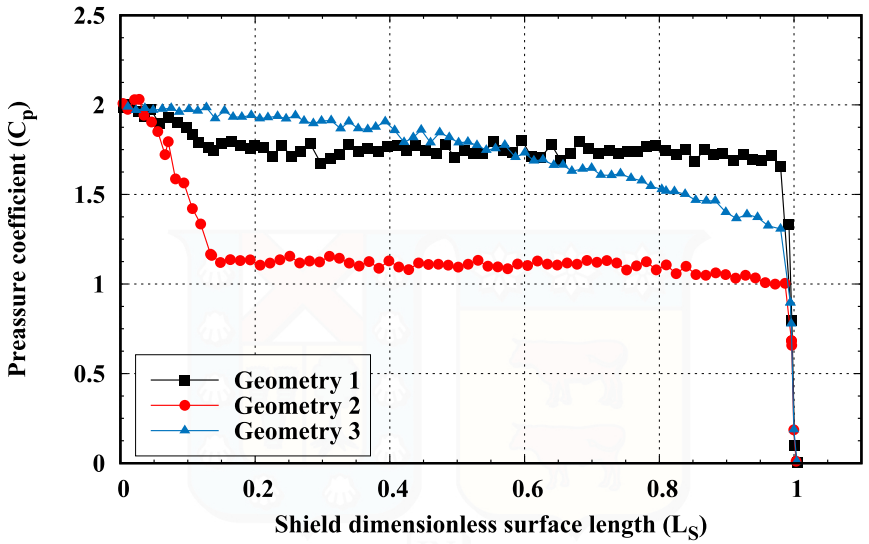

Figure 4.15: Pressure coefficient (C_p) distribution along the nondimensional length of each IAD surface.

4.3.3 Skin friction coefficient

The skin friction coefficient (C_f) is obtained by normalizing the shear stress (τ_{wall}) on the surface with the dynamic pressure of the freestream flow, that is,

$$C_f = \frac{\tau_{\text{wall}}}{\frac{1}{2}\rho_\infty U_\infty^2}, \tag{4.12}$$

where the shear stress on the surface (τ_{wall}) of the spacecraft is calculated by considering the tangential component ($c_\parallel$) of the velocity of the incident and reflected particles. Hence, the net tangential momentum flow can be expressed as

$$\tau_{\text{wall}} = \tau_i - \tau_r = \frac{F_N}{A\Delta t}\sum_{j=1}^{N}\left\{\left[(mc_\parallel)_j\right]_i - \left[(mc_\parallel)_j\right]_r\right\}. \tag{4.13}$$

The diffuse gas-surface interaction model implies that the average tangential momentum of reflected particles is equal to zero, since there is an equal probability for positive and negative values of tangential momentum in reflected particles. Thus, the shear stress on the IAD surface can be calculated as

$$\tau_{\text{wall}} = \tau_i = \frac{F_N}{A\Delta t}\sum_{j=1}^{N}\left\{\left[(mc_\parallel)_j\right]_i\right\}. \tag{4.14}$$

Figure 4.16 shows the skin friction coefficient (C_f) contours over the IADs geometries coupled with 1U CubeSat. All surface contour plots have the same contour levels, which were based on the maximum skin friction value computed for Geometry 2. From Figure 4.16, it is observed that all geometries have a

low skin friction region at the nose region and areas of higher C_f values near the shoulder of each IAD configuration. At 0° angle of attack, the low values of the skin friction coefficient at the nose of each geometry are attributed to the angle between the incident particles and the surface, which results in a lower tangential velocity component and hence a lower momentum flow in this direction. Conversely, the IAD disturbance in the flow causes the particles to follow a path parallel to the surface in the forebody region, increasing the tangential momentum to the flexible aeroshell of each geometry.

Differences in the form factor of the geometries' forebody change the interaction between the IAD and incoming freestream. An aerodynamic shape, such as Geometry 2, with a shield angle of 45°, has a smaller region of low-speed flow over the shield, and high-speed flow is achieved over most of the flexible shield up to the shoulder. The increase in the velocity over the surface causes a significant augmentation of the skin friction coefficient, as can be observed in the C_f contours, Geometry 2. On the contrary, Geometry 1, with a shield angle of 68.821°, shows significantly lower C_f over the IAD surface and maintains a relatively uniform distribution up to the beginning of the shoulder. In this regard, the blunt shape of Geometry 3 results in a larger area of low C_f at the nose; however, a rapid increase from the IAD nose to the shoulder is noticed. Similarly to the heat transfer and pressure coefficients, the skin friction coefficient at the shield shoulder falls to values close to zero, maintaining negligible magnitude on the rear surface of the shield and on the payload.

The distribution of the skin friction coefficient over the IAD geometries is shown in Figure 4.17. As described in the subsection 4.3.1 and subsection 4.3.2, $L_S = 0$ corresponds to the nose tip ($X0$) and $L_S = 1$ to the farthest point from the centerline on the shield shoulder ($X3$).

According to Figure 4.17, it is clear to notice the influence of the IAD surface angle on the skin friction coefficient distribution. The three geometries considered in the present investigation presented very low C_f values at the stagnation point ($L_S = 0$), as a consequence of the particle's velocity decrease at this region. As the flow particles move over the IAD, the change on the inflatable aerodynamic decelerator surface angle causes particles to move faster or slower, towards the geometry shoulder. From $L_S = 0$ to $L_S = 0.15$, it is observed a steep increase on C_f for geometry 1 and 2. After $L_S = 0.15$, the skin friction coefficient remains constant, with a slight increase as the flow approaches the IAD shoulder. Once the flow expands over the shoulders regions, C_f decreases to almost zero values. Due to its rounded surface, it is clearly noticed that Geometry 3 presented a linear increase in the skin friction coefficient distribution from the stagnation point to the IAD shoulder.

From the three IAD geometries considered in the present investigation, Geometry 2 exhibited the most pronounced increase in skin friction coefficient, reaching a maximum value 0.8 between the nose and the shoulder. This value is significantly higher than the shear stress experienced by Geometry 1 and Geometry 3 in the same zone. Geometry 1 has an approximate skin friction coefficient of 0.45 in this region, while Geometry 3 gradually increases within the range of $0.1 < C_f < 0.2$.

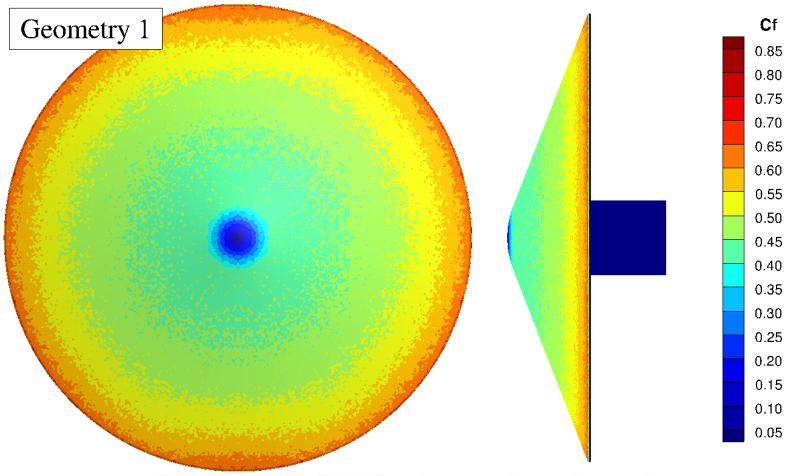

(a) Geometry 1 skin friction coefficient (C_f).

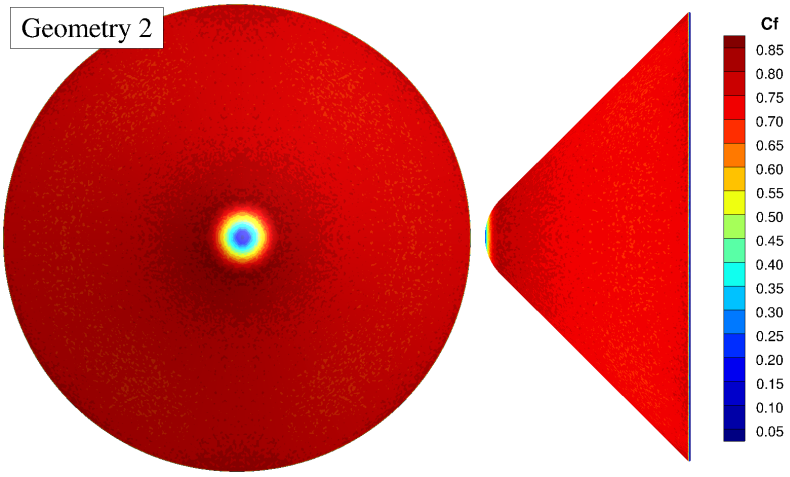

(b) Geometry 1 skin friction coefficient (C_f).

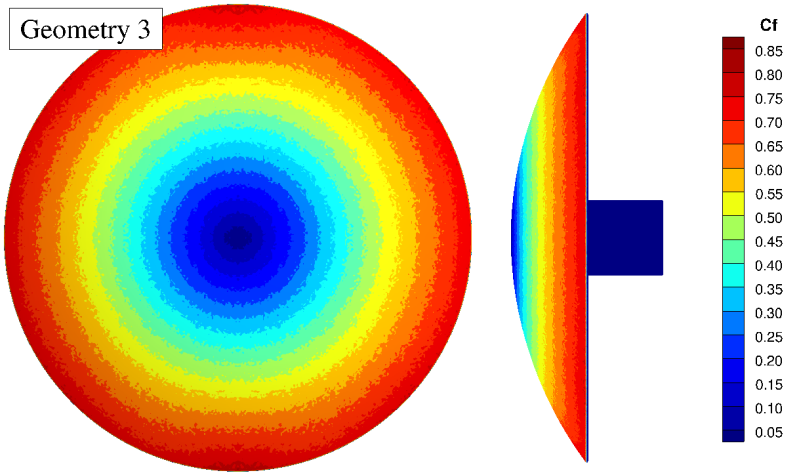

(c) Geometry 1 skin friction coefficient (C_f).

Figure 4.16: Skin friction coefficient (C_f) contours over the IADs surface.

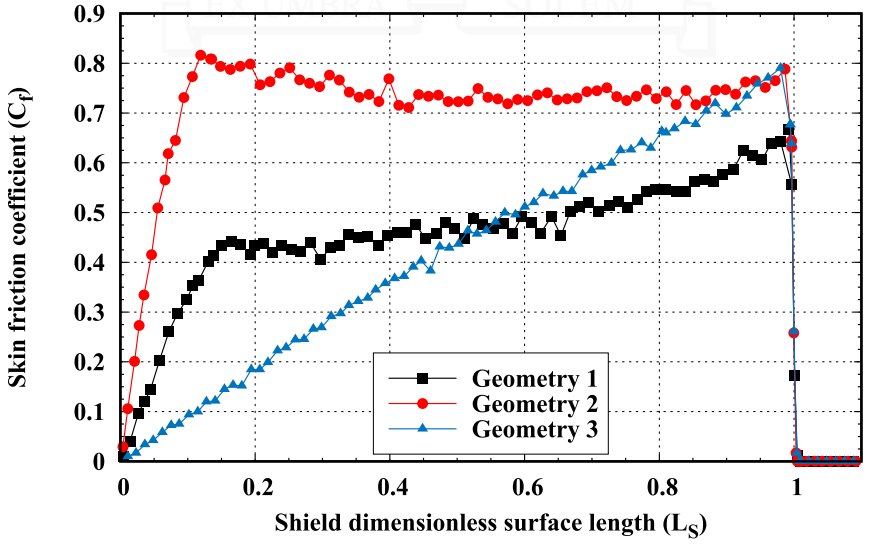

Figure 4.17: Skin friction coefficient (C_f) distribution along the nondimensional length over the IAD surfaces.

4.4 Aerodynamic forces

The aerodynamic forces experienced by each IAD geometry considered in this investigation are presented in Table 4.5. Due to the axial symmetry of the geometries, the lift and normal forces can be considered negligible, and the respective coefficients are assumed to be zero ($C_N = C_L = 0$). In addition, 0° the angle of attack of implies that the axial force and the drag force acting on the IAD surface are equivalent, $C_A = C_D$. In doing so, the drag coefficient (C_D) is calculated as follows:

$$C_D = \frac{F_D}{\frac{1}{2}\rho_\infty U_\infty^2 A}, \tag{4.15}$$

where A corresponds to the cross-sectional area of each IAD.

From Table 4.5, it is observed that Geometry 1 has the highest drag coefficient among all geometries analyzed. Since Geometry 3 and Geometry 1 generate similar upstream flow disturbance, similar C_D values are found for these geometries. According to the computed data, Geometry 2 is considered the most aerodynamically efficient geometry and presented the lowest values of drag force and drag coefficient.

The ballistic coefficient (BC) is calculated considering the target mass of a 2U CubeSat, the reference cross-section area, and the drag coefficient associated with each geometry, as follows:

$$\text{BC} = \frac{m}{C_D\, A}. \tag{4.16}$$

According to Table 4.5, it is observed that Geometry 2 presented the highest BC among the geometries considered in this investigation. Furthermore, the BC values calculated for Geometry 1 and Geometry 3 shows that these geometries have better mass-to-drag proportion.

Table 4.5: Aerodynamic forces during reentry.

Parameter	Geometry 1	Geometry 2	Geometry 3
F_D (N)	3.06	2.91	3.02
C_D	1.90	1.81	1.87
BC	7.46	7.84	7.55

5 | Conclusions and future work

In this investigation, the dsmcFoam+ code software was used to assess the effects of three distinct IAD forebody geometries designed for CubeSat applications on the flow, surface properties, and aerodynamic forces experienced during reentry. The geometries under study are similar in shape to form factors used in previous and current IAD projects. The investigation focused on the initial stages of atmospheric reentry, where the simulation conditions involved high-speed nonreacting flow in the transitional regime.

A validation and verification process was carried out to assess the accuracy and sensibility of the dsmcFoam+ solver. The validation process was based on previous numerical work by Moss *et al.* on the Orion crew module and the IRVE spacecraft. Excellent agreement between the calculated and reference values is observed for all validation simulations. One of the validation simulations was used as a standard case from which the key simulation parameters for the accuracy of the DSMC method are deviated. According to the results of the verification process, the flow solutions calculated can be considered to be independent of small variations in the different factors tested. These results validate the application of the dsmcFoam+ code for the atmospheric reentry simulation of blunt and cone geometries under high-speed nonreacting rarefied conditions.

The main body of work of this research was concerned with the study of three CubeSat based IAD geometries. All geometries under study have a shield radius of 0.3 m and each is characterized by its respective aeroshell shape; 68.8°, 45° and fully rounded, respectively. All geometries are simulated at an altitude of 105 km and under conditions similar to those experienced by these kinds of spacecraft during upper reentry. The results presented demonstrate that all three geometries are effective in reducing the thermal and mechanical loads on the CubeSat payload during reentry. However, it was observed that all flowfields analyzed are highly dependent on the IAD forebody geometry. Blunt geometries were observed to have a strong diffuse shock wave away from the surface of the shield. On the contrary, aerodynamic shapes are associated with a less strong shock wave closer to the body of the vehicle, with increased temperature and lower pressure and density fields. These differences subsided closer to the edges of the main shoulder, in the flow expansion region, where similar macroscopic quantity magnitudes and flow behavior were observed between the different geometries being studied. Behind the shield and around the CubeSat, a low temperature,

low speed flow region is formed, protecting the payload from the harsh reentry conditions. This flow region is larger in aerodynamic elongated shapes, but these vehicles are associated with a higher gas temperature near the front surface of the shield. No recirculation zone behind the shield was observed in any of the IAD concepts under study.

Moreover, IAD forebody geometry was found to have a significant influence on the distribution and magnitude of the heat and momentum fluxes to the surface. According to the results, the heat transfer coefficient was observed to be high and concentrated at the IAD nose region. Geometry 2 exhibited the highest maximum heat transfer coefficient and total heat transfer at the IAD nose when compared with Geometry 1 and 3. However, it was also noticed that Geometry 2 had the lowest heat transfer coefficient over the middle segment of the flexible heat shield. The data obtained in this investigation indicates that this type of geometry has higher design requirements at the tip of the spacecraft, but would be more favorable for the flexible thermal protection material over the IAD. All three geometries were observed to have a maximum pressure coefficient at the shield nose. However, aerodynamic geometries were found to have lower pressures on the IAD surface, which could reduce aeroshell deformation and structural design requirements. Each geometry exhibited a minimum skin friction coefficient in the shield nose region; however, it increases significantly along the surface depending on the IAD geometry angle. For fully rounded geometries, a smooth increase in skin friction coefficient was observed. All aerothermal coefficients fall to negligible values in the rear section of the shield and on the CubeSat surface, further demonstrating the effectiveness of IAD devices in reducing thermal and mechanical loads on the payload. Finally, Geometry 2 presented the lowest drag coefficient and the highest ballistic coefficient of the three geometries analyzed. In contrast, Geometry 1 demonstrated the highest drag coefficient and a better mass-to-drag proportion, implying that blunt geometries have better deceleration and performance for deorbit applications.

Future work will be dedicated to the analysis of the three geometries at different altitudes of descent during the reentry process. Future projects also consider investigations assessing the effect of chemical reactions in the flow for different forebody geometries and altitudes.

Bibliography

[1] Gil Denis, Didier Alary, Xavier Pasco, Nathalie Pisot, Delphine Texier, and Sandrine Toulza. From new space to big space: How commercial space dream is becoming a reality. *Acta Astronautica*, 166:431–443, February 2020. 1, 1

[2] Martin N. Sweeting. Modern Small Satellites-Changing the Economics of Space. *Proceedings of the IEEE*, 106(3):343–361, 2018. 1, 1

[3] Markets and Markets. Nanosatellite and Microsatellite Market. 1

[4] Robyn M. Millan, Rudolf von Steiger, Meir Ariel, Sergey Bartalev, Maurice Borgeaud, Stefano Campagnola, Julie C. Castillo-Rogez, René Fléron, Volker Gass, Anna Gregorio, David M. Klumpar, Bhavya Lal, Malcolm Macdonald, Jong Uk Park, V. Sambasiva Rao, Klaus Schilling, Graeme Stephens, Alan M. Title, and Ji Wu. Small satellites for space science: A COSPAR scientific roadmap. *Advances in Space Research*, 64(8):1466–1517, 2019. 1

[5] Jason Crusan and Carol Galica. NASA's CubeSat Launch Initiative: Enabling broad access to space. *Acta Astronautica*, 157:51–60, September 2019. 1

[6] California Polytechnic State University. Cubesat Design Specification Rev 14.1. Technical report, The CubeSat Program, Cal Poly SLO, February 2022. (document), 1, 1.1

[7] Thyrso Villela, Cesar A. Costa, Alessandra M. Brandão, Fernando T. Bueno, and Rodrigo Leonardi. Towards the thousandth CubeSat: A statistical overview. *International Journal of Aerospace Engineering*, 2019, 2019. (document), 1, 1, 1.3

[8] National Academies of Sciences, Engineering, and Medicine. *Achieving Science with CubeSats*. National Academies Press, Washington, D.C., oct 2016. 1

[9] Armen Poghosyan and Alessandro Golkar. CubeSat evolution: Analyzing CubeSat capabilities for conducting science missions. *Progress in Aerospace Sciences*, 88:59–83, November 2017. 1

[10] Erik Kulu. Nanosats database. (document), 1, 1.2

[11] Loïs Miraux, Andrew Ross Wilson, and Guillermo J. Dominguez Calabuig. Environmental sustainability of future proposed space activities. *Acta Astronautica*, 200:329–346, June 2022. 1

[12] Carmen Pardini and Luciano Anselmo. Evaluating the impact of space activities in low earth orbit. *Acta Astronautica*, 184:11–22, November 2021. 1, 1

[13] Heiner Klinkrad. *Orbital Debris and Sustainability of Space Operations*, pages 1145–1174. Springer New York, New York, NY, 2013. 1

[14] Giacomo Curzi, Dario Modenini, and Paolo Tortora. Large constellations of small satellites: A survey of near future challenges and missions. *Aerospace*, 7(9), 2020. 1

[15] Joseph R. Kopacz, Roman Herschitz, and Jason Roney. Small satellites an overview and assessment. *Acta Astronautica*, 170:93–105, January 2020. 1

[16] Jonathan C. McDowell. The Low Earth Orbit Satellite Population and Impacts of the SpaceX Starlink Constellation. *The Astrophysical Journal*, 892(2):L36, 2020. 1

[17] N. H. Crisp, P. C.E. Roberts, S. Livadiotti, V. T.A. Oiko, S. Edmondson, S. J. Haigh, C. Huyton, L. A. Sinpetru, K. L. Smith, S. D. Worrall, J. Becedas, R. M. Domínguez, D. González, V. Hanessian, A. Mølgaard, J. Nielsen, M. Bisgaard, Y. A. Chan, S. Fasoulas, G. H. Herdrich, F. Romano, C. Traub, D. García-Almiñana, S. Rodríguez-Donaire, M. Sureda, D. Kataria, R. Outlaw, B. Belkouchi, A. Conte, J. S. Perez, R. Villain, B. Heißerer, and A. Schwalber. The benefits of very low earth orbit for earth observation missions. *Progress in Aerospace Sciences*, 117, April 2020. 1

[18] W. J. Pang, B. Bo, X. Meng, X. Z. Yu, J. Guo, and J. Zhou. Boom of the cubesat: A statistic survey of cubsats launch in 2003-2015. *Proceedings of the International Astronautical Congress, IAC*, 0:2–7, September 2016. 1

[19] Jhonathan O. Murcia Piñeros, Walter Abrahão dos Santos, and Antônio F.B.A. Prado. Analysis of the orbit lifetime of CubeSats in low Earth orbits including periodic variation in drag due to attitude motion. *Advances in Space Research*, 67(2):902–918, 2021. 1

[20] Chris Ostrom and John Opiela. Orbital debris mitigation and cubesats. In *8th European Conference on Space Debris*, volume 8. ESA Space Debris Office, 04 2021. 1

[21] Donald J. Kessler, Nicholas L. Johnson, J. C. Liou, and Mark Matney. The Kessler Syndrome: Implications to future space operations. *Advances in the Astronautical Sciences*, 137:47–61, 2010. 1

[22] Joseph N. Pelton. The Space Debris Threat and the Kessler Syndrome. *SpringerBriefs in Space Development*, pages 17–23, 2013. 1

[23] National and Space National Administration. Process for Limiting Orbital Debris. Technical report, NASA-STD-8719.14C, February 2019. 1

[24] Fcc adopts new '5-year rule' for deorbiting satellites, Sep 2022. 1

[25] Valerio Carandente and Raffaele Savino. New Concepts of Deployable De-Orbit and Re-Entry Systems for CubeSat Miniaturized Satellites. *Recent Patents on Engineering*, 8(1):2–12, 2014. (document), 1, 1.1, 1.3, 1.20, 4.1

[26] Alan Cassell, Neil Cheatwood, Steven Hughes, Cole Kazemba, and Gregory Swanson. Deployable Entry Vehicles for Future Science and Exploration Missions. *Bulletin of the AAS*, 53(4), mar 2021. 1, 1.1, 1.1, 1.1, 1.1

[27] Joseph A. del Corso, F. McNeil Cheatwood, Walter E. Bruce, Stephen J. Hughes, and Anthony M. Calomino. Advanced high-temperature flexible TPS for inflatable aerodynamic decelerators. *21st AIAA Aerodynamic Decelerator Systems Technology Conference and Seminar 2011*, pages 1–23, May 2011. 1.1

[28] Stephen Hughes, Joanne Ware, Joseph Del Corso, and Rafael Lugo. Deployable Aeroshell Flexible Thermal Protection System Testing. In *20th AIAA Aerodynamic Decelerator Systems Technology Conference and Seminar*, AIAA 2011-2510, pages 1–21, Reston, Virigina, May 2009. American Institute of Aeronautics and Astronautics. 1.1

[29] Joseph A. Del Corso, Walter E. Bruce III, Stephen J. Hughes, John A. Dec, Marc D. Rezin, Mary Ann, B. Meador, Haiquan Guo, Douglas G. Fletcher, Anthony M. Calomino, and F. McNeil Cheatwood. Flexible Thermal Protection System Development for Hypersonic Inflatable Aerodynamic Decelerators. In *9Th International Planetary Probe Workshop*, June 2012. 1.1, 1.1

[30] Max Braun, Paul Bruce, and Errikos Levis. Strategies to utilize advanced heat shield technology for high-payload mars atmospheric entry missions. *Acta Astronautica*, 136:22–33, November 2016 2017. 1.1

[31] Rui Wu, Peter C.E. Roberts, Constantinos Soutis, and Carl Diver. Flexible heat shields deployed by centrifugal force. *Acta Astronautica*, pages 78–87, June 2018. 1.1, 1.3

[32] Brandon Smith, Alan Cassell, Carl Kruger, Ethiraj Venkatapathy, Cole Kazemba, and Kyle Simonis. Nano-ADEPT: An entry system for secondary payloads. *IEEE Aerospace Conference Proceedings*, 2015-June, 2015. 1.1, 1.3

[33] Alan M. Cassell, Paul F. Wercinski, Brandon P. Smith, Bryan C. Yount, Shakib M. Ghassemieh, Owen S. Nishioka, Carl E. Kruger, Chad A. Brivkalns, Alberto Makino, Shang C. Wu, Nghia N. Mai, Ryan D. McDaniel, Ali Guarneros-Luna, Joseph D. Williams, Dzung T. Hoang, Richard L. Rowan, Soumyo Dutta, Ashley M. Korzun, Justin S. Green, Jake A. Tynis, and Chris Karlgaard. Adept sounding rocket one flight test overview. *AIAA Aviation 2019 Forum*, pages 1–15, June 2019. 1.1, 1.3, 1.23b

[34] Valerio Carandente, Raffaele Savino, Vera D'Oriano, and Raimondo Fortezza. A Study on Earth Re-entry Capsules with Deployable Aerobrakes for Recoverable Microgravity Experiments. *Microgravity Science and Technology*, 27(3):181–191, 2015. 1.1, 1.1, 1.3

[35] Brandon P. Smith, Christopher L. Tanner, Milad Mahzari, Ian G. Clark, Robert D. Braun, and F. Mc Neil Cheatwood. A historical review of inflatable aerodynamic decelerator technology development. *IEEE Aerospace Conference Proceedings*, 2010. (document), 1.1, 1.4

[36] Juan Cruz and J. Lingard. Aerodynamic Decelerators for Planetary Exploration: Past, Present, and Future. In *AIAA Guidance, Navigation, and Control Conference and Exhibit*, 8, pages 5342–5361, Reston, Virigina, August 2006. American Institute of Aeronautics and Astronautics. 1.1

[37] David Akin. The ParaShield Entry Vehicle Concept: Basic Theory and Flight Test Development. *Small Satellite Conference*, 1990. 1.1

[38] David Akin. Applications of Ultra-Low Ballistic Coefficient Entry Vehicles to Existing and Future Space Missions. In *SpaceOps 2010 Conference*, Reston, Virigina, April 2010. American Institute of Aeronautics and Astronautics. (document), 1.1, 1.5, 4.1

[39] Matthias Wiegand and Hans J Königsmann. A Small Re-entry Capsule - BREM-SAT 2. *AIAA/USU Small Satellite Conference*, 1996. (document), 1.1, 1.6

[40] Detlef Wilde, Stephan Walther, and Astrium Gmbh. Inflatable Reentry and Descent Technology (IRDT) – Further Developments. *International Symposium of Atmospheric Reentry Vehicles and Systems*, pages 26–29, March 2001. 1.1, 1.7a

[41] Detlef Wilde, Stephan Walther, Konstantin Pitchadze, and Sergej Alexsaschkin. Flight test and ISS application of the Inflatable Reentry and Descent Technology (IRDT). *Acta Astronautica*, 51(1-9):83–88, jul 2002. 1.1

[42] L. Marraffa, D. Boutamine, S. Langlois, C. Reimers, C. Feichtinger, Th Walloschek, P. Kyr, and S. Alexashkin. IRDT 2R mission, first results. *European Space Agency, (Special Publication) ESA SP*, 2006(631):17–19, 2006. 1.1, 1.7b

[43] L. Marraffa, D. Vennemann, U. Anschuetz, S. Walther, C. S. Stelter, K. M. Pitchkhadze, and V. S. Finchenko. IRDT - Inflatable Re-entry and Descent Technology. In *4th European Workshop*, 2003. 1.1

[44] Stephen J. Hughes, Robert A. Dillman, Brett R. Starr, Ryan A. Stephan, Michael C. Lindell, Charles J. Player, and F. Mc Neil Cheatwood. Inflatable Re-entry Vehicle Experiment (IRVE) design overview. *Collection of Technical Papers - 18th AIAA Aerodynamic Decelerator Systems Technology Conference and Seminar*, pages 381–394, 2005. (document), 1.1, 1.8a, 3.1.2, 3.3

[45] Michael C. Lindell, Stephen J. Hughes, Megan Dixon, and Cliff E. Willey. Structural analysis and testing of the Inflatable Re-entry Vehicle Experiment (IRVE). *Collection of Technical Papers - AIAA/ASME/ASCE/AHS/ASC Structures, Structural Dynamics and Materials Conference*, 2:1303–1321, 2006. 1.1

[46] Robert A Dillman, Stephen J Hughes, and Richard J Bodkin. Flight Performance of the Inflatable Reentry. *NASA Technical Report*, NASA Technical Report(1):3–7, 2009. 1.1

[47] Stephen J. Hughes, F. McNeil Cheatwood, Robert A. Dillman, Henry S. Wright, Joseph A. Del Corso, and Anthony M. Calomino. Hypersonic Inflatable Aerodynamic Decelerator (HIAD) technology development overview. *21st AIAA Aerodynamic Decelerator Systems Technology Conference and Seminar 2011*, May 2011. 1.1, 1.1

[48] Aaron D. Olds, Roger E. Beck, David M. Bose, Joseph P. White, Karl T. Edquist, Brian R. Hollis, Michael C. Lindell, F M. Cheatwood, Valerie T. Gsell, and Ernest L. Bowden. IRVE-3 post-flight reconstruction. In *AIAA Aerodynamic Decelerator Systems (ADS) Conference 2013*, pages 1–24, Reston, Virginia, mar 2013. American Institute of Aeronautics and Astronautics. 1.1

[49] Robert Dillman, John DiNonno, Richard Bodkin, Valerie Gsell, Nathanael Miller, Aaron Olds, and Walter Bruce. Flight Performance of the Inflatable Reentry Vehicle Experiment 3. *Ippw*, 13(NF1676L-16379):2–5, 2013. 1.1

[50] David Jurewicz, Glen Brown, Brian Gilles, Anthony Taylor, Robert Sinclair, Benjamin Tutt, David Lichodziejewski, Christopher Kelley, and Stephen Hughes. Design and Development of Inflatable Aeroshell Structure for IRVE-3. In *21st AIAA Aerodynamic Decelerator Systems Technology Conference and Seminar*, pages 1–10, Reston, Virigina, May 2011. American Institute of Aeronautics and Astronautics. 1.1

[51] David Lichodziejewski, Christopher Kelley, Benjamin Tutt, David Jurewicz, Glen Brown, Brian Gilles, Dennis Barber, Robert Dillman, and Charles Player. Design and Testing of the Inflatable Aeroshell for the IRVE-3 Flight Experiment. In *53rd AIAA/ASME/ASCE/AHS/ASC Structures, Structural Dynamics and Materials Conference
20th AIAA/ASME/AHS Adaptive Structures Conference
14th AIAA*, 53, pages 1–11, Reston, Virigina, April 2012. American Institute of Aeronautics and Astronautics. 1.1

[52] National Aeronautics and Space Administration. Irve-3 concepts. 1.8b

[53] Daniel K. Litton, David M. Bose, F. McNeil Cheatwood, Stephen Hughes, Henry S. Wright, Michael C. Lindell, Stephen D. Derry, and Aaron Olds. Inflatable Re-Entry Vehicle Experiment (IRVE) - 4 overview. In *21st AIAA Aerodynamic Decelerator Systems Technology Conference and Seminar 2011*, pages 1–14, Reston, Virigina, May 2011. American Institute of Aeronautics and Astronautics. 1.1

[54] Henry Wright, Amanda Cutright, James Corliss, Walter Bruce, Dominic Trombetta, Ali Reza Mazaheri, Michael Coleman, Aaron Olds, and Sean Hancock. HEART Flight Test Overview. *9th International Planetary Probe Workshop*, 9, June 2012. 1.1, 1.9a

[55] David M. Bose, Richard Winski, Jeremy Shidner, Carlie Zumwalt, Christopher O. Johnston, D. R. Komar, F. M. Cheatwood, and Stephen J. Hughes. The Hypersonic Inflatable Aerodynamic Decelerator (HIAD) mission applications study. *AIAA Aerodynamic Decelerator Systems (ADS) Conference 2013*, pages 1–18, March 2013. 1.1

[56] J. M. DiNonno, F. M. Cheatwood, S. J. Hughes, M. M. Ragab, R. A. Dillman, R. J. Bodkin, C. H. Zumwalt, and R. K. Johnson. HIAD on ULA (HULA) Orbital Reentry Flight Experiment Concept. *NASA Technical Reports Server*, pages 1–7, June 2016 2016. 1.1, 1.9b

[57] Greg Swanson. The HIAD Orbital Flight Demonstratoin Instrumentation Suite, 2019. (document), 1.1, 1.10

[58] National Aeronautics and Space Administration. Low-earth orbit flight test of an inflatable decelerator (loftid). 1.1

[59] E. Venkatapathy, P. Wercinski, and D. Prabhu. Mechanically-Deployed Hypersonic Decelerator and Conformal Ablator Technologies for Mars Missions. In *Concepts and Approaches for Mars Exploration*, number 1 in 2, pages 1–29, 2012. 1.1

[60] Brandon P. Smith, Bryan C. Yount, Ethiraj Venkatapathy, Eric C. Stern, Dinesh K. Prabhu, and Daniel K. Litton. Progress in payload separation risk mitigation for a deployable Venus heat shield. *AIAA Aerodynamic Decelerator Systems (ADS) Conference 2013*, pages 1–14, March 2013. 1.1

[61] Paul F Wercinski, Ethiraj Venkatapathy, Peter J Gage, Bryan C Yount, Dinesh K Prabhu, Brandon Smith, James O Arnold, Keith Hoppe Peterson, Ronald I Chinnapongse, et al. Enabling venus in-situ science-deployable entry system technology, adaptive deployable entry and placement technology (adept): a technology development project funded by game changing development program of the space technology program. In *10th Meeting of the Venus Exploration Analysis Group*, number ARC-E-DAA-TN6611 in 10, 2013. 1.1

[62] Paul Wercinski, Ethiraj Venkatapathy, Peter Gage, Dinesh Prabhu, Brandon P. Smith, Alan M Cassell, B Yount, and Gary Allen. Adaptable, Deployable Entry and Placement Technology (ADEPT) for Future Mars Missions. *International Planetary Probe Workshop*, 2013. 1.1, 1.11a

[63] Ethiraj Venkatapathy, James Arnold, Ian Fernandez, Kenneth R. Hamm, David Kinney, Bernard Laub, Alberto Makino, Mary Kathleen McGuire, Keith Peterson, Dinesh Prabhu, Daniel Empey, Ian Dupzyk, Loc Huynh, Prabhat Hajela, Peter Gage, Austin Howard, and Dana Andrews. Adaptive deployable entry and placement technology (ADEPT): A feasibility study for human missions to mars. *21st AIAA Aerodynamic Decelerator Systems Technology Conference and Seminar 2011*, pages 1–22, May 2011. 1.1, 1.11b

[64] Bryan Yount, James O. Arnold, Peter Gage, Jeffrey Mockelman, and Ethiraj Venkatapathy. Structures and Mechanisms Design Concepts for Adaptive Deployable Entry Placement Technology. In *AIAA Aerodynamic Decelerator Systems (ADS) Conference*, Reston, Virginia, March 2013. American Institute of Aeronautics and Astronautics. 1.1

[65] Alan M Cassell, Brandon P Smith, Paul F Wercinski, Shakib M Ghassemieh, nasagov E Kenneth Hibbard, Adam P Nelessen, and James A Cutts. ADEPT, A Mechanically Deployable Re-Entry Vehicle System, Enabling Interplanetary CubeSat and Small Satellite Missions. *Small Satellite Conference*, pages 1–9, August 2018. 1.1

[66] Brandon Smith, Ethiraj Venkatapathy, Paul Wercinski, Bryan Yount, Dinesh Prabhu, Peter Gage, Lori Glaze, and Charles Baker. Venus in Situ Explorer Mission design using a mechanically deployed aerodynamic decelerator, 2013. 1.1

[67] James O. Arnold, Bernard Laub, Yih-Kang Chen, Dinesh K. Prabhu, M. E. Bittner, and Ethiraj Venkatapathy. Arcjet Testing of Woven Carbon Cloth for Use on Adaptive Deployable Entry Placement Technology. *IEEE Aerospace Conference*, pages 1–9, 2013. 1.1

[68] James O. Arnold, Keith H. Peterson, Bryan C. Yount, Nigel Schneider, and Jose Chavez-Garcia. Thermal and structural performance of woven carbon cloth for adaptive deployable entry and placement technology. In *AIAA Aerodynamic Decelerator Systems (ADS) Conference 2013*, pages 1–12, Reston, Virginia, March 2013. American Institute of Aeronautics and Astronautics. 1.1

[69] Yasunori Nagata, Kazuhiko Yamada, Takashi Abe, and Kojiro Suzuki. Attitude dynamics for flare-type membrane aeroshell capsule in reentry flight experiment. *AIAA Aerodynamic Decelerator Systems (ADS) Conference 2013*, pages 1–13, March 2013. 1.1, 1.12a

[70] Kazuhiko Yamada, Yasunori Nagata, Takashi Abe, Kojiro Suzuki, Osamu Imamura, and Daisuke Akita. Suborbital reentry demonstration of inflatable flare-type thin-membrane aeroshell using a sounding rocket. *Journal of Spacecraft and Rockets*, 52(1):275–284, 2015. 1.1

[71] Yusuke Takahashi, Kazuhiko Yamada, Takashi Abe, and Kojiro Suzuki. Aerodynamic Heating Around Flare-Type Membrane Inflatable Vehicle in Suborbital Reentry Demonstration Flight. *Journal of Spacecraft and Rockets*, 52(6):1530–1541, nov 2015. 1.1, 1.12b

[72] Taiki Koike, Yusuke Takahashi, Nobuyuki Oshima, and Kazuhiko Yamada. Aerodynamic heating prediction of flare-type membrane inflatable reentry vehicle from low earth orbit. *AIAA Atmospheric Flight Mechanics Conference, 2018*, 6(209999):1–21, 2018. 1.1

[73] Manabu Matsunaga, Yusuke Takahashi, Nobuyuki Oshima, and Kazuhiko Yamada. Aerodynamic Heating Prediction of an Inflatable Reentry Vehicle in a Hypersonic Wind Tunnel. In *55th AIAA*

Aerospace Sciences Meeting, pages 1–15, Reston, Virginia, January 2017. American Institute of Aeronautics and Astronautics. 1.1

[74] Yusuke Takahashi and Kazuhiko Yamada. Aerodynamic heating of inflatable aeroshell in orbital reentry. *Acta Astronautica*, pages 437–448, April 2018. 1.1

[75] E. Bassano, R. Savino, R. Lo Forti, A. Ferrarotti, C. Richiello, G. Russo, R. Aurigemma, F. Punzo, and P. Dell'Aversana. IRENE - Italian re-entry Nacelle for microgravity experiments. In *62nd International Astronautical Congress 2011, IAC 2011*, volume 1, pages 858–866, 2011. (document), 1.1, 1.13

[76] R. Savino, R. Aurigemma, Dr. Pasquale Dell'Aversana, L. Gramiccia, F. Punzo, J. Longo, L. Scolamiero, and L. Marraffa. European Sounding Rocket Experiment on Hypersonic Deployable Re-entry Demonstrator. *8th European Symposium on Aerothermodynamics for Space Vehicles*, March 2015. 1.1, 1.3

[77] Alberto Fedele and Stefano Mungiguerra. Aerodynamics and flight mechanics activities for a suborbital flight test of a deployable heat shield capsule. *Acta Astronautica*, 151:324–333, May 2018. 1.1

[78] P Vernillo, A Fedele, R Gardi, R Savino, F Punzo, F Gunnar, and R Molina. Mini-irene: The first european flight experiment of a deployable heat shield. In *23rd ESA Symposium on European Rocket and Balloon Programmes and Related Research*, 2017. 1.1

[79] R Gardi, P Vernillo, A Fedele, G Pezzella, R Savino, P Dell'Aversana, L Gramiccia, G D'aniello, R Aurigemma, N Cimminiello, et al. Mini irene-deployable heat shield for suborbital flight test. In *Proceedings of the 24th AIDAA International Conference. Palermo-Enna, Italy*, 2017. 1.1

[80] Alberto Fedele, Roberto Gardi, and Giuseppe Pezzella. Aerothermodynamics and thermal design for on-ground and in-flight testing of a deployable heat shield capsule. *CEAS Space Journal*, 12(3):411–428, 2020. 1.1

[81] R. Savino and V. Carandente. Aerothermodynamic and feasibility study of a deployable aerobraking re-entry capsule. *Fluid Dynamics and Materials Processing*, 8(4):453–476, 2012. 1.1

[82] A. Nocerino, I. Notaro, G. Morani, M. Poderico, E. D'Amato, L. Blasi, A. Fedele, R. Fortezza, M. Grassi, and M. Mattei. Trajectory control algorithms for the de-orbiting and Re-entry of the MISTRAL satellite. *Acta Astronautica*, pages 392–406, July 2023. 1.1, 1.3

[83] Raimondo Fortezza, Raffaele Savino, and Gennaro Russo. Mistral (air-launcheable micro-satellite with reentry capability) a small spacecraft to carry out several missions in LEO. *Proceedings of the International Astronautical Congress, IAC*, pages 524–534, January 2013. (document), 1.1, 1.14

[84] Alberto Fedele, Sanny Omar, Stefania Cantoni, Raffaele Savino, and Riccardo Bevilacqua. Precise re-entry and landing of propellantless spacecraft. *Advances in Space Research*, 68(11):4336–4358, 2021. 1.1

[85] Alberto Fedele, Salvatore Carannante, Michele Grassi, and Raffaele Savino. Aerodynamic Control System for a Deployable Re-entry Capsule. *Acta Astronautica*, 181:707–716, June 2020 2021. 1.1

[86] Alice Brunello, Andrea Valmorbida, Enrico C. Lorenzini, Stefania Cantoni, Mario De Stefano Fumo, Alberto Fedele, Roberto Gardi, and Raffaele Votta. Deorbiting small satellites from the ISS using a tether system. *CEAS Space Journal*, 13(2):217–230, 2021. 1.1, 1.3

[87] S Ianelli, M Albano, M Di Clemente, A Gabrielli, S Cantoni, M De Stefano Fumo, R Votta, A Fedele, R Gardi, M Cardi, et al. Iperdrone roadmap for new on orbit services performed by space drones. In *Proceedings of the 70th International Astronautical Congress, Washington DC (United States)*, pages 21–25, 2019. 1.1, 1.3

[88] Giuseppe Guidotti, Irene Pontijas Fuentes, Federico Trovarelli, Ingrid Dietlein, Roberto Gardi, Ysolde Prevereaud, Yann Dauvois, and Giuseppe Governale. EFESTO - advancing European hypersonic inflatable heatshield technology for Earth recovery and Mars high-mass delivery missions. *Aeronautics and Aerospace Open Access Journal*, 6(2):59–73, 2022. 1.1

[89] Davide Bonetti, Gabriele De Zaiacomo, Ingrid Dietlein, Burkard Esser, Giuseppe Guidotti, Alberto Fedele, Jean-luc Verant, Ysolde Prevereaud, Giovanni Gambacciani, Giulia Bimbi, Davide Bonetti, Gabriele De Zaiacomo, Ingrid Dietlein, Burkard Esser, Giuseppe Guidotti, Davide Bonetti, Gabriele De Zaiacomo, Ingrid Dietlein, Burkard Esser, Giuseppe Guidotti, Jean-luc Verant, Ysolde Prevereaud, Giovanni Gambacciani, Giulia Bimbi, Nicole Viola, Deimos Space S L U, and Tres Cantos. European Flexible Heat Shields : Advanced TPS Design and Tests for Future In-Orbit Demonstration. *The International Conference on Flight vehicles, Aerothermodynamics and Re-entry Missions and Engineering*, 2021. 1.1

[90] F. Trovarelli, G. Guidotti, G. Medici, B. Esser, T. Schleutker, I. Dietlein, G. Gambacciani, G. Governale, J. L. Verant, Y. Dauvois, and Y. Prevereaud. Advanced European Re-Entry System Based on Inflatable Heat Shields EFESTO project overview: System and mission design and technology roadmap. *Proceedings of the International Astronautical Congress, IAC*, D2:25–29, October 2021. (document), 1.1, 1.15

[91] G. A. Bird. *Molecular gas dynamics and the direct simulation of gas flows*. Oxford Science Publications, first edition, 1994. (document), 1.2, 1.16, 1.2, 2.3, 2.4, 2.5, 2.6, 2.7, 2.1.7, 2.2.3, 2.2.4, 3, 3.1.1, 3.1.1, 3.2.1, 4.1

[92] Jonathan Josyula, Eswar and Burt. Review of Rarefied Gas Effects in Hypersonic Applications. *Rto-En-Avt-194*, 2011. 1.2

[93] Alejandro L. Garcia. Direct Simulation Monte Carlo: Theory, Methods, and Open Challenges. *Rto-En-Avt-194*, pages 1–12, 2011. 1.2

[94] Francis J Alexander and Alejandro L Garcia. The Direct Simulation Monte Carlo Method. *Computers in Physics*, 11(6):588, 1997. 1.2

[95] C. White, M.K. Borg, T.J. Scanlon, S.M. Longshaw, B. John, D.R. Emerson, and J.M. Reese. dsmcFoam+: An OpenFOAM based direct simulation Monte Carlo solver. *Computer Physics Communications*, 224:22–43, mar 2018. (document), 1.2, 1.2, 2.9, 3

[96] Thomas E. Schwartzentruber, Maninder S. Grover, and Paolo Valentini. Direct Molecular Simulation of Nonequilibrium Dilute Gases. *Journal of Thermophysics and Heat Transfer*, 32(4):892–903, oct 2018. 1.2

[97] Thomas E. Schwartzentruber and Iain D. Boyd. Progress and future prospects for particle-based simulation of hypersonic flow. *43rd Fluid Dynamics Conference*, pages 1–19, 2013. 1.2

[98] John David Anderson. *Hypersonic and High Temperature Gas Dynamics (AIAA Education)*. American Institute of Aeronautics and Astronautics, 2006. (document), 1.18, 2.1, 3.1.1, 3.2.1

[99] Ernst Heinrich Hirschel. *Basics of Aerothermodynamics*. Springer International Publishing, Cham, 2nd edition, 2015. 1.2

[100] Iain D. Boyd and Thomas E. Schwartzentruber. *Nonequilibrium Gas Dynamics and Molecular Simulation*. Cambridge University Press, Cambridge, 2017. (document), 1.2, 2.2, 2.1.7, 2.8, 2.2.3, 2.2.4

[101] G. A. Bird. Forty years of DSMC, and now? In *AIP Conference Proceedings*, volume 585, pages 372–380. AIP, 2001. 1.2, 2.2.4

[102] G. A. Bird. Recent advances and current challenges for DSMC. *Computers and Mathematics with Applications*, 35(1-2):1–14, 1998. 1.2

[103] Jason Andrews, Krissa Watry, and Kevin Brown. Nanosat Deorbit and Recovery System to Enable New Missions, 2011. (document), 1.3, 1.19

[104] Dana G. Andrews, Michael Beerman, Kevin A Brown, Jeffrey H Cannon, Krissa E. Watry, and Jason Andrews. DEPLOYABLE DECELERATOR BASED MCROSATELLITE RECOVERY, 2012. 1.3

[105] Valerio Carandente, Gennaro Zuppardi, and Raffaele Savino. Aerothermodynamic and stability analyses of a deployable re-entry capsule. *Acta Astronautica*, 93:291–303, 2014. (document), 1.3, 1.21, 4.1

[106] Michele Iacovazzo, Valerio Carandente, Raffaele Savino, and Gennaro Zuppardi. Longitudinal stability analysis of a suborbital re-entry demonstrator for a deployable capsule. *Acta Astronautica*, 106:101–110, 2015. 1.3

[107] G. Zuppardi, R. Savino, and G. Mongelluzzo. Aero-thermo-dynamic analysis of a low ballistic coefficient deployable capsule in Earth re-entry. *Acta Astronautica*, 127:593–602, 2016. 1.3

[108] P. Pasolini, R. Savino, F. Franco, and S. De Rosa. Preliminary validation of fluid-structure interaction modeling for hypersonic deployable re-entry systems. *Fluid Dynamics and Materials Processing*, 11(3):301–324, 2015. 1.3

[109] Stefano Mungiguerra, Gennaro Zuppardi, and Raffaele Savino. Rarefied aerodynamics of a deployable re-entry capsule. *Aerospace Science and Technology*, 69:395–403, 2017. 1.3

[110] Kazuhiko Yamada, Takashi Abe, Kojiro Suzuki, Osamu Imamura, Daisuke Akita, Yasunori Nagata, and Yusuke Takahashi. Development of flare-type inflatable membrane aeroshell for reentry demonstration from LEO. In *Aerodynamic Decelerator Systems Technology Conferences*, Reston, Virginia, apr 2015. American Institute of Aeronautics and Astronautics. 1.3

[111] Maximilien Berthet, Kazuhiko Yamada, Yasunori Nagata, and Kojiro Suzuki. Feasibility assessment of passive stabilisation for a nanosatellite with aeroshell deployed by orbit-attitude-aerodynamics simulation platform. *Acta Astronautica*, 173(November 2019):266–278, 2020. (document), 1.3, 1.22

[112] Naoya Enoki, Yusuke Takahashi, Nobuyuki Oshima, Kazuhiko Yamada, and Kojiro Suzuki. Aerodynamics of inflatable nano-satellite "eGG" in low earth orbit and reentry duration. *AIP Conference Proceedings*, 2132(August), 2019. 1.3

[113] Yusuke Takahashi, Masahiro Saito, Nobuyuki Oshima, and Kazuhiko Yamada. Trajectory reconstruction for nanosatellite in very low Earth orbit using machine learning. *Acta Astronautica*, 194(January):301–308, 2022. 1.3

[114] Yusuke Takahashi. Propagation Path of Radio Waves in Nonequilibrium Reentry Plasma Around a Nanosatellite with an Inflatable Aeroshell. *IEEE Transactions on Aerospace and Electronic Systems*, 58(5):4070–4082, 2022. 1.3

[115] Paul Wercinski, Brandon Smith, Bryan Yount, Carl Kruger, Chad Brivkalns, Alberto Makino, Alan Cassell, Soumyo Dutta, Shakib Ghassemieh, Shang Wu, Stephen Battazzo, Owen Nishioka, Ethiraj Venkatapathy, and Gregory Swanson. ADEPT sounding rocket one (SR-1) flight experiment overview. *IEEE Aerospace Conference Proceedings*, 2017. 1.3, 1.23a

[116] Soumyo Dutta and Justin S. Green. Flight mechanics modeling and post-flight analysis of adept sr-1. *AIAA Aviation 2019 Forum*, pages 1–16, 2019. 1.3

[117] Ashley M. Korzun, Soumyo Dutta, Ryan D. McDaniel, Christopher D. Karlgaard, and Jake A. Tynis. Aerodynamics for the adept sr-1 flight experiment. *AIAA Aviation 2019 Forum*, pages 1–15, 2019. 1.3

[118] Brandon J. Reddish, Ben E. Nikaido, Sarah N. D'souza, Veronica M. Hawke, Zane B. Hays, and Hyung Suk Kang. Pterodactyl: Aerodynamic and aerothermal modeling for a symmetric deployable earth entry vehicle with flaps. *AIAA Scitech 2021 Forum*, pages 1–23, 2021. 1.3

[119] Wendy A. Okolo, Benjamin W. Margolis, Sarah N. D'souza, and Jeffrey D. Barton. Pterodactyl: Development and comparison of control architectures for a mechanically deployed entry vehicle. *AIAA Scitech 2020 Forum*, pages 1–14, 2020. 1.3

[120] Rui Wu, Peter C.E. Roberts, Constantinos Soutis, and Carl Diver. Downrange manoeuvre and oscillation suppression of a self-regulating centrifugally deployed flexible heat shield using a controlled reaction wheel. *Acta Astronautica*, 161(December 2018):415–424, 2019. 1.3

[121] Rui Wu, Peter C.E. Roberts, Lulu Xu, Constantinos Soutis, and Carl Diver. Deployable self-regulating centrifugally-stiffened decelerator (DESCENT): Design scalability and low altitude drop test. *Aerospace Science and Technology*, 114:106710, 2021. (document), 1.3, 1.24

[122] Ignazio Dimino, Cristian Vendittozzi, William Reis Silva, Salvatore Ameduri, and Antonio Concilio. A Morphing Deployable Mechanism for Re-Entry Capsule Aeroshell. *Applied Sciences (Switzerland)*, 13(5), 2023. 1.3

[123] Carlo Cercignani. *Rarefied Gas Dynamics - From Basic Concepts To Actual Calculations*. Cambridge University Press, 1st edition, 2000. 2.1.7, 2.2

[124] Walter G Vincenti, Charles H Kruger Jr, and T Teichmann. Introduction to physical gas dynamics, 1966. 2.1.7

[125] N. Hadjiconstantinou. Analysis of discretization in the direct simulation Monte Carlo. *Physics of Fluids*, 12(10):2634–2638, 2000. 2.2

[126] Zhi Xin Sun, Zhen Tang, Ya Ling He, and Wen Quan Tao. Proper cell dimension and number of particles per cell for DSMC. *Computers and Fluids*, 50(1):1–9, 2011. 2.2

[127] Alejandro L. Garcia and Wolfgang Wagner. Time step truncation error in direct simulation Monte Carlo. *Physics of Fluids*, 12(10):2621, 2000. 2.2

[128] Wolfgang Wagner. A convergence proof for Bird's direct simulation Monte Carlo method for the Boltzmann equation. *Journal of Statistical Physics*, 66(3-4):1011–1044, feb 1992. 2.2

[129] G.A. Bird. Perception of numerical methods in rarefied gas dynamics. *Progr. Astronaut. Aeronaut.*, 118:211 – 226, 1989. Cited by: 28. 2.2.2

[130] GA Bird. Shock-wave structure in a rigid sphere gas. In *Proceedings of the 4th International Symposium on Rarefied Gas Dynamics, New York, 1965*, volume 2, pages 216–222. Academic Press, 1965. 2.2.2

[131] Katsuhisa Koura. Null-collision technique in the direct-simulation monte carlo method. *The Physics of fluids*, 29(11):3509–3511, 1986. 2.2.2

[132] Kenichi Nanbu. Direct simulation scheme derived from the boltzmann equation. i. monocomponent gases. *Journal of the Physical Society of Japan*, 49(5):2042 – 2049, 1980. Cited by: 334. 2.2.2

[133] MS Ivanov and SV Rogasinskii. Theoretical analysis of traditional and modern schemes of the dsmc method. *Rarefied gas dynamics*, pages 629–642, 1991. 2.2.2

[134] Ehsan Roohi and Stefan Stefanov. Collision partner selection schemes in dsmc: From micro/nano flows to hypersonic flows. *Physics Reports*, 656:1–38, 2016. 2.2.2

[135] Aaron Pikus, Israel B. Sebastião, Shashank Jaiswal, Michael Gallis, and Alina A. Alexeenko. DSMC-SPARTA implementation of majorant collision frequency scheme. *AIP Conference Proceedings*, 2132(1):070026, 08 2019. 2.2.2

[136] N V Shugalevskaia, A A Shevyrin, and Ye A Bondar. Comparison of modern implementations of the direct simulation monte carlo method. *Journal of Physics: Conference Series*, 1404(1):012123, nov 2019. 2.2.2

[137] A Venkattraman, Alina A Alexeenko, MA Gallis, and MS Ivanov. A comparative study of no-time-counter and majorant collision frequency numerical schemes in dsmc. In *AIP Conference Proceedings*, volume 1501, pages 489–495. American Institute of Physics, 2012. 2.2.2

[138] Stefan K. Stefanov. Particle monte carlo algorithms with small number of particles in grid cells. In Ivan Dimov, Stefka Dimova, and Natalia Kolkovska, editors, *Numerical Methods and Applications*, pages 110–117, Berlin, Heidelberg, 2011. Springer Berlin Heidelberg. 2.2.2

[139] Stefan K. Stefanov. On dsmc calculations of rarefied gas flows with small number of particles in cells. *SIAM Journal on Scientific Computing*, 33(2):677–702, 2011. 2.2.2

[140] G A Bird. Monte-Carlo Simulation in an Engineering Context. In *Rarefied Gas Dynamics, Parts I and II*, pages 239–255. American Institute of Aeronautics and Astronautics, New York, jan 1981. 2.2.3

[141] G. A. Bird. Definition of mean free path for real gases. *Physics of Fluids*, 26(11):3222, 1983. 2.2.3

[142] Claus Borgnakke and Poul S. Larsen. Statistical collision model for Monte Carlo simulation of polyatomic gas mixture. *Journal of Computational Physics*, 18(4):405–420, aug 1975. 2.2.4

[143] G. A. Bird and Takashi Abe. A Comparison of Collision Energy-based and Temperature-based Procedures in DSMC. In *AIP Conference Proceedings*, pages 245–250. AIP, 2009. 2.2.4

[144] H. Alsmeyer. Density profiles in argon and nitrogen shock waves measured by the absorption of an electron beam. *Journal of Fluid Mechanics*, 74(3):497–513, 1976. 2.2.4

[145] G A Bird. Monte carlo simulation of gas flows. *Annual Review of Fluid Mechanics*, 10(1):11–31, 1978. 2.2.4

[146] G.A. Bird. Direct molecular simulation of a dissociating diatomic gas. *Journal of Computational Physics*, 25(4):353–365, 1977. 2.2.4

[147] G. A. Bird. Chemical Reactions in DSMC. *AIP Conference Proceedings*, 1333(1):1195–1202, 05 2011. 2.2.4

[148] Israel Borges Sebastião and Alina Alexeenko. Consistent post-reaction vibrational energy redistribution in DSMC simulations using TCE model. *Physics of Fluids*, 28(10):107103, 10 2016. 2.2.4

[149] Andrew Walker, Piyush Mehta, and Josef Koller. Different implementations of diffuse reflection with incomplete accommodation for drag coefficient modeling. *Journal of Spacecraft and Rockets*, 51(5):1522–1532, 2014. (document), 2.10

[150] American Institute of Aeronautics and Astronautics. *Guide for the Verification and Validation of Computational Fluid Dynamics Simulations (AIAA G-077-1998(2002))*. American Institute of Aeronautics and Astronautics, Inc., Washington, DC, 1998. 3

[151] James N. Moss, Katie A. Beyles, and Francis A. Greene. Orion aerodynamics for hypersonic free molecular to continuum conditions. *A Collection of Technical Papers - 14th AIAA/AHI International Space Planes and Hypersonic Systems and Technologies Conference*, 3:1749–1772, November 2006. (document), 3, 3.1.1, 3.1, 3.1.1, 3.1, 3.2, 3.2.1, 3.2.1, 3.6, 3.6

[152] James N. Moss, Christopher E. Glass, Brian R. Hollis, and John W. Van Norman. Low-density aerodynamics for the inflatable reentry vehicle experiment. *Journal of Spacecraft and Rockets*, 43(6):1191–1201, 2006. (document), 3, 3.1.2, 3.3, 3.1.2, 3.3, 3.4, 3.1.2, 3.2.2, 3.7, 3.2.2, 3.9, 3.2.2, 3.7, 3.8

[153] R. G. Wilmoth, D. B. VanGilder, and J. L. Papp. DSMC simulation of entry vehicle flowfields using a collision-based chemical kinetics approach. *AIP Conference Proceedings*, 1333(PART 1):1269–1274, 2011. 3.2.1

[154] Kyle B Thompson, Christopher O Johnston, Brian R Hollis, and Victor Lessard. Recent improvements to the laura and hara codes. In *AIAA AVIATION 2020 FORUM*, page 3030, 2020. 3.2.2

[155] National Oceanic And Atmospheric Administration; National Aeronautics And Space Administration; United States Air Force. *U.S. Standard Atmosphere 1976*. U.S. Government Publishing Office, 1976. (document), 4.1, 4.2

[156] Wilson F. N. Santos. Physical and computational aspects of shock waves over power-law leading edges. *Physics of Fluids*, 20(1), 01 2008. 016101. 4.2.2